April 2019

Water and Salt at the Lipid-Solvent Interface

James M. Kruczek
University of South Florida, james.kruczek@gmail.com

Water and Salt at the Lipid-Solvent Interface

by

James M. Kruczek

A dissertation submitted in partial fulfillment
of the requirements for the degree of
Doctor of Philosophy in Applied Physics
Department of Physics
College of Arts and Sciences
University of South Florida

Major Professor: Sagar A. Pandit, Ph.D.
Ullah, Ghanim, Ph.D.
Robert S. Hoy, Ph.D.
Jianjun Pan, Ph.D.
Yicheng Tu, Ph.D.

Date of Approval:
March 26, 2019

Keywords: Lipid Bilayer, Ionic Solvents, Ether Lipids, Molecular Simulations

Dedication

To my wife Nicole, without whom none of this would be possible.

To my father Michael, who labored for his family till his last days.

To my family, for all of their support.

Acknowledgments

The work presented in this document would not be possible without the assistance of many academic professionals. In particular, I would like to acknowledge my major advisor Dr. Sagar Pandit. Dr. Pandit, always knew when to push me to be better and when to show me how good I had become. He worked with me to improve not just my scientific skills, but professional and personal skills as well. When personal issues arose, he understood the gravity of them and help me work around them, never letting me give up.

This work would also not be possible without those who contributed to the manuscripts which we published. Thanks to Dr. Eric Jakobsson, for your vast knowledge of biological systems and in particular the role lithium plays in those systems. Thanks to Dr. See-Wing Chiu, for your experience and guidance with force fields. Thanks to Dr. Sameer Varma for your advice in ion behavior. Thanks to Dr. Yicheng Tu, for your help with optimizing computation and process. Thanks to Dr. David Rabson, for his challenging questions around modeling collagen. Thanks to Dr. Garrett Matthews for your insight into how collagen fibrils behave. Thanks to Brad Bennett, for the work you did on the collagen fibrils simulations. Thanks to Matthew Saunders and Meghna Khosla for your hard work collecting and analyzing data.

Thanks to Dr. Joseph Fogarty who preceded me in the Computational Soft Matter lab and left a great deal of automation to leverage, as well as an excellent reputation to live up to.

I would also like to thank my graduate committee for their patience, understanding, and their contributions to the work presented within.

Finally, I would like to give an additional thank you to Dr. David Rabson and Dr. Sagar Pandit for the financial help while I was a struggling undergraduate at the University of South Florida. The computational science scholarship, headed by Dr. Rabson, was of great assistance in my academic and personal life and cannot be adequately described. Dr. Pandit always seemed to find money for summer research, so I could continue working in the lab and remain focused on science.

Table of Contents

List of Tables

List of Figures

Abstract

Lipid bilayers are important biological structures. The changes in bilayer properties are induced by the composition of the bilayer as well as the solvent. In this work, we study the effects of different molecular makeups of lipids and ionic solvents with molecular dynamics simulations to determine their effect on the bilayer interface. In particular, we look at how different carbon chain bindings affect water viscosity at the interface and allow for a less permeable bilayer. Additionally, we examine the changes to the bilayer due to the presence of the most biologically relevant salt ions. Lastly, we show how the pharmacological ion lithium may replace magnesium due to overlapping solvation shells.

Chapter 1

Introduction

The cell is the fundamental building block, and the smallest unit of life, bound by a membrane. The membrane has two primary functions. First, to act as the boundary for the cell, providing individuality and integrity, while also creating a barrier to diffusion. Second, the membrane creates a structure for proteins and other signaling pathways to which to adhere to.

1.1 Lipid Membrane

Membranes are diverse in both composition and function, and therefore it is convenient to define a general model for cell membranes. The foremost model of the membrane is the fluid mosaic model [1]. In this model, the cell membrane is a two-dimensional, liquid bilayer of lipids in which globular protein molecules are suspended. The hydrophilic regions of the protein protrude from the membrane surface while hydrophobic regions are embedded in the membrane [1]. Proteins can even extend from one membrane surface to another. Another important aspect to the model is that since the membrane is a liquid, proteins can diffuse across the surface of the bilayer.

The composition of cell membranes varies significantly with the type or function of the cell, but the supporting structural matrix is almost always a lipid bilayer. Lipid bilayers are composed of amphiphilic lipids, meaning they have both water-soluble hydrophilic and water-insoluble hydrophobic regions. By hydrophilic regions, we mean regions with thermodynamic properties which cause free energy to decrease as polar solvents, such as water, surround the regions. Moreover, by hydrophobic, we mean regions with thermodynamic properties such that free energy increases as polar solvents neighbor them. In order to minimize the solvation free energy of the system, lipids self-organize in the presence of a polar solution [2].

In bulk, this self organization takes different forms. The actual form taken by the lipids depends considerably on the molecular geometry of bulk lipids [3]. This geometry is defined primarily by the areas of the hydrophobic and hydrophilic regions of the lipids. By area, we mean the

equilibrium distances between hydrated lipids. When lipids are conical in shape, that is to say, that the hydrophobic portion is smaller in area than the hydrophilic, they organize such that the hydrophobic portions, which can be packed closer, all face the center of a spherical blob. This lipid sphere is referred to as a micelle.

When lipids are cylindrical in shape, or even reverse conical, that is to say, the area of their hydrophobic section is the same size or larger than that of the hydrophilic section, the lipids will organize into a bilayer [3]. A bilayer is composed of two opposite facing planes, or leaflets, of lipids where the hydrophilic portions face outward, away from the center, while the hydrophobic portions face each other towards the center of the plane. A cross section of a portion of a lipid bilayer can be seen in figure 1.1.

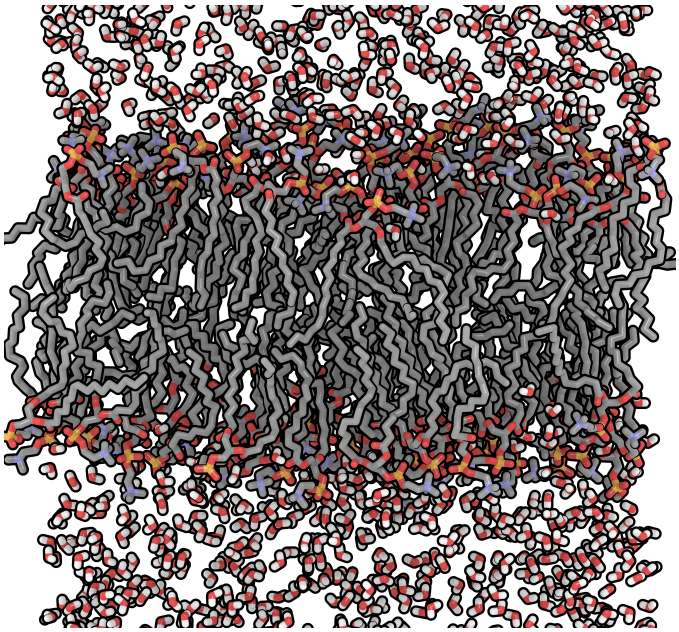

Figure 1.1: Rendering of a portion of a DPPC lipid bilayer simulation using Qutemol software package. In this figure, oxygen atoms are colored red, nitrogen blue, phosphate yellow, hydrogen white, and carbon as gray. Note that the hydrophobic carbon chains are all organized towards the center of the bilayer.

A significant amount of the remaining energy of a bilayer sheet are the hydrophobic edges exposed to the polar solvent. In order to reduce its energy further, a bilayer will spontaneously curve until it is spherical in shape, this is called a liposome. This sphere is not a micelle, but rather a vesicle where the two leaflets have together created a sphere with a portion of the solvent on the inside and a (generally larger) portion of the solvent on the outside. This reduction in the exposed

hydrophobic portions dramatically outweighs the energy cost of the curvature [2]. This energy cost can be reduced when the bilayer consists of molecules of two different lipids. When two different lipids are combined, the more conical shaped lipid will favor the outer leaf of the vesicle while less conical shaped lipid will prefer the interior. This organization is less entropically favorable but is also balanced with a favorable decrease in energy from more efficient packing [3].

1.1.1 Lipid Molecules

Lipid membranes are composed of many species of lipids. Though not all lipids are present in lipid bilayers, they are defined broadly as molecules which dissolve in organic solvents but are insoluble in water [4]. Lipids can be purely hydrophobic, *i.e.*, non-polar, or amphiphilic, having both a polar and non-polar region. Amphiphilic lipids are crucial in the formation of lipid bilayers.

The most simple form of lipids are fatty acids. Fatty acids are aliphatic chains attached to a carboxylic acid. Fatty acids can be categorized as saturated, meaning no carbon atoms in the chain are double bonded, or unsaturated, meaning at least one pair of carbon atoms are double bonded. Unsaturated fatty acids can be further categorized as mono-unsaturated, denoting that only one of the pairs of covalently bonded carbons in the chain are double bonded, or poly-unsaturated, denoting more than one double bond is located on the chain. Fatty acids can also be classified by length. Two prevalent fatty acids are palmitic acid (palm oil), a 16 carbon saturated fatty acid, and oleic acid (olive oil), an 18 carbon mono-unsaturated fatty acid.

In addition to being lipids themselves, fatty acids may bond to larger complexes to make up more complex lipids. The group which the fatty acids bind to is referred to as the backbone of the lipid. The most common backbones are glycerol and sphingoid. Lipids with a glycerol base are referred to as glycerolipids while lipids with sphingoid backbones are referred to as sphingolipids.

Glycerol has three available binding sites. Because of glycerol's chirality, these sites can be distinguished and are labeled as Sn1, Sn2, and Sn3. These sites can be occupied by an ester bonded fatty acids, an ether bonded carbon chains, or some form of hydrophilic group. When a hydrophilic group occupies a site, that group is typically referred to as the head group of the lipid. The most common example of a glycerolipid with a head group is a phospholipid. A phospholipid is a lipid with a head group whose base is a phosphate group, attached to the Sn3 position of the glycerol.

1.1.2 Glycerophospholipids Classification

A glycerolipid with a phosphate-based head group (phospholipid) is more specifically called a glycerophospholipid. Additional chemical groups, attached to the phosphate base of the head group, can be used to classify the glycerophospholipid further. The more common additions to the phosphate group are choline, inositol, ethanolamine, serine, glycerol, among others. When a single instance of the group is present, the lipid is referred to as phosphatidylcholine, phosphatidylinositol, phosphatidylethanolamine, phosphatidylserine, and phosphatidylglycerol respectively.

Since a phosphoglyceride has two carbon chains, often referred to as its tails, they can be further categorized by the type of chain and the method at which it is bounded to the lipid. For example, phosphatidylcholine with palmitic acid in the Sn1 position and oleic acid in the Sn2 position has the chemical name 1-palmitoyl-2-oleoyl-sn-glycero-3-phosphocholine and is commonly referred to as palmitoyloleoylphosphatidylcholine or POPC (see figure 1.2b), whereas the lipid in figure 1.2a with both the Sn1 and Sn2 sites occupied by a palmitic acid has the chemical name 1,2-dipalmitoyl-rac-glycero-3-phosphocholine, more commonly referred to as dipalmitoylphosphatidylcholine or DPPC.

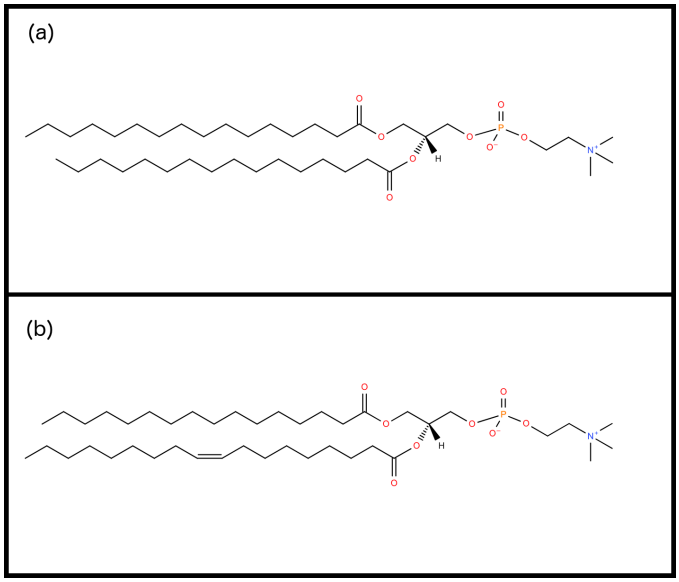

Figure 1.2: Line drawings of (a) a DPPC lipid and (b) a POPC lipid.

1.1.3 Ether Lipids

Another important class of phospholipids is ether lipids. These lipids replace at least one ester bound fatty acid with an ether bound alkyl or acetyl group. Much like fatty acids, alkyl and acetyl groups can be classified by their length, and whether they are saturated or unsaturated. However, unlike their ester bounded counterparts, ether bounded lipids lack the double bounded carbonyl. Examples of ether lipids in nature include plasmanyl- and plasmenyl-phospholipids, lipids with a single ether bond, appear in specialized animal tissue such as heart and brain [5]. Additionally, ether lipids are most common in archaea [6].

Archaea are a distinct domain of life from bacteria or eukaryota. A critical contrast between Archaea and other domains are the lipid composition of their bilayers [6]. While eukaryotic and bacteria bilayers are composed primarily of ester bonded fatty acids, archaea are composed of ether bonded isoprenoids. Additionally, ether bonded isoprenoids are attached to the Sn2 and Sn3 binding site of glycerol rather then the Sn1 and Sn2 to which ester bonded fatty acids are attached [7]. The distinction in the lipid makeup of the bilayers is interesting for two reasons. First, because the differences in bilayer makeup between archaea and bacteria may inform us what the membrane of the last universal common ancestor (LUCA) might look like and what caused the first split into the two now established domains [7]. Second, species of archaea are frequently found to survive and even thrive in extreme environments such as high salt concentration. These environments require specialization such as membranes that can withstand additional stress. In this work we will address ways ether lipids in archaeal bilayers could be an evolved mechanism to deal with these extreme environments.

1.1.4 Sterol Lipids

A class of lipids which are distinct from glycerophospholipids, sphingolipids, and other simple fatty acid chains are sterol lipids. The base of sterol lipids are a chain of four, nearly planar, carbon rings as can be seen in figure 1.3. Unlike many eukaryotic cells, prokaryotic membranes lack sterols. The primary sterol lipid found in animals is cholesterol. Cholesterol and other sterols adjust the dynamics [8] of lipid bilayers in order to keep portions of the membrane in a liquid-ordered state [9]. By liquid ordered, we mean a state where the lipids still diffuse and rotate in the bilayer similar to

a liquid, but are as highly ordered as they would be in low-temperature solid states.

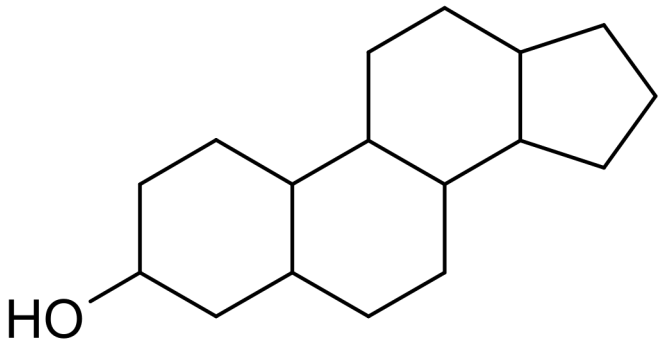

Figure 1.3: Line drawing of a sterol molecule.

1.1.5 Physiological Solvents

Most often in nature, lipids are suspended in water with many minerals, the most important of which are alkali metal salts. Ions, such as Na^+, K^+, Ca^{2+}, Mg^{2+}, and Cl^- play an essential role in cell functions. Many of these functions rely on the barrier formed by the lipid bilayer to regulate ion concentration.

In addition to acting as a barrier to ions, lipids can also act as a capacitor of sorts, storing concentrations of positive cations along their surface. Since cations can better bind to the negatively charged oxygen atoms along the hydrophilic region of the lipid, they will often take the place of polar molecules such as water. Depending on the concentration, these substitutions alter the physical properties of the bilayer. Bilayers may have evolved to be suited for particular solvent environments. Archaea, for example, are often classified as extremophiles, thriving in environments with high temperatures, high salt content, or high methane concentration. Since archaea evolved in these environments, it is theorized their ether-based lipid composition provided advantages in these chronic energy stress environments [10].

1.1.6 Lipid-Solvent Interface

Lipid bilayers define a barrier, and therefore, a surface with solvent surrounding it. The chemical composition of the lipids which make up the bilayer and the particles that make up the solvent both affect the behavior and stability of the interface.

1.2 Structure and Characterization of Lipid Bilayers

1.2.1 Differential Scanning Calorimetry

The phases and phase transitions of the lipid membrane are a significant aspect of their function. Phases of the membrane have different stability, permeability, and compressibility among other structural properties. A Differential Scanning Calorimeter (DSC) is used to determine phase transition temperatures and enthalpies. Both transition temperature and transition enthalpy can be derived from measurements as well as the change in the heat capacity along the transition [11]. DSCs achieve this by measuring the temperature difference between the two vessels. The first vessel contains the lipid of interest while the second is a reference solution. The temperature difference is measured between these vessels as a function of a set heating rate [12]. Phase transitions resulting from thermal energy will result in a temperature lag which is used to determine the thermodynamic properties of the transition [12].

1.2.2 Form Factors

The atomic structure of lipid membranes cannot be determined directly. Instead, experiments are done using small-angle scattering from sources such as X-ray (SAXS) or neutrons (SANS) to produce the reciprocal space representation known as form factors. The combination of these form factors is useful in more accurately describing the system since they scatter more effectively in different environments. SAXS, with its small wavelength, is most effective in electron-dense regions such as the phosphate groups while SANS is ideal in hydrogen deficient areas such as glycerol or carbonyl.

These form factors are not fully reversible due to the inherent disorder of liquid phase lipids [13] and the unavailability of the full spectrum of scattering [14]. To derive the physical structure of the lipid assembly from the measured form factors, a model must be imposed on the system. The scattering density profile (SDP) model uses volume probability distributions and their spatial conservation as restrictions to the inverse solution [13], while the atomically detailed model (ADP) optimizes a large number of atomistic parameters with restrictions and averages under-determined values using a weight factor.

The volume of the lipid molecule V_l is used to derive other structural properties such as area and thickness. These volumes are determined from techniques such as neutral flotation, where the density of water is changed by altering concentrations of H_2O and D_2O until the lipid neither floats nor sinks [15]. Volumes of the lipid chains (V_c) and head groups (V_{hg}) are both determined in the gel phase DPPC. It is assumed that V_{hg} does not change in the liquid phase since it is fully hydrated in both phases [15]. The scattering density profile determines the area per lipid (A) from the equation

$$AF(0) = 2(n_L \rho_W V_L), \tag{1.1}$$

where $F(0)$ is the zero-ith order form factor, ρ_W is the electron density of water, and n_L is the number of electrons per lipid [15]. With volume and area known, one can derive the thickness of the components from them. The thickness of the hydrocarbon chains ($2D_c$) is then $2D_c = V_c/A$, and the thickness of the entire bilayer ($2D_b$) is $2D_b = V_c/A$ [15].

1.2.3 Nuclear Magnetic Resonance Spectroscopy

Nuclear magnetic resonance (NMR) is a technique used to probe molecular positioning, molecular order, and molecular dynamics. Atomic nuclei have spin-1/2 or spin-1. When a magnetic field is applied to a spin 1/2 nucleus, the energy of the spin splits between a higher or lower state, depending on the direction of the spin. Atoms with a spin-1, have a quadrupole splitting of energies. The output of NMR experiments is resonance spectra whose peaks can be used to identify groups. H-nuclear magnetic resonance sometimes referred to as proton nuclear magnetic resonance since when H binds to other elements, it does not have sufficient electro-negativity to keep the electron and is therefore essentially a proton.

The resonance spectra from $^1H - NMR$ is a strong signal that can be easily matched to a chemical structure. Deuterium nuclear magnetic resonance ($^2H - NMR$) is similar to $^1H - NMR$ except the hydrogen being tested are deuterium, and therefore they have an extra neutron. This extra neutron gives the nucleus spin 1. Also, unlike $^1H - NMR$, deuterium hydrogen is seldom naturally present in lipids and can therefore be added for targeting purposes. Deuterium hydrogen NMR experiments can be used to determine the C-C bond order parameter. This order relates

to the alignment of the chains and is highest when they are straight. Therefore bilayer thickness can be estimated using the carbon order parameters. Phosphorus-31 nuclear magnetic resonance (P-NMR) works on the magnetic resonance spectra of phosphorus. These shifts from neighboring protons can be used to determine head group orientation. ^{13}C Carbon NMR with Magic-angle spinning (MAS) is used to determine the carbon ordering parameter [16], which is an essential measurement to understand when bilayers are approaching phase transitions. ^{2}H-NMR deuterium water allows experiments to record quadrupole splitting of the water oriented by the charges in the lipid head group.

1.2.4 Membrane Electrostatics and Electrophoretic Mobility

Dipole potential measurements are made by [17] step wise changes in applied voltage and their resultant step in current using the voltage-clamp technique. Neher and Sakmann developed the electrophysiological patch clamp technique. The current across the membrane associated with the opening and closing of individual ion channels in the cell membrane can be measured by applying a defined voltage across the membrane via electrodes in the solution phases on each side of the membrane. The effect of the change of dipole potential on the opening and closing rates of ion channels can be investigated in detail.

The vibrating plate method involves bringing a condenser electrode near the surface of the bilayer. The electrode position is then shifted. The other electrode is placed under the bilayer. The vibration of the plate results in a measurable capacity variance $C(t)$. The dipole potential is defined by the amount of voltage needed to counter the effect and minimize the signal [18].

When liposomes are exposed to an electric field (E), whether due to the charge of the lipid or charge of ions bound to its surface, they will move with some electrophoretic velocity (ν_{ep}) equal to

$$\nu_{ep} = \mu_{ep} E, \tag{1.2}$$

where μ_{ep} is the electrophoretic mobility of the liposome. For a liposome with a sufficient radius

compared to the Debye-Huckel parameters, the electrophoretic mobility is defined as

$$\nu_{ep} = \frac{\zeta \epsilon \epsilon_0}{\eta}, \tag{1.3}$$

where ϵ and ϵ_0 are the dielectric constant of the medium and permittivity of free space respectively, η is the dynamic viscosity of the medium, and ζ is the electrostatic potential at the surface of the liposome. The potential is of interest as it relates to the total charge inside the "slip surface," inside of which particles move with the liposome.

1.3 Simulations and Models of Lipid Bilayers

Although experiments give a substantial insights into the properties of bilayers, simulations of model solutions are ideal for understanding the microscopic models which are the underpinnings of the bulk properties of lipid membranes. Importantly, for microscopic measurements to be reliable explanations for macroscopic properties, the models must reproduce the macroscopic properties within an appropriate approximation.

The most accurate simulations are ab initio, quantum calculations in which electronic structure along with nuclear coordinates evolves in time. These simulations are the most exact, but this complexity restricts the size and time scales of the simulations. To simulate on length and time scales needed to measure bulk properties of a bilayer, classical approximations are needed.

To simulate on length and time scales needed for lipid bilayers, atomic simulations are used, where atoms are considered restricted to a point, and the complicated quantum interactions are simplified to a set of classical potentials. The potentials used to evolve the system are Lennard-Jones (6-12), electrostatic, and inter-molecular forces, which are approximated as simple springs, for 2 (bonded), 3 (angle), and 4 (dihedrals) body interactions. Additional approximations are made by removing hydrogen from the lipids which decreases the number of atoms needed to be updated. This has added benefit since hydrogen atoms have a much smaller mass and therefore can have much larger step sizes than other atoms. This model of simulation is referred to as United Atom (UA).

1.3.1 Molecular Dynamics Simulations

The most common form of simulation are Molecular Dynamics (MD) simulations, where given an initial set of positions for all atoms in the system, the system is evolved according to Newtons equations of motion using the potential functions described in the previous section. All atoms are treated as point particles for purposes of computing position or momentum [19]. Without additional restrictions, MD simulations give rise to NVE ensembles. That is to say, an ensemble of frames which will be constant with respect to the number of particles, the volume, and the total energy of the system. This is often not the most faithful to biological conditions, where energy flows freely between it and the environment and the system can grow as needed. A more appropriate ensemble for lipids is typically NPT. In this ensemble, the number of particles, pressure, and temperature are held constant.

Temperature, in the context of a molecular dynamics simulation, is calculated from the momentum of the particles in the simulation. Temperature coupling is the process of fixing the temperature of the simulation by controlling these momenta. There are many methods of temperature coupling, but the Nosé-Hoover coupling scheme [20] is the only one used throughout this paper. In this coupling scheme, a frictional parameter (ξ) is added with a reservoir. The force of friction added to the particle is proportional to ξ and the velocity of the particles. The frictional parameter itself has a momentum p_ξ whose derivative is equal to the difference between the current temperature and the desired temperature. The new equation of motion for particle i is now described by the equation

$$\frac{d^2\mathbf{r_i}}{dt^2} = \frac{\mathbf{F_i}}{m_i} - \frac{p_\xi}{Q}\frac{d\mathbf{r_i}}{dt}, \tag{1.4}$$

where F_i is the net force acting on the i–th particle, $\mathbf{r_i}$ is its position, and Q is the mass parameter of the reservoir.

Pressure must also be held constant as well to achieve an NPT ensemble. Pressure couples are used to keep the pressure constant. The most common, or at least the one used exclusively in this work, is the Parrinello-Rahman pressure coupling [21]. In this coupling, changes are made to the

box dimensions described by the matrix $\mathbf{b}$, according to the equations

$$\frac{d^2\mathbf{b}}{dt^2} = V\mathbf{W}^{-1}\mathbf{b}'^{-1}(\mathbf{P} - \mathbf{P_{ref}}), \tag{1.5}$$

where V is the volume of the box, $\mathbf{W}$ is the matrix which determines the strength, and P and P_{ref} are the current and target pressure matrix respectively. Similar to Nosé-Hoover modifications to coupling, Parrinello-Rahman makes the following changes to the equations of motion

$$\frac{d^2\mathbf{r_i}}{dt^2} = \frac{\mathbf{F_i}}{m_i} - \mathbf{b}^{-1}\left[\mathbf{b}\frac{d\mathbf{b}'}{dt} + \frac{d\mathbf{b}}{dt}\mathbf{b}'\right]\mathbf{b}'^{-1}\frac{d\mathbf{r_i}}{dt}. \tag{1.6}$$

The pressure coupling can also be either isotropic, where the three dimensions of the simulation remain equal, semi-isotropic, in which only two box dimensions have this restriction, and anisotropic where all three box dimensions are free to adjust independently to maintain the target pressure. For lipid bilayers, semi-isotropic, where the direction normal to the bilayer is independently held at constant pressure, is necessary since it allows the depth of the simulation to change in order to accommodate changes in area per lipid for the bilayer to reach an equilibrium.

Additional ensembles sometimes used to simulate bilayers are NVT or NAPT. NVT, in particular, semi-isotropic NVT, is often used to fix the area of the box as well as the depth in order to create a difference in pressure between the lateral box pressure and the normal pressure, perpendicular to the bilayer, to achieve an imposed surface tension. NAPT is also used to enforce a surface tension by fixing the area parallel to the bilayer and allowing the depth to adjust to obtain the set pressure.

1.3.2 Force Field Parameters

As stated in section 1.3, three sets of potentials are used to evolve the system. Each of these sets of potentials requires parameters specific to the atom and molecule. The collection of these parameters is often referred to as the force field as they define the forces between the atoms in the simulation. In some cases, these forces are approximated from the actual force in physics due to limitation discussed below.

Coulomb potentials are the most classic form of potentials used, and for all non-bonded pairs

of atoms, follow the equation

$$V_c(r_{ij}) = \frac{1}{4\pi\epsilon_0}\frac{q_i q_j}{\epsilon_r} \tag{1.7}$$

where the constant ϵ_0 is the permittivity of free space, ϵ_r is the dielectric constant of the medium, r_{ij} is the distance between the two particles i and j, and q_i and q_j are the charges of the i–th and j–th particles. Therefore, the parameters needed are the charges on the atoms, which as stated earlier are assumed to be fixed with time. The net charge on an atom is the result of the difference between the number of protons the atom has minus the net number of electrons. For atoms where this number is constant, such as ions, this charge is well known. For atoms which are part of a larger covalently bonded molecule, the number of electrons associated with that atom orbiting the atom needs to be determined through quantum calculations.

Coulomb potentials are also long-range potentials, requiring the resulting force between any two charged atoms in the simulated box be calculated, and in most simulations, periodic boundary conditions (PBC) are implored, assuming each simulated box in neighbored by an identical box on each side, thereby making the simulation infinite. These PBC with long-range coulomb potentials result in a significant number of interactions that required calculation. To reduce the time needed to compute this potential, the particle-mesh Ewald [22] method is used, whereby the total potential on a particle is split into a short-range summation, which converges quickly in real space, and a long-range summation, which converges quickly in reciprocal space. Additionally, by placing the long range charges on a lattice and using Fast Fourier Transform (FFT), we can reduce the time needed to compute the reciprocal potential [22].

Along with coulomb potentials, non-bonded atoms each have an additional short-range repulsive term, which is a result of Pauli repulsion, and an additional attractive dispersion term. These terms are combined to a single equation. Although an attractive portion is known to have a functional form $\propto r^{-6}$, the repulsive term is a quantum repulsion, and its functional form is not defined. Therefore it is often assumed to be an exponential, in which this combined function is referred to as the Buckingham potential, or, more commonly, of the form $\propto r^{-12}$, where the function is referred to as the Lennard-Jones potential. In the following work, we will limit ourselves the Lennard-Jones

function

$$V_{LJ}(r_{ij}) = \frac{C_{ij}^{(12)}}{r_{ij}^{12}} - \frac{C_{ij}^{(6)}}{r_{ij}^{6}} \tag{1.8}$$

Where $C_{ij}^{(12)}$ and $C_{ij}^{(6)}$ are adjustable parameters for atom types i and j. This function two additional forms to make interpretation more straight forward. These forms are

$$V_{LJ}(r_{ij}) = 4\epsilon_{ij}\left[\left(\frac{\sigma_{ij}}{r_{ij}}\right)^{12} - \left(\frac{\sigma_{ij}}{r_{ij}}\right)^{6}\right] \tag{1.9}$$

$$V_{LJ}(r_{ij}) = \epsilon_{ij}\left[\left(\frac{R_{ij}}{r_{ij}}\right)^{12} - 2\left(\frac{R_{ij}}{r_{ij}}\right)^{6}\right], \tag{1.10}$$

where ϵ_{ij}, σ_{ij}, and R_{ij} are also adjustable parameters related to $C_{ij}^{(12)}$ and $C_{ij}^{(6)}$ through the equations

$$R_{ij} = 2^{-1/6}\sigma_{ij} \tag{1.11}$$

$$C_{ij}^{(12)} = 4\epsilon_{ij}\sigma_{ij}^{12} \tag{1.12}$$

$$C_{ij}^{(6)} = 4\epsilon_{ij}\sigma_{ij}^{6}. \tag{1.13}$$

In these new functional forms, the parameters have units of distance, in the case of σ_{ij} and R_{ij}, and energy, in the case of ϵ_{ij}. These parameters can be located on a general plot of the potential seen in figure 1.4. We note in the figure, σ_{ij} is the distance where the Lennard-Jones potential is zero, R_{ij} is the location of the minimum energy of the potential, and therefore the relaxed distance between two particles, and ϵ_{ij} is the depth of the energy well, and therefore the energy required to separate atoms in the minimum energy.

These Lennard-Jones potentials are much shorter than coulomb potentials, going to zero as r^{-6} rather then r^{-2}. This shorter distance means that we can ignore interaction from atoms beyond a sufficient cutoff distance.

The last set of potentials which require a definition of parameters are bonded potential. These are potentials for neighboring atoms in a molecule. Although bonded interactions, in reality, are quite complicated quantum interactions, which could even break when given enough energy, we

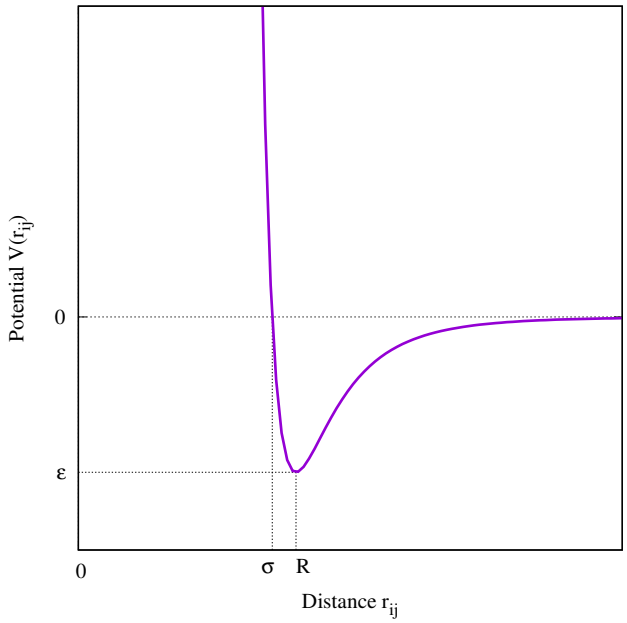

Figure 1.4: Lennard-Jones potential plot denoting location of parameters.

assume for molecular dynamic simulations that all bonds are permanent and can be modeled as simple harmonic potentials. These potentials require two parameters, a spatial parameter b and an energy parameter k. These potentials can be grouped into two-body (bond length), three-body (angle), and four-body (dihedrals) interactions. Examples of MD equations for two-body, three-body, and four-body bonded potentials respectively are

$$V_b(r_{ij}) = \frac{1}{2} k_{ij} \left(r_{ij} - b_{ij}\right)^2, \tag{1.14}$$

$$V_\theta(\theta_{ijk}) = \frac{1}{2} k^\theta_{ijk} \left(\theta_{ijk} - b^\theta_{ijk}\right)^2, \tag{1.15}$$

$$V_{i\ d}(\xi_{ijkl}) = \frac{1}{2} k^\xi_{ijkl} \left(\xi_{ijkl} - b^\xi_{ijkl}\right)^2, \tag{1.16}$$

where b_{ij}, b^θ_{ijk}, and b^ξ_{ijkl} are the spatial terms and k_{ij}, k^ξ_{ijkl}, and k^ξ_{ijkl} are the energy terms for atoms of type i, j, k, and l respectively. Other expressions of these interactions exist, and in some cases require additional terms, but in all cases, the correct parameters need to be chosen to achieve accurate simulations.

It is necessary, if not sufficient that the choice of force field parameters must adequately repro-

duce experimental values, in order for a simulation using those force fields to be considered accurate. Therefore the choice and improvement of force field parameters ultimately center around reproducing experiential data. This is not an easy task, as the parameters, depending on the simulation, can number in hundreds of, often interdependent, parameters. Although some systems of general optimizations techniques have been proposed and utilized [23], typically, the improvement to these parameters has centered around tuning sets of parameters while comparing simulated results with experimental values which are affected most by those parameters and by computing the parameters in ab initio, or quantum calculations. Lennard-Jones parameters are optimized until simulations match experimental densities and heats of vaporizations [24]. Additionally, these parameters can be computed for a target molecular group, such as n-alkane chains, and are sufficiently accurate for use in the carbons in the lipid chain. Parameters for dihedral torsion and partial charges on covalently bonded atoms are derived from quantum calculations [24].

1.4 Analysis of Molecular Dynamic Simulations

MD Simulations provide two primary types of analysis. First, macroscopic parameters, similar to those measured in experiments, can be deduced, assuming that the model tying the experiment to particle behavior is correct. This analysis is essential to validate the simulation, and all related parameters such as force fields, are a correct model of the real system. The second type of analysis is one that does not compare a simulated result to an experiment but instead measures a microscopic parameter to determine the mechanisms which are the drivers of experimental behavior. This analysis allows scientists to explain the cause of the phenomenon and predict yet unobserved behaviors. This is the basis for theoretical work which leads to drug discovery or other breakthroughs.

Analysis of lipid membranes can be further classified into three important areas of investigation: lipid structure, bound water behavior, and interface characteristics. Each of these regions affects the bulk properties of the bilayer.

1.4.1 Lipid Properties

Simulation Dimensions

While running NPT, MD simulations of lipid bilayers, dimensions of the simulated box fluctuate while maintaining constant pressure and temperature. When initial values of atomic positions and velocities, and simulated box size, are chosen for a simulation, they are far from the equilibrium state. A simulated lipid bilayer is considered in equilibrium once the structural and thermodynamic properties become independent within fluctuations of the time. Box area (A) is therefore monitored as the simulation runs, to ensure simulations are not stopped until a sufficient portion of the simulation is available in which fluctuations of A are independent of time.

In addition to being a simple measurement to extract and use to determine equilibrium, the A also fluctuates around an equilibrium position with a deviation (σ_A^2) proportional to its compressibility. To compute the compressibility modulus of a simulated bilayer, we use the equation

$$K_A = \frac{Ak_bT}{\sigma_A^2}, \tag{1.17}$$

Where k_b is Boltzmann's constant and T is the temperature of the bilayer [25].

Calculation From Number Densities

Given the exact position of each atom that an MD simulation provides, the number density for each type of particle can be calculated. By number density, we mean the average number of particles of a particular type, which are in a unit volume. Since simulated systems of lipid bilayers are generally uniform, particularly at scale, the number densities of groups of particles are computed for each "slice" of the simulation. By the slice, we mean the even partitioning of the simulated box along the z dimension into even portions with the same cross-sectional area. Number density plots such as the example in figure 1.5, give the researcher insight into the localization of a particle. For example, we see in figure 1.5 the number density of water oxygen atoms (OW) denoted with the green $\times$'s that go to zero as they approach the center of the bilayer. This is expected since the center of the bilayer is hydrophobic. The integration of the number density between two z slices, times the x–y cross-sectional area, results in the number of atoms in the region integrated over.

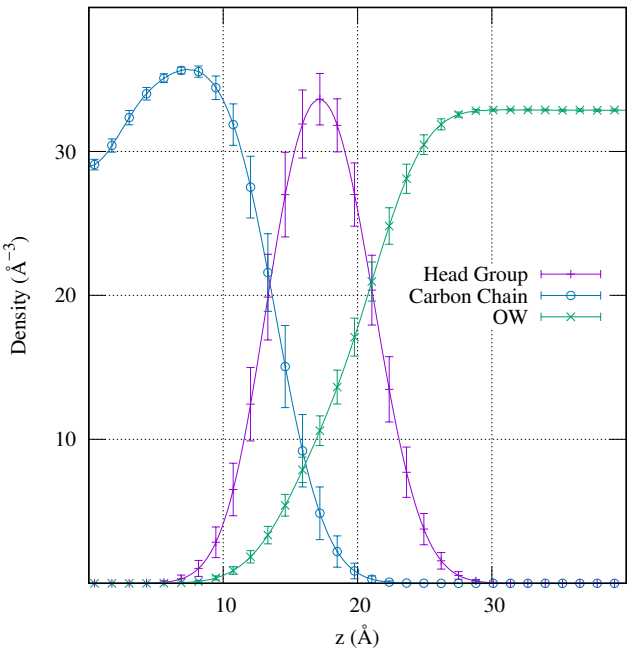

Figure 1.5: Number density of the (blue ·) hydrocarbon chains, (purple +) head group and glycerol atoms, and (green ×) water oxygen as a function of distance from the center of the bilayer z.

Number densities also provide a means of determining the size of bulk regions of the simulations which should approximate the size of the regions experiment. The partial molecular volumes of each type of particle is an important property used to derive other proportions. By partial molecular volume, we mean the volume taken up by the presence of a particle of a particular type.

One method to define the partial volume of a simulated particle could be to use the hard shell volume of the particles from the force field parameters. The problem of this definition is that the lowest energy state between two particles is rarely the sum of the hard shell positions. Therefore, the sum of this volume would not equal the sum of the simulated box. In order for a method of defining the volume to resemble that which is calculated from the experiment, the sum of the partial volumes times the number of each particle should equal the total volume. An even more helpful restriction might be, the sum of the partial volumes times the number of particles in a slice should be the volume of that slice. We now have a definition of partial volume for our simulations,

which defines them as the set of variables v_i which minimizes the equation

$$F(v_i) = \sum_{z_j}^{N_s} \left(1 - \sum_{i=1}^{N_p} n_i(z_j) v_i \right)^2 , \tag{1.18}$$

where $n_i(z_j)$ is the number density of the i–th particle type, N_s is the number of slices the simulation is divided between and N_p is the number of particle types that the simulation's particles are divided between. This method assumes that the particles in each group have the same partial volumes. This assumption is not necessarily true, even for atoms of the same type, *e.g.*, oriented water may take up more space than disordered water. Any error arising from this assumption is minimal. Therefore, we divide the lipid bilayer simulation into three groups: water, lipid head group, lipid hydrocarbon tails, for which we calculate the partial volumes of and multiply by the number of particles in each group to find the partial volume of the lipid head group (V_{hg}) and the lipid hydrocarbon chains (V_c) per lipid molecule.

With the partial volumes of the particles known, the thickness of the bilayer is the second structural property that can be calculated. By thickness, we mean the distance between opposite surfaces of the bilayer. This would be an easy calculation if it were not for the unclear meaning of surface. A bilayer is composed of a porous hydrophilic head group which adsorbs water. What we need is the distance between the Gibbs surfaces on each side of the bilayer. The simplest way to find this is first to compute the entire volume of bulk, then divide the volume by the cross-sectional area of the simulation, leaving the distance between the planes which would completely contain the volume. The total volume of the bulk is the integral of the number density times the partial volume as explained in the previous section. We, therefore, can calculate the thickness of the hydrocarbon chains ($2D_c$) as

$$2D_c = \frac{1}{A} \sum_{z_j}^{N_s} n_c(z_j) v_c, \tag{1.19}$$

where A is the area of the box, and v_c is the partial volume of the hydrocarbon chains. Likewise, the thickness of the lipid bilayer (D_b), can be found by subtracting the volume of water from the

total volume to find the volume of the bilayer as such

$$D_b = \frac{1}{2A}\left(1 - \sum_{z_j}^{N_s} n_w(z_j) v_w\right), \tag{1.20}$$

where v_w is the partial volume of water.

The area per lipid can now be determined by dividing $2D_c$ into V_c. This area per lipid is distinct from the box area because the lipid undulates, and therefore the area per lipid times the number of lipids is greater than the box area. The difference between these values is proportional to the amount of undulation in the bilayer.

Calculations from Electron Densities

In x-ray scattering experiments, the reciprocal space is directly recorded and is transformed back to the real space density via transform. Since the bilayer is symmetric, only the cosine portion of the transform is relevant. The transform of x-ray scattering gives the relative electron density ($\rho(z)$) since electrons best scatter x-rays. In the case of MD simulations, the real space locations of electron density can be calculated directly, since atoms are considered classical particles. Figure 1.6 is an example of an electron density from a DPPC simulation. We note that peak electron densities are around the phosphate region of the head group. The z dimension distance between these peaks is known as d_{hh} and is measured experimentally from the transformed density. Validation of simulations can be more accurately verified by computing the form factors ($F_m(q)$) from the simulated bilayer by taking the cosine transform of $\rho(z)$ using the equation

$$F_m(q) = \int_{-\infty}^{\infty} \rho(z)\cos(qz)dz. \tag{1.21}$$

We may then compare the transformed simulation data to the raw experimental raw data for better validation of the model.

Hydrocarbon Chain Order Parameters

As described in section 1.2.3, NMR experiments can measure the carbon chain order. Since simulations have access to the positions of the carbon atoms, the order of the chains can be com-

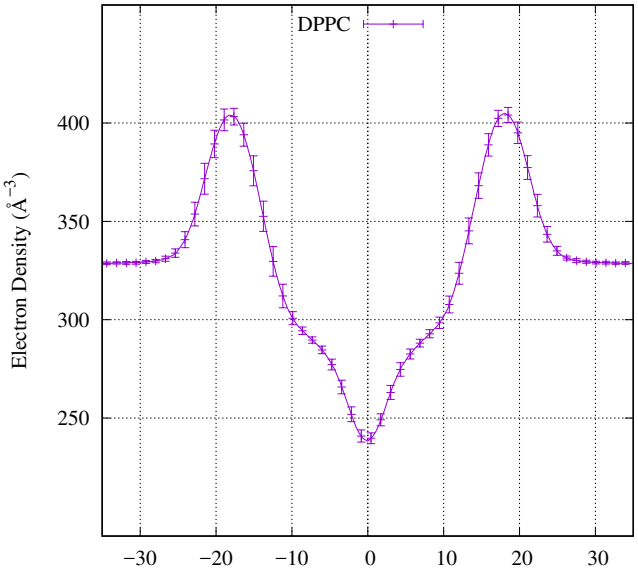

Figure 1.6: Electron density of a simulated DPPC lipid bilayer as a function of the distance from the center of the bilayer z.

puted directly. The order parameter for each pair of carbon atoms on the hydrocarbon chain C_{n-1} and C_{n+1} is a tensor $S_{\alpha\beta}$, where α and β are the chosen coordinates and, θ_α and θ_β are the angles between the vector connecting C_{n-1} with C_{n+1} and the unit vector in the α or β direction respectively. $S_{\alpha\beta}$ is computed using the equation

$$S_{\alpha\beta} = \frac{1}{2}\langle 3\cos(\theta_\alpha)\cos(\theta_\beta) - \delta_{\alpha\beta}\rangle. \tag{1.22}$$

To compare to NMR experiments, the S_{zz} components of the tensor are computed using the equation

$$S_{zz} = \frac{3}{2}\langle cos^2(\theta_z)\rangle - \frac{1}{2}. \tag{1.23}$$

The highest order possible is one and is attained when the vector between C_{n-1} and C_{n+1} is in the same direction as the vector normal to the bilayer. An order of zero means that the orientation is isotropic.

P-N Angle

The head group of a lipid is not straight but is a flexible region of the lipid. In the presence of polar or charged particles, the angle of the head group has been shown to change. It is believed that this might be used by the cell as charge sensors. To measure the angle of the lipid head group, we compute the angle between the vector pointing from the phosphate atom to the nitrogen atom and the normal vector $\hat{\mathbf{z}}$ of the bilayer. These measurements can be compared to Phosphate-31 NMR experiments which are used to measure the angle of the head group experimentally.

1.4.2 Water Properties

Lipids bilayers, *in vivo*, are a material adsorbed by water. Due to the combination of hydrophobic and hydrophilic interactions, water aids in the stability of the structure of a lipid bilayer. The absorption of water in the head group region also denatures typical bulk water behavior. Therefore, a critical focus of understanding lipid function is understanding water behavior.

Perturbation of Water

NMR experiments of bulk water show it has no net orientation, *i.e.*, bulk water is isotropic. As water approaches either an anionic or zwitterionic lipid, the polar water starts to become perturbed. This perturbation can be thought of as a net orientation of water. The orientation can be broken into ranks which correspond to the equivalent rank of spherical harmonics. In MD simulations, this ordering can be measured by first choosing a principal frame of the water molecule. Typically the principal frame is chosen to be the dipole moment or the vector from one of the hydrogen atoms to the oxygen atom ($O \rightarrow H$) of the water molecule. We then find the angle (β_{Bp}) between the principal frame and the director frame, the vector normal to the surface of the bilayer. Each rank can then be calculated as the expectation value of the Legendre polynomial of the cosine of the angle β_{Bp}. Therefore the first rank order parameter is $\langle\cos(\beta_{Bp})\rangle$, and the second rank is $\langle\frac{1}{2}(3\cos^2(\beta_{Bp}) - 1)\rangle$. The first rank order parameter for water, being the first spherical harmonic, corresponds to whether the principal frame is pointing more inward, towards the bilayer, for positive values, or outward, away from the bilayer, when values are negative. The second rank

order parameter, being the second spherical harmonic, corresponds to how much the principal frame is oriented parallel vs. perpendicular to the bilayer.

Åman *et al.* [26] demonstrated the quadrupole splitting ($\Delta\nu$) of a simulated system can be inferred from the second rank order parameter of the simulation so that the perturbation of water can be compared to results from NMR experiment. To derive $\Delta\nu$, Åman *et al.* used the second rank order and split the order into positive (B_+) and negative (B_-) regions [26]. The average second rank order parameter in each region was multiplied by the fraction of the total simulated water that was in each region. $\Delta\nu$ is then the absolute value of this sum times 3/4-th the quadrupolar coupling constant of water (χ =220 kHz). Using a simulated DPPC lipid bilayer, this process gave a $\Delta\nu$ which matched well with experiment [17].

In our work, we have improved on this system for calculating $\Delta\nu$. Rather than averaging the order parameter for each entire region and finding the water density in that region, we instead multiply the second rank order parameter by the water density to achieve the total weighted order parameter. We then sum each slice of the weighted order parameter. The absolute value of which, multiplied by 3/4-th the quadrupolar coupling constant of water, results in the estimated $\Delta\nu$. This technique is an improvement for several reasons. First, density is not uniform across the bilayer; therefore, assuming the average order parameter of the region skews the actual average. Second, the error in the boundary between these regions results in considerable differences in the final result.

Lateral Diffusion

The Diffusion coefficient quantifies the translational mobility of water. Lipid bilayers act as a barrier to this diffusion in the direction normal to its plane. The diffusion through a lipid bilayer is dependent on the permeability of the bilayer which is low enough that it is unlikely to occur in an MD simulation on reasonable time scales. Diffusion in the remaining two dimensions is known as lateral diffusion. Lateral diffusion is much easier to measure in simulated time scales and gives insight to the increased viscosity of water.

To compute the lateral diffusion of targeted water in a simulation, the oxygen atom of the targeted water is tracked for some time δt. The lateral mean square displacement (C) is then calculated as a function of time $C(t) = \langle|\rho(t) - \rho(t_0)|^2\rangle$, where $\rho(t)$ is the lateral displacement of

the atom, averaged over all target waters. The lateral diffusion, defined by the equation

$$D^{lateral} = \frac{1}{4}\frac{\langle|\rho(t_0+\delta t)-\rho(t_0)|^2\rangle}{\delta t}. \tag{1.24}$$

where $D^{lateral}$ is therefore the slope of measured $C(t)$.

Orientational Motion

Autocorrelation of the O-H vector ($\vec{v}_{OH}$) of a water molecule is useful to classify its orientational motion. Longer autocorrelation times denote water is more frozen. The characterizing function to autocorrelation is

$$C_1^{O-H} = \langle P_1(\vec{v}_{OH}(t_0)\cdot\vec{v}_{OH}(t))\rangle\,, \tag{1.25}$$

where P_1 is the first Legendre Polynomial. The expectation value is the average of all water oxygen tracked for some given time. This function can also be derived for the set of water in a particular region, of example the head group region of the bilayer.

The simulation can also be broken into slices. Since water molecules are likely to enter or leave slices during the time they are tracked, the resulting function $P_1(\vec{v}_{OH}(t_0)\cdot\vec{v}_{OH}(t))$ is computed and added to the average of each slice, weighted by the fraction of the time it has spent in that slice. Therefore, slices where water spends 100% of the tracking time in a slice, receive 100% of the function while slices in which water spends no time in receive 0%.

An example of the resulting characterizing function is shown in figure 1.7. This function is a multi-exponential decay with a term for each mode of orientational motion. It has been found that a three-term exponential function such as

$$A_1e^{-t/\tau_1} + A_2e^{-t/\tau_2} + A_3e^{-t/\tau_3}, \tag{1.26}$$

where τ_1, τ_2, and τ_3 are the correlation times and A_1, A_2, and A_3 are weights to the particular mode of rotation. The weight parameters have the additional restrictions that they are all positive and must add up to one. We must also note that if any of the correlation times are near the time step of the simulation, the value will have a large uncertainty. Although these values cannot

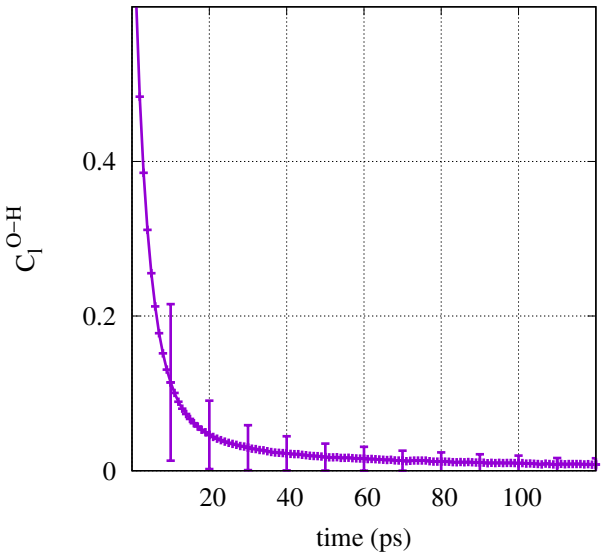

Figure 1.7: An example of the autocorrelation function taken from water molecules 24-26 Å from the center of a DPPC bilayer.

be matched directly to experimental values, these values are directly connected to NMR-water relaxation experiments.

1.4.3 Interface Properties

Electrostatic Properties

In MD simulations, we are not able to measure electrostatic potentials directly and therefore must deduce them from charge densities available, since both positions and charges are known for all atoms. We can again simplify the system as a one-dimensional problem by assuming that the charge of the system is reasonably homogeneous in slices parallel to the bilayer. The electrostatic potential is, therefore, the solution to the Poisson equation, with appropriate boundary conditions in one dimension as such

$$\frac{\partial^2 \phi(z)}{\partial z^2} = -\frac{\rho(z)}{\epsilon_0}, \tag{1.27}$$

where $\phi(z)$ is the potential and $\rho(z)$ is the charge density. The general solution to this equation is obtained by integrating the equation twice. The resulting function is

$$\phi(z) = -\frac{1}{\epsilon_0}\int_0^z \int_0^{z'} \rho(z'')dz''dz' + C_1 z + C_2. \tag{1.28}$$

To determine the exact solution, two boundary conditions must be applied. The first condition is that the potential of bulk water is zero. This is done, when a system has the bilayer near the center of the simulation, by setting the boundary of the solution to zero. The second boundary condition typically applied is the assertion that the electric field is zero in bulk water. We have found in previous work that this assumption is inaccurate, especially for large systems or systems with ions in bulk water. This is because there are small differences in charge density between slices which result in small electric fields. To ignore these small fields is to incorrectly choose C_1 which, since multiplied by z, becomes significant in large simulations. We, therefore, choose C_1 to zero the average electric field in bulk water by computing it from the first integral of the charge density.

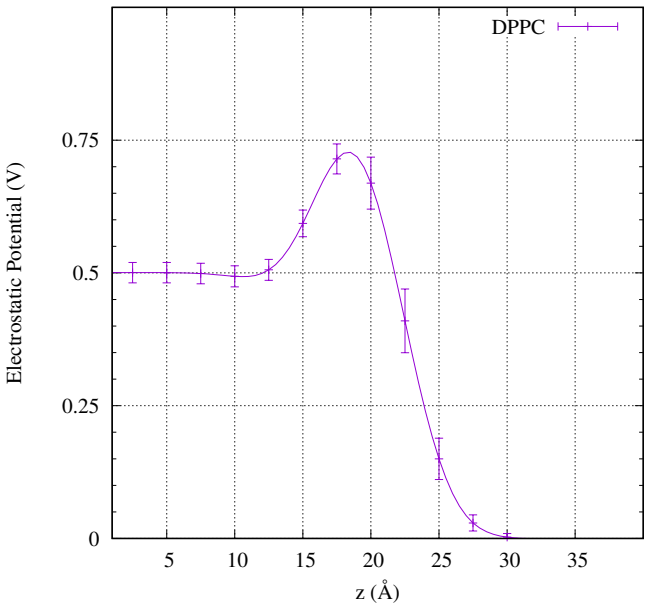

Figure 1.8: Electrostatic potential compared to the center of bulk water as a function of distance from the bilayer z.

Figure 1.8 plots the result of the solution to the Poisson equation, ϕ vs. the distance from

the center of a simulated DPPC bilayer. The height of the potential at the center of the bilayer represents the dipole potential and is likely closest to the potential measured experimentally. The electrostatic potential of the peak is the largest potential needed to be overcome by a charged particle to penetrate the bilayer.

Pressure Profile

To understand the mechanical stresses that a bilayer experiences, the pressure profile or local pressure tensor is calculated. Pressure profiles of MD simulations are complicated and require choices which can sometimes arrive at different results. Pressure profiles $P^{\alpha\beta}$ can be broken up into configurational $P_C^{\alpha\beta}$ and kinetic contributions $P_K^{\alpha\beta}$, as seen in the equation

$$P^{\alpha\beta} = P_K^{\alpha\beta} + P_C^{\alpha\beta}. \tag{1.29}$$

The kinetic contribution from the i–th particle is equal to the outer product of the velocity with itself times the mass of the particle and the delta function around the position of the particle (r_i)

$$P_K(r)^{\alpha\beta} = \sum_i m_i v_i^\alpha v_i^\beta \delta(r - r_i) \tag{1.30}$$

The configurational component to the local pressure tensor can be expressed as

$$P_C^{\alpha\beta}(\vec{r}) = \sum_i f_i^\alpha \int_{C_{0i}} \delta(\vec{r} - \vec{l}\,)\ \ \vec{ds}^\beta, \tag{1.31}$$

where f_i^α is the forces are acting on the i–th particle, $\int_{C_{0i}} \delta(\vec{r} - \vec{l}\,)\ \ ds^\beta$ is the line integral of a delta function along an arbitrary path C_{0i}, from a common reference point r_0, to the particle i, at r_i; $\vec{l}$ is the position vector of the line element, and $\vec{s}$ is the line segment of the contour. The expression can be simplified with two assertions. First, we assume forces that are acting on the i–th particle are pairwise interactions $\vec{f}_{ij}$. Second, since the choice of the contour is arbitrary, we force the contour to pass through the j–th particle of the pairwise force. Since the configurational energy must be invariant under translation, the portion of the line integral from the arbitrary start point to the

j–th particle, must be zero [27, 28]. We are therefore left with the equation

$$P_C^{\alpha\beta}(\vec{r}) = -\frac{1}{2}\sum_{i\neq j} f_{ij}^{\alpha} \int_{C_{ij}} \delta(\vec{r} - \vec{l}\,)\ ds^{\beta}, \tag{1.32}$$

where C_{ij} is the contour between the i–th and j–th particle for the pairwise interaction f_{ij}^{α}. This contour is not uniquely defined. The most common contour used is the Irving-Kirkwood (IK) which is taken as the shortest path between the two particles $\vec{r}_{ij}$.

If we again assume the system is homogeneous, we can compute the local pressure tensor for each slice z parallel to the bilayer with volume V using the equation

$$P^{\alpha\beta}(z) = \sum_{i\in z} m_i v_i^{\alpha} v_i^{\beta} - \frac{1}{V}\sum_{i<j} f_{ij}^{\alpha} r_{ij}^{\beta} w(\vec{r}_i, \vec{r}_j, z, dz), \tag{1.33}$$

where $w(r_i, r_j, z, dz)$ is a function that computes the fraction of r_{ij} that lies in slice z.

Additionally, we have stated that all forces considered are pairwise. MD simulations allow for angles and dihedral forces which are three and four body interactions respectively. The solution to this restriction is to use a form of force decomposition. Decomposition is the method to extract a set of pairwise forces which can be used to replace the multi-body interaction. The method of decomposition is not unique, but should at least fit restrictions that the decomposed force on i from j should be equal in magnitude as the force on j from i. Also, the direction of the force on i from j should be in the same direction as the displacement between them. Recent work by Vanegas *et al.* [29], showed the Goetz and Lipowsky force decomposition [27] results in the most accurate results.

Another issue arises from long-range electrostatic forces which for performance, are computed via Ewald summation. This summation computes the resulting force from all long-range interaction simultaneously and has no single source for the contour to come from. One partial solution to this issue is to choose Harasima contour, whose path is divided into a path parallel to the chosen slices, and an entirely perpendicular path. Choosing this path allows one to compute the lateral contribution to the pressure profile since despite not having a source for the force, we can say the perpendicular portion of the contour will remain entirely in the slices of the i–th particle. However, since the parallel portion must traverse through an unknowable number of slices, the z component

of the pressure profile is unobtainable. The total z component of the pressure profile, for NVT or NAPT ensembles, should be the normal pressure. Throwing away this component loses confirmation of this fact, as well as details about other contributions to the profile. This component is vital to calculations such as surface tension and therefore the Harasima contour is not ideal when accurate surface tension calculations are needed. Another, more computationally expensive, way around the issue of long-range electrostatic forces, is to extend the cutoff for computing the electrostatic forces explicitly in the pressure profile calculations. In the following work, we will use more considerable cutoff distances for our electrostatic forces.

Surface Tension

Surface tension can be computed from a pressure tensor by finding the difference in the pressure normal to the surface ($P_n(z) = P^{zz}(z)$) and the pressure lateral to the surface ($P_l(z) = (P^{xx}(z) + P^{yy}(z))/2$) [30]. This can be done for the local stress tensor of each slice computed above to determine the partial surface tension contribution from each region of the system. The total surface tension of the system is then calculated as the integral (or sum in the discrete case) of the difference between the normal pressure and lateral pressure. Positive surface tension indicates the system desires to decrease the surface in order to reduce the energy of that system.

1.4.4 Averaging of Binned Values With Varying Bin Widths

In constant pressure simulations, or at a minimum, simulations whose normal pressure is sustained by adjusting the normal dimension. When analyzing the trajectories of these simulations, measurements are sampled for a fixed number of bins. The result of these facts is that the dimensions of the boxes along the normal z-direction, which contain the measured values, are not the same. Further, the beginning and ending positions of the N-th bins from two-time frames of the same simulation, will not match, and especially for the large simulations we have produced within this work, will match better with other bins in other positions. For example, the N-th bin in the first time frame might be between 30 and 31 Å while the N-th bin from the second time frame is between 24 and 24.8 Å.

Therefore, before we can average the sampled values across different time frames, we must first normalize the samples across a uniform set of bins, all with the same positions along the normal

(z_j) with a shared bin width ($z_{j+1} - z_j$ is constant for any j). To convert a set of the original values (V_i) from a time frame with bins z_i, to a set of values (V_j) in the new set of bins z_j, we just, for each new bin, add all the all the original values, V_i, times a weight, W_i, which is proportional to the fraction of the new bin (z_j to z_{j+1}) overlaps with the bin whose value we are adding (z_i to z_{i+1}), see figure 1.9. We note that when the new bin fits entirely inside an old bin, its value is the value of the bin which is fits inside. When a new bin is split, in a way that half of it lies in two original bins, the new bin with have the average value between those bins.

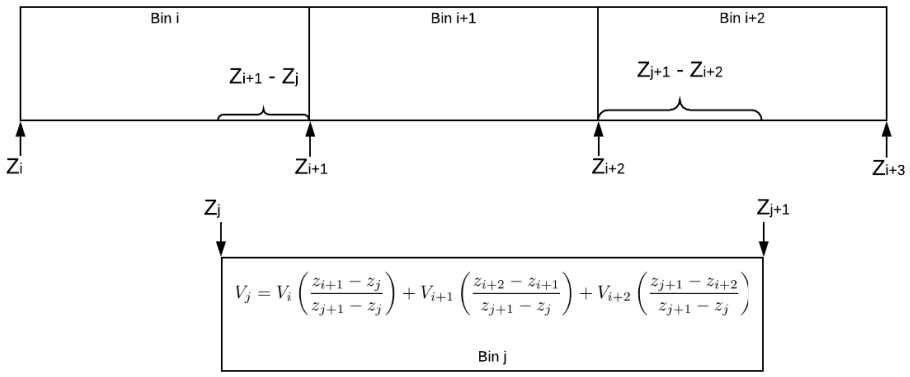

Figure 1.9: A drawing depicting the method of normalizing the bin widths of simulation sampling.

In figure 1.9 we see the more general approach, whereby the sampled value of the new bin V_j is computed as the weighted average of the values in the overlapping bins, according to the equation

$$V_j = V_i\left(\frac{z_{i+1}-z_j}{z_{j+1}-z_j}\right) + V_{i+1}\left(\frac{z_{i+2}-z_{i+1}}{z_{j+1}-z_j}\right) + V_{i+2}\left(\frac{z_{j+1}-z_{i+2}}{z_{j+1}-z_j}\right). \tag{1.34}$$

Once all measurements have been converted to the same bin widths, we are then able to confidently compute averages and standard deviations of the samples, knowing that summing the values in the N-th bin represents the same position in the simulation. This technique was used for all intrinsic samples which were dependent on the distance from the center of the bilayer z, before averaging and plotting, unless otherwise noted.

1.5 Conclusions

Lipid membranes are important biological structures whose properties depend on which lipids are present as well as the composition of the surrounding solvent. Experimental techniques measure macroscopic properties of the bilayer while computational techniques give insight into the microscopic mechanisms that give rise to the bulk properties. This work examines the results of MD simulations of lipid bilayers to better understand how lipid molecular structure and solvent salt concentrations affect the membrane properties.

Chapter 2

Ether-Lipid Bilayers

2.1 Introduction

The wide variety of lipids used by different organisms implies that lipid makeup is a specialization which provides advantages. One of the earliest examples of this specialization can be found in the difference in the domains of eukaryotic and prokaryotic from that of archaea. While eukaryotic and prokaryotic cells are formed from mostly ester linked lipids, archaea have ether-linked lipids [6]. This divergence is believed to have occurred around the time of the last universal common ancestor (LUCA) [6]. Although the exact reason for this split in lipid types is not known, there are a few possible advantages that could have been the basis of the evolution. For one, ether lipids tend to be less permeable and therefore may have given an advantage in environments of chronic energy stress [10]. Although not true for all, many extremophiles are members of the archaean domain. Lipid composition might be a result of the extreme environments in which these archaea evolved. Another specialization advantage may be from ester lipids with increased lateral diffusion which gave eukaryotes advantages in photosynthesis, respiration and signal transduction [10]

Although ether lipids are rare in eukaryotic and prokaryotic cells, they are not absent. For one, these lipids exist in human cells in the form of plasmanyl and plasmalogen [5] lipids. These lipids contain a single ester, and a single ether or vinyl, bonded chain. These lipids are most prevalent in specialized human tissue such as brain and heart [5]. and they are believed to affect lipid raft formation [31] and oxidative damage [32], but their entire function is not fully understood [33].

To better understand how changing a particular moiety of a lipid affects the macro properties of a bilayer, it is ideal, to work with lipids which are identical in every way except for the difference in the area of interest. Although not always possible, this control allows a researcher to isolate the result of the difference in chemical structure. Ideal candidates for exploring the changes in bilayers when constructed with ether vs. ester bonded lipids are dipalmitoylphosphatidylcholine

(DPPC) and dihexadecylphosphatidylcholine (DHPC). These lipids both are fully saturated with phosphatidylcholine head groups, as well as a glycerol backbone. Both hydrocarbon chains of both lipids have the same chain length of 16 carbons. The only difference is between them is that DPPC has fatty acid chains that are connected with ester bonds, while DHPC has two hydrocarbon chains connected with ether bonds.

These lipids were studied experimentally by Gawrisch *et al.* [17], Guler *et al.* [34], Balleza *et al.* [35], and Pan *et al.* [36]. Gawrisch *et al.* [17] measured a difference in dipole potential and determined DPPC was 118 mV higher than DHPC. NMR readings from small amounts of deuterated water at the surface of the bilayer produced larger quadrupole splitting, and therefore more ordered water, in DHPC than DPPC. X-ray scattering was used by Guler *et al.* [34] which gave a basis for the structural parameters of DPPC. DHPC was found to be a thicker bilayer in its fluid phase. The permeability of DPPC was much higher than that of DHPC. Balleza *et al.* [35] further tested permeability with experiments of both polar and nonelectrolytic ions, again confirming the decreased permeability of DHPC over its ester bonded equivalent. Work by Pan *et al.* [36]

It was shown that, since the difference in thickness between the two bilayers was much smaller than the difference in permeability, the three slab theory [37] was more accurate at predicting the permeability of these bilayers. However, Guler *et al.* [34] were not able to determine if the smaller permeability of DHPC was from a larger minimum area per lipid A_0 or a smaller diffusion coefficient of water in the unobstructed portion of the head group region (D_{head}).

Henceforth, we will refer to the broad class of lipids with both chains attached via ether bonds, such as DHPC, as an "ether lipid," while referring to the class of lipids with two ester bonded hydrocarbon chains as "ester lipids."

Several Molecular Dynamics (MD) studies have been performed on various ether lipids. Shinoda *et al.* [38] used Molecular Dynamics (MD) to simulate branched ether and ester lipids, and calculate the dipole potential and free energy barrier for a water molecule. Additionally, the previously mentioned work by Pan *et al.* [36] included MD simulations of un-branched ether and ester lipids with and without cholesterol. These simulations showed the OH group of cholesterol in ether lipid membranes associate with phosphate oxygen, while in ester lipids they associate with the carbonyl oxygen.

In this study, we examine the structure of simulated ester and ether lipid bilayers via Molecular

Dynamics (MD). Electrostatic potential calculated for the two bilayers affirms the higher dipole potential of DPPC bilayers. However, it also indicates that DHPC has a higher potential barrier. The more substantial potential barrier of DHPC bilayers may contribute to its lower permeability. We observe that water in DHPC is more ordered and has slower translational and rotational motion. These results point to a less free water layer within the head group region which is perhaps the main contributor to the reduced permeability of the DHPC bilayer.

2.2 Simulations

Two homogeneous, hydrated lipid bilayers were simulated using Molecular Dynamics (MD). One bilayer was composed of 200 DHPC lipids, and the other was composed of 200 DPPC lipids. Figure 2.1 is a model representation of the lipids used for these bilayers. These lipids differ only in that DPPC has the oxygen carbonyls as part of the ester bond, while DHPC has only the ether bond. They both share the same phosphatidylcholine head group and glycerol backbone and have fully saturated 16 carbon chains. These systems were simulated with a large hydration layer of 150:1 SPC/E water to lipid ratio. Systems were constructed by creating a bilayer leaflet, placing 100 lipids on a 10 by 10 grid, then making a second mirror image of original leaflets tails, and finally filling the space above the leaflet with SPC/E water.

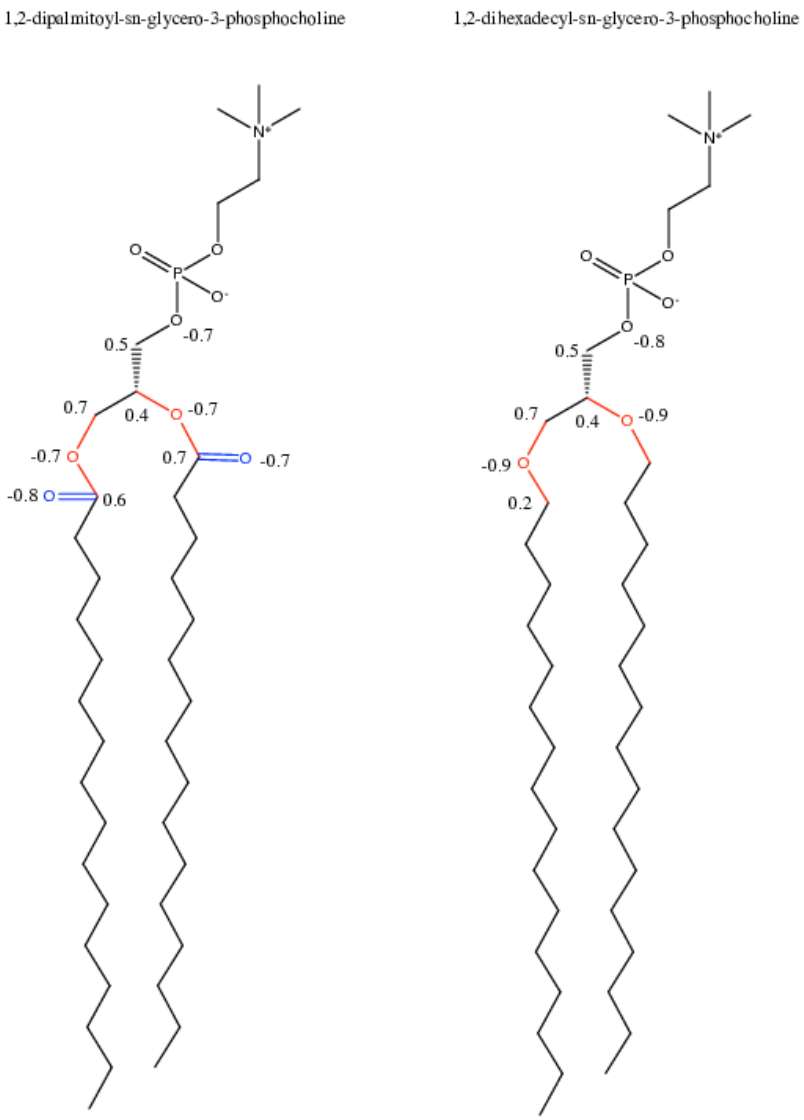

Figure 2.1: Line drawings of DPPC (left) and DHPC (right) lipids. The numbers next to atoms show the partial charges used for the corresponding atom in the simulation.

Simulations were performed using the GROMACS package, version 5.0 [39]. Systems were energy-minimized to remove bad contacts from stretched bonds and overlapping hard sphere surfaces. The systems were then equilibrated by performing four 50 ps runs. First, the systems were simulated with NVT ensembles of small 1 fs steps to ensure that the bilayer did not blow up in subsequent runs. Next, two NAPT ensemble runs ensured that the bilayers would not break apart before settling. These runs were performed by decreasing the compressibility in the z-dimension from 4×10^{-5} to 4×10^{-10}, followed by an increase to 4×10^{-8}. Finally, an NPT ensemble was simulated using a 2 fs time step to ensure complete equilibration. The systems were annealed by performing 250 ps runs at 400 K, and reducing the temperature to 330 K with steps of 10 K. Each temperature step was simulated for 250 ps.

Once the systems were adequately annealed, 200 ns of continuous MD simulations were performed. The pressure was held at 1 atm using Parrinello-Rahman semi-isotropic pressure coupling [21], while the temperature was held at 323 K for both systems, using the Nosé-Hoover temperature coupling scheme [20]. All bonds in the system were constrained using the LINCS algorithm [40] which allowed for an integration time step of 4 fs. Boundary conditions in all three dimensions were periodic. The long-range electrostatics were computed using SPME algorithm [41]. Cutoffs of the real space electrostatic and Van der Waals interactions were set to 10.0 and 16.0 Å respectively.

We used 42A1-S3 lipid force field developed by our group [24] for both DPPC and DHPC lipids. The DHPC lipids needed re-computation of partial charges. The partial charges were computed using GAUSSIAN 03 [42] on 15 randomly generated DHPC head group and methyl-terminated backbone structures. All the structures were first geometry optimized at B3LYP level with 6-31G (d,p) basis set. The partial charges obtained using Mulliken population analysis were averaged and rounded to produce neutral charge groups. The final partial charges used in the simulations are presented in figures 2.1 and 2.2.

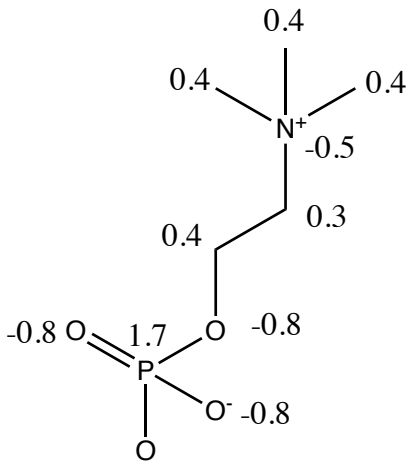

Figure 2.2: Line drawing of the Phosphocholine Head Group shared by both DPPC and DHPC. The numbers next to atoms on the line drawing show the partial charges used for the corresponding atom in the simulation.

2.3 Analysis

2.3.1 Lipid Properties

The geometric area (A) of the simulated bilayers were measured for the entire simulation to ensure the lipid reached thermal equilibrium. The area of each simulation at each step is shown in figure 2.3. The compressibility of each bilayer can be inferred from fluctuation in the box area. DPPC has a visibly more large deviation of A, and therefore we expect it is more flexible than DHPC. The compressibility modulus of DPPC was computed to be 359 dyn/cm while DHPC was computed to be 418 dyn/cm using the method described in section 1.4.1. Since DHPC has a higher compressibility modulus, it requires more energy to change its area. These moduli are similar to those computed from experiments by Rawicz *et al.* [43].

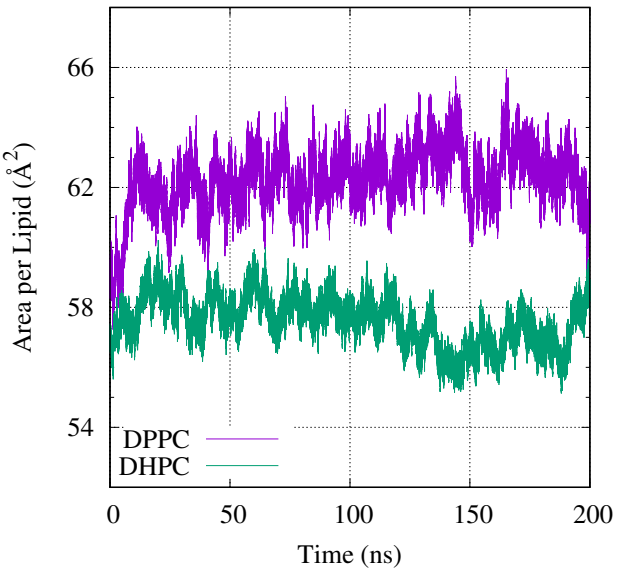

Figure 2.3: The simulated box area, in Å, of the lipid bilayer simulations for DPPC (purple) and DHPC (green) as a function of time. The higher variance in the box area of DPPC corresponds with a higher compressibility.

Density, Volumes & Form Factors

Number densities for hydrocarbon chains, head groups, and water oxygens were calculated for each 5 ns run. The results of these calculations were averaged according to section 1.4.4, and are plotted in figure 2.4 for DPPC and DHPC. We note that water in the head group region of DHPC does not have a typical hyperbolic curve, but instead has an additional peak density around 18 Å. This feature is a signal that water behaves differently in DHPC and perhaps ether lipids in general.

These number density data are then used to compute the partial volume of each group of atoms as described in section 1.4.1. V_L and V_c are thus computed, and the resulting values are shown in table 2.1, rows V_L and V_c respectively. As expected, the similar chains of DPPC and DHPC both have the same V_c, while DHPC, with its missing carbonyl, has a slightly smaller V_L. Partial volumes of water v_w and hydrocarbon chains v_c were then used to compute the thickness of the bilayer as explained in section 1.4.1. These thicknesses are in table 2.1 rows $2D_c$ and D_b respectively. Hydrocarbon thickness $2D_c$ matches well with experimental data, in particular, DPPC. DHPC is slightly thicker than results published from Guler *et al.* [34]. Given V_c and $2D_c$, the area per lipid,

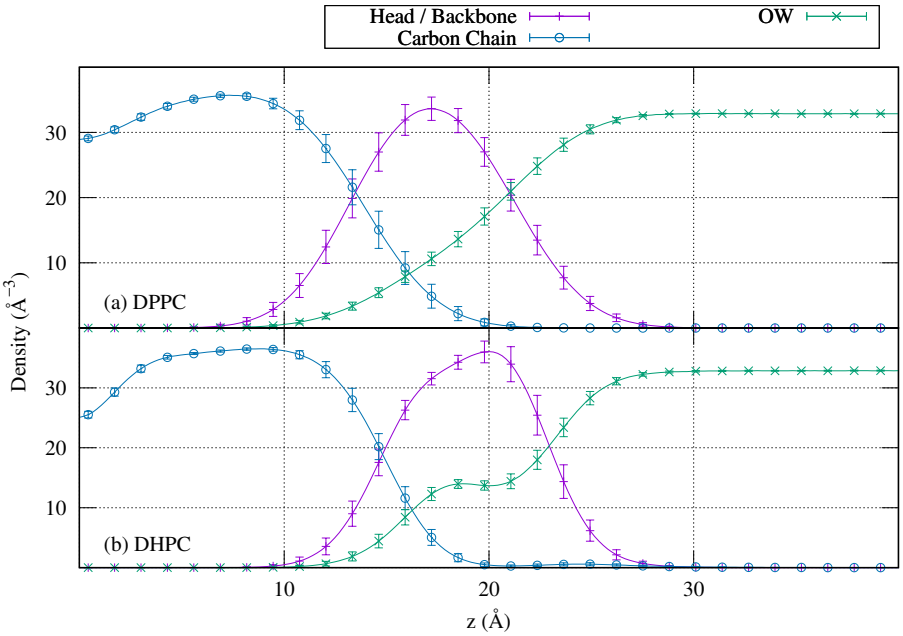

Figure 2.4: Atomic number densities of the head group and glycerol (purple —), hydrocarbon chains (blue ·), and water oxygens (green ×) as a function of the distance from the center of the bilayer (z) for (a) the DPPC simulation and (b) DHPC simulation.

A_l, calculated and is listed in table 2.1 row A_l. A_l is highly depended on $2D_c$; therefore, DHPC has a higher A_l due to the lower $2D_c$.

Electron densities were computed as described in section 1.4.1. The density per slice is displayed in figure 2.5. Electron densities, transformed from experimental form factors by Guler *et al.* [34], display a similar difference in electron density shapes. In particular, the inward bowing of the electron density of DPPC around 12 to 18 Å region.

From electron densities, D_{hh} was computed as the peak to peak distance in the figure and the results placed in table 2.1, row D_{hh}. This measure of thickness was smaller than equivalent experimental measurements for DPPC, though it is closer to experimental measurements expressed using the newer atomically detailed model (ADP) model defined by Fogarty *et al.* [14]. DHPC was slightly thicker than experimental results, though ADP model values are not available for DHPC. Electron densities were then transformed back to experimental form factors as described in section 1.4.1. Scaled form factors for DPPC (see figure 2.6a) match within error bars to both small and wide angle x-ray scattering data taken from work by Fogarty *et al.* [44]. DHPC form factors

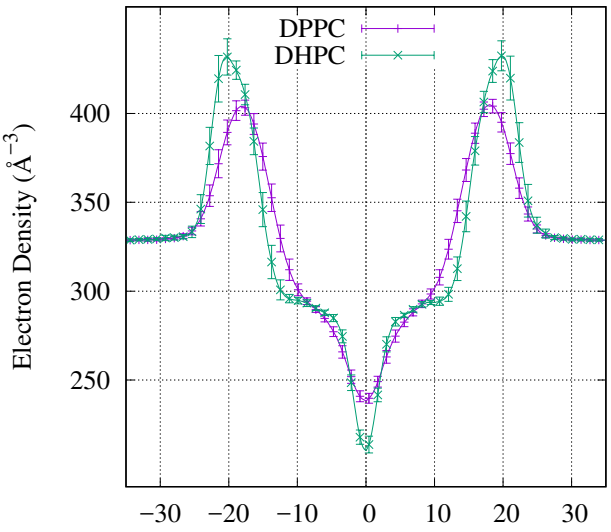

Figure 2.5: The electron density, from a region of the simulation, as a function of the distance from the center of the bilayer (z) for DPPC (purple) and DHPC (green). A region between -35 to 35 Å was chosen to focus on the lipid-water interface.

(see figure 2.6b), scaled to best fit with experimental data, were compared to experimental data by Pan *et al.* [36]. These data show a slightly smaller leading edge of the first peak which does not match the error bars. This feature corresponds to the higher $2D_c$ measure than the experiment.

P-N Angle

The angle of the lipid head group is of great interest since it contributes to the dipole potential, which is, a barrier to charged and zwitterionic particles. As the dipole of the head group moves from a parallel to perpendicular orientation, the dipole creates an additional obstruction to particles [45]. Additionally, the angle of the head group is believed to be a signaling mechanism for ion concentration for the cell. The angle of each head group was computed, as explained in section 1.4.1, and histograms of the P-N angles were constructed and shown in figure 2.7. The distribution of angles for both lipids appears to be Gaussian, with a peak (the mode) near 15 degrees from the plane of the bilayer. The most apparent difference between the distribution of angles of the lipids is that DPPC has a much broader distribution, signifying a more flexible orientation than DHPC, which

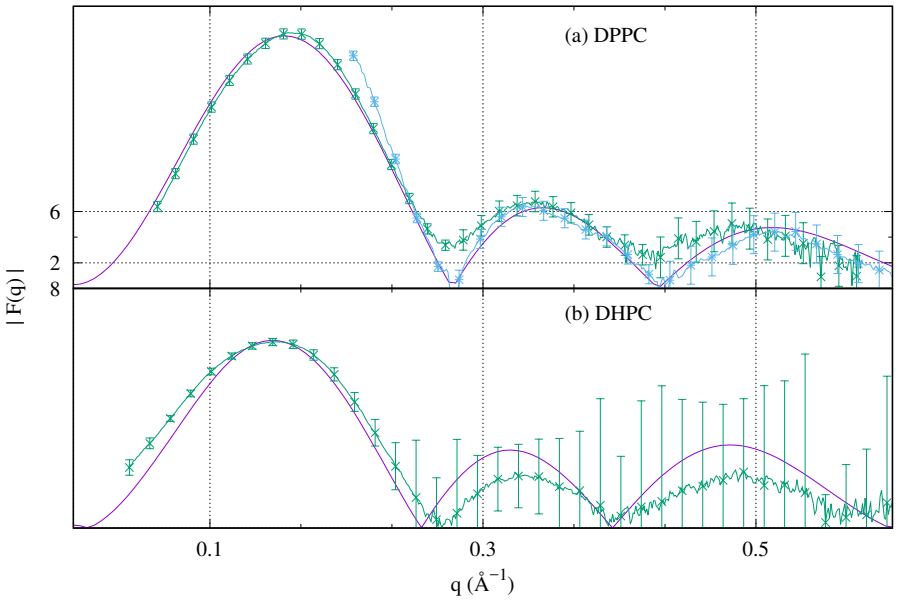

Figure 2.6: Form factor plots. (a) Form factor data for DPPC derived from the cosine transform of electron densities (purple) compared to scaled form factors of experimental measurements using unilamellar (ULV) (green) and oriented (ORI) (blue) x-ray diffraction. (b) Form factor data for DHPC derived from the cosine transform of electron densities (purple) compared to scaled form factors of experimental measurements using ULV (green) x-ray diffraction.

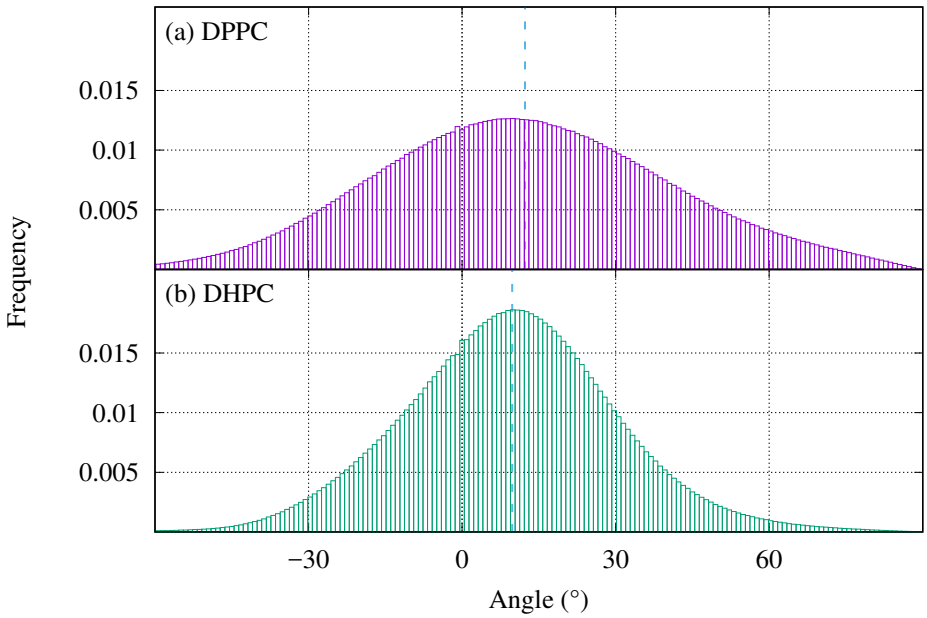

Figure 2.7: Histogram of the dipole angle, *i.e.*, the angle between the vector connecting the phosphate and nitrogen atoms, and the vector normal to the bilayer plane form (a) DPPC and (b) DHPC. The dashed line denotes the average (mean) dipole angle.

has a much sharper peak. Another notable feature of the DPPC distributions is the mean angle (denoted with a vertical dashed line) which is larger than the mode, or most frequent angle. This difference denotes a slight preference of straightening over compressing, of DPPC over DHPC.

2.3.2 Water Properties

Its charges perturb water surrounding the lipid head group while lipid area reduces from the matrix formed by the water. The balance of these actions gives insight into the structure and stability of the bilayer. First and second rank order parameters for water as a function of distance from the center of each bilayer were calculated as described in section 1.4.2. The results of these calculations are displayed in figure 2.8. The first rank order parameter figure 2.8 a, show both lipids orient the principal frame of the water molecule ($O \rightarrow H$) opposite the bilayer normal which is most notable for DHPC. The second rank order parameter, shown in figure 2.8 b, describes how perpendicular or parallel the principal frame is. These data show both bilayers orient water at the surface, outside of 20 Å from the center, as parallel to the bilayer. However, as they enter the D_b

	DPPC			DHPC	
	Guler *et. al.*	Fogharty *et. al.*	Our Simulation	Guler *et. al.*	Our Simulation
K_A, in dyn/cm	–	–	359	–	418
V_c, in Å^3	897	866	869 ± 5	897	870 ± 5
V_l, in Å^3	1229	1298.6	1229 ± 5	1223	1209 ± 5
$2D_c$, in Å	27.9	27.2	27 ± 1.0	27.6	29 ± 1
D_b, in Å	–	38.2	38.0 ± 0.5	–	40.3 ± 0.5
A_l, in Å^2	64.3	63.8	64.7 ± 1.0	65.1	60.0 ± 1.0
D_{hh}, in Å	37.8	37.0	36.0 ± 0.7	38.2	39.9 ± 1.0
P-N angle (deg)	–	–	12.3 ± 0.5	–	9.8 ± 0.6

Table 2.1: Table of physical properties measured from the simulated bilayer compared to properties derived from experimental data.Major columns separate results for DPPC and DHPC while minor columns separate experimental work from Fogarty *et al.* [44] and Guler *et al.* [34], and results from simulations described in this chapter. Rows include compressibility modulus (K_A) of the bilayer calculated from fluctuations in the geometric area, volumes of the hydrocarbon chains (V_c) and the entire lipid (V_l), thicknesses of the hydrocarbon chains ($2D_c$) and of the entire bilayer (D_b), area per lipid (A_l), peak to peak electron density separation (D_{hh}), and dipole angle measured as the angle between the P-N vector and the vector normal to the bilayer.

surface, they begin to favor a perpendicular orientation. DHPC, in particular, has a vast region of water positioned in this manner.

The second rank order parameter can also be used to estimate the quadrupole splitting ($\Delta\nu$) that would be measured from water NMR experiments. These calculations were made for ∼23 water molecules per lipid as described in section 1.4.2. The quadrupole splittings for the lipid simulations are listed in table 2.2. DHPC demonstrates significantly more quadrupole splitting than DPPC. This data is in agreement with experimental values by Gawrisch *et al.* [17]

Lateral Diffusion

The lateral diffusion of water should decrease in the head group region of the bilayer as the head group denatures liquid water, making it more viscous. We can find the relative viscosity of this perturbed water by measuring and comparing the lateral diffusion coefficients of water both inside the head group ($D_{head}^{lateral}$) and outside in the bulk water region ($D_{bulk}^{lateral}$) of the simulation using the process described in section 1.4.2. The location where the second rank water order went to zero, as calculated above, was used to delineate the regions. Target water molecules were tracked for 200 ps. Any water which moved out of the region during the 200 ps were rejected. Coefficients

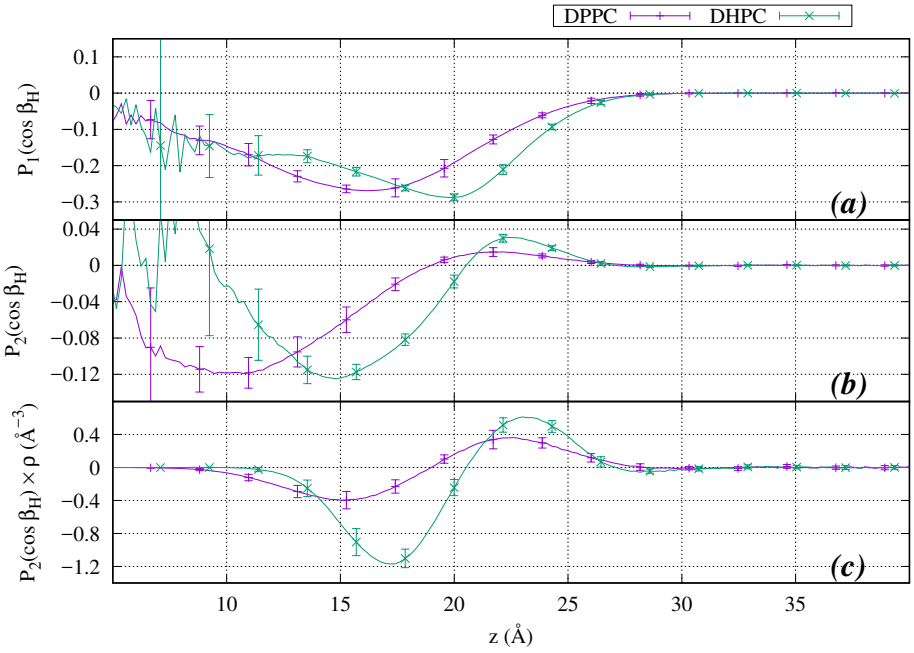

Figure 2.8: (a) First rank and (b) second rank order parameters as a function of distance from the center of the bilayer (z). (c) The product of the second rank order parameter and the density of water oxygen used for the estimation of $\Delta\nu$. Each figure includes plots for DPPC (purple) and DHPC (green).

were calculated from the middle 80% of the mean square displacement. Table 2.2 rows 2 and 3 list the lateral diffusion of water computed in the two regions of the two simulations. We note that the lateral diffusion of water in the bulk region , $D_{bulk}^{lateral}$, is the same for both simulations, but diffusion in the DHPC head group is smaller, meaning that the water in its head group is more viscous than that of DPPC.

Orientational Motion

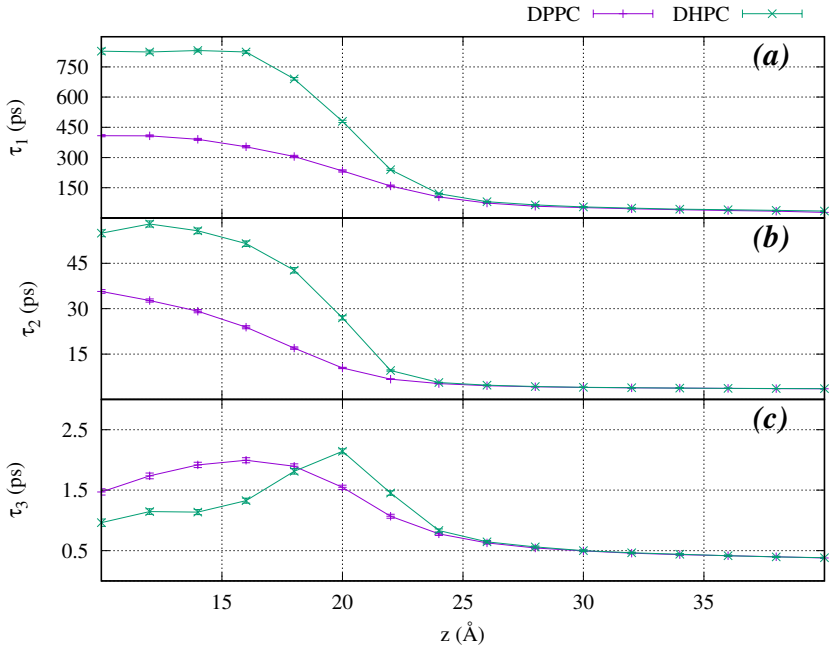

Figure 2.9: (a) long (τ_1), (b) medium length (τ_2), and (c) short (τ_3) time scale exponential fits the autocorrelation function as a function of the distance to the center of the bilayer z for an 80 Å region of the simulation about the center of the bilayer.

The principal O-H vector of water was used to characterize the orientational motion of water as described in section 1.4.2. This calculation was repeated for water in each 2 Å slice, from the center of the bilayer to the bulk water region, for each bilayer simulated. From this calculation, three correlation times τ_1, τ_2, and τ_3 were produced for each slice of each bilayer and plotted in figures 2.9. Figure 2.9 a is the longest correlation time while figure 2.9 c is the shortest. The shorter correlation time τ_3 is near the simulation step size and therefore should be considered the least reliable. Both lipids have a remarkable increase in the larger correlation times as water

transitions from bulk to the lipid head group. This increase seems to reach a maximum value by 17 Å from the center of the bilayer.

These max correlation times are reported in table 2.2. The max correlation times for DHPC are nearly double than that of DPPC. These longer correlation times again represent more viscous behavior of water in the DHPC head group, and in particular, shows that water in its head group is less likely to change its orientation.

	DPPC	DHPC
$\Delta\nu(Hz)$	210 ± 20	1280 ± 40
Water $D_{head}^{lateral}$ $(\times 10^{-9} m^2/s)$	0.94 ± 0.09	0.37 ± 0.03
Water $D_{bulk}^{lateral}$ $(\times 10^{-9} m^2/s)$	6.2 ± 0.1	6.1 ± 0.1
max τ_1 (ps)	408 ± 5	831 ± 7
max τ_2 (ps)	35.6 ± 0.6	58 ± 1

Table 2.2: Table of water properties measured from simulations. Columns for each simulation and a row for estimated water-NMR quadrupole splitting at 21 waters per lipid, lateral diffusion coefficients for bulk water ($D_{bulk}^{lateral}$) as well as water inside the head group region ($D_{head}^{lateral}$), and maximum values of the longest (τ_1) and second longest (τ_2) correlation times.

2.3.3 Interface Properties

Electrostatic Potential

The electrostatic potential as a function of the distance from the center of the bilayer was calculated by twice integrating the charge density as described in section 1.4.3. The results of the integrations are plotted in figure 2.10. We note in this figure that the "dipole potential," *i.e.*, the difference in potential between bulk water and the center of the bilayer, is 56 ± 5 mV more substantial for DPPC than DHPC. This larger dipole potential of DPPC is consistent with experiments by Klaus *et al.* [17] which showed an increased dipole potential with of DPPC. Figure 2.10 also demonstrates a peak potential increase in the head group region of the bilayer. This peak would create a more considerable potential barrier to diffusion of charged and zwitterionic particles, which explains in part, why DHPC has a lower permeability. Cordomi *et al.* [45] computed potential contributions from different components from simulations and showed that the positive contributions mostly come from water's dipole orientation in the head group region, and that lipid dipole reduced

the potential.

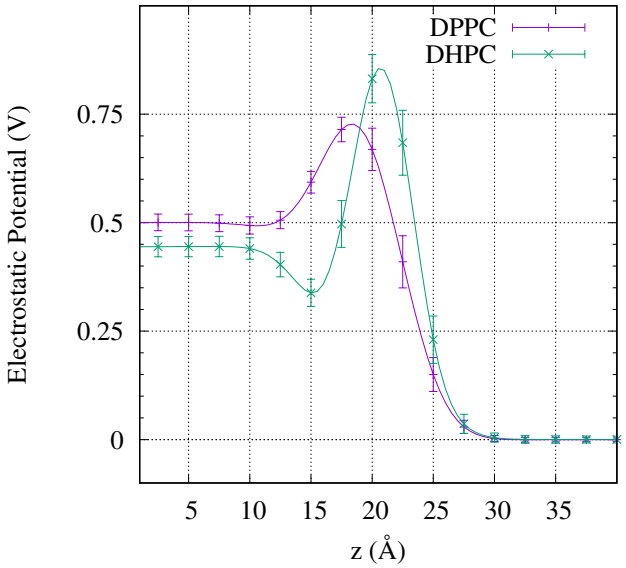

Figure 2.10: Electrostatic potential of DPPC (purple) and DHPC (green) as a function of the distance to the center of the bilayer (z).

2.4 Conclusions

"Ether lipids," lipids with ether bonded hydrocarbon chains, are an important feature in the "lipid divide," the specialization of lipid composition by archaea during earliest known evolution [7]. Ether lipids are important, since lipids with a single hydrocarbon chain bounded by an ether linkage are found in specialized tissue such as heart and brain cells. The existence of this linkage in human tissue, despite its small proportions, signifies a particular use for the bond.

The use of ether lipids may stem from their decrease in permeability. The mechanism driving the decreased permeability was not understood, since dipole potentials of ester bonded DPPC appeared to be higher than that of ether bonded DHPC lipids in experiments by Klaus *et al.* [17]. These experiments did show an increase in the quadrupole splitting of water in the head group of DHPC as opposed to DPPC [17].

In this chapter, we simulated the same lipids, DPPC and DHPC, as Klaus *et al.* [17], using force fields for DHPC derived from DPPC, tuned for glycero-phospholipids, with additional parameters

determined from Ab Initio Calculations. Results from DPPC match near perfect with experimental structural parameters, while results for DHPC are not as accurate and suggest further tuning of the ether force field is needed. Quadrupole splitting, calculated from DHPC and DPPC, fit both rather well, suggesting that water behavior is accurate for the simulations.

DHPC bilayers were shown to be more rigid in simulation compared to the equivalent DPPC bilayer. DHPC has a larger compressibility modulus and a smaller deviation of P-N angles. This rigidity of the ether bilayers could have some disadvantage compared to the ester lipids of bacteria and eukarya, where flexibility might have allowed for lipid dipoles to be used as charge sensors [46, 47].

Examination of the potential of the two bilayers, despite a smaller dipole potential, shows that DHPC has a higher peak potential which could be at least one contribution to the decreased permeability since this peak would be an additional barrier against charged and zwitterionic particles.

The most significant difference between the ether and ester bilayers is the behavior of the water in the head group region. Water in the head group of DHPC was more viscous and frozen than water in the head group region of DPPC. The viscosity was determined by an increase in the first and second rank ordering of water, a decrease in the lateral diffusion, and an increase of the lengthening of the orientation autocorrelation times of water as they approach the center of the bilayer. This immobilization of water may create a frozen layer of water at the surface of the ether bilayer, which would also contribute to the decreased permeability of ether lipids.

Work by Guler *et al.* [34] used a three slab theory [37] to explain the difference in permeability between DHPC and DPPC. In this theory, the higher permeability of DPPC would come from a smaller area per lipid A_0 or a larger diffusion rate in the head group (D_{head}). Work from this chapter suggests the mobility of water is greater in ester lipids and therefore D_{head}, would account for the difference in permeability.

Chapter 3

Lipid Bilayers in the Presence of Monovalent Ions

3.1 Introduction

Physiologically, lipid bilayers are not solvated in pure water. Typically, this water contains other minerals, most importantly salt ions. Biological materials for many physiological processes use salt ions. Lipid bilayers, as the primary barrier to diffusion, can regulate these functions by impeding the movement of ions. Also, due to the large charge densities of ions, lipid bilayers attract ions to their surface. This attraction creates a surface charge density on the surface of the bilayer. More importantly, the presence of ions in the head group region and surface of the bilayer affects the properties of the bilayer. The changes to the bilayer are dependent on the ion present. Salts are classified first into positively charged cations and negatively charged anions. In nature, Cl^- is the most common anion, while Na^+, K^+, Ca^{2+}, Mg^{2+} are the most common cations.

Li^+ is not a physiologically common ion, but it does have many significant affects on human physiology [48]. The most well known is that Li^+ has been used in the treatment of bipolar disorders since the 1950s [49]. Another important effect is Li^+ is toxic at far lower levels than other physiological salts [48]. The mechanisms of both of these effects are not yet known and therefore study of the binding properties of Li^+ compared to other salts is useful in understanding how to use Li^+ safely as a medicine.

Li^+, Na^+, K^+, and Rb^+ are all monovalent, alkali metal cations. That is to say, each of these ions is formed from an element in the first column of the periodic table losing a single electron, and therefore have a net charge of one proton ($+e$). The set Li^+, Na^+, K^+, and Rb^+ are listed in increasing atomic number, and consequently, increasing in atomic radius. In this chapter, we use these cations as variables in four identical simulations, in addition to a simulation without the presence of any salt in order to understand the effect of monovalent cation size, to the mechanical and electrostatic properties of the bilayer, as well as the binding locations of these ions. Finally, we

looked for differences in Li^+ which may explain many physiologically effects Li^+ has on humans.

The following experimental work has been done on zwitterionic lipid bilayers in the presence of monovalent ions. X-ray diffraction, EPR spectroscopy, differential scanning calorimetry, and dilatometry and velocimetry where performed on Palmitoyl-Oleoyl-Phosphatidylcholine (POPC) bilayers by Pabst *et al.* [50]. In this work, high concentrations of NaCl (about 500 mM) caused bilayers to thicken, and their areas contract. Fluorescence correlation spectroscopy and calorimetry on POPC bilayers, by Böckmann *et al.*, showed that with increasing ion concentration the lateral lipid decreases [51]. Infrared spectroscopic experiments by Binder *et al.*showed deep penetration of cations into the polar region of POPC bilayers, and that Li^+ better dehydrates the phosphate and carbonyl groups than Na^+ or K^+ [52]. ζ potentials of phosphatidylserine vesicles were measured, by Eisenberg *et al.*, in solutions containing monovalent cations [53]. Hydration repulsive pressure between phosphatidylcholine bilayers was measured by Simon *et al.* [54]. Their work determined that hydration pressure correlated with the dipole potential of the bilayer [54]. Despite all of this work, much more experimental data is needed to build a comprehensive explanation of the influence of monovalent ions on bilayers.

MD simulations provide a simple method to look thoroughly at lipid–ion interactions. Significant work with MD simulations includes that of Pandit *et al.* [55], Cordomi *et al.* [45, 56], and Gurtovenko *et al.* [57]. All simulations from these works show that cations bind in the head group region while the anion Cl^- loosely binds at just outside the head group. Pandit *et al.*found small decreases in the area per lipid, and increases in the carbon chain order parameter of Dipalmitoylphosphatidylcholine (DPPC), in the presence of NaCl [55]. Cordomi *et al.*and Gurtovenko *et al.*found that ions with smaller radii bind in higher numbers, and that the dipole formed by the locations of positive and negative ions was almost entirely counteracted by an increase to the dipole of the bilayer, such that the increase to the dipole potential of the lipid, due to the dipole from the ions, was minimal [45, 56, 57].

Force fields available for common lipids are well established and have shown repetitively to yield physically accurate results. In contrast, many simulations with ions result in issues, such as salt crystals forming below their solubility limit [58]. A comprehensive analysis by Cordomi *et al.* [56] simulated bilayers in ionic solutions, each with different force fields for the simulated ions. The result was significant differences in the structure of the bilayer such as area per lipid. New work by

Joung *et al.* [58] was released shortly after that of Cordomi *et al.*and was consequently unavailable. In this work of Joung *et al.*, new Lennard-Jones parameters where determined for monovalent ions, combined with common water models, by careful re-optimization against hydration free energy, lattice energy, and lattice constants [58]. These improvements to critical parameters for simulations where chosen for our simulations.

A thorough analysis of lipid bilayers in ionic solvents need long simulation times to reach equilibration [59]. This long run time is needed because equilibration of ionic binding is limited by the diffusion of ions in bulk water and the thermodynamic balance of association and dissociation process at the bilayer surface. For small ions, such as Li^+, these factors are especially burdensome since the lipid head group can accommodate a large number of ions, and their binding preferences tend to be deep in the bilayer. To ensure all runs reached an equilibrium state with the new force fields described above, each of our simulations were run for 0.5 μs.

3.2 Simulations

System Name	Composition	Run Length	Effective Bulk Concentration
POPC (No Salt)	200 POPC, 10,000 SPC/E	0.5 μs	–
POPC-LiCl	200 POPC, 29,784 SPC/E, 108 Li^+, 108 Cl+	0.5 μs	70 mM
POPC-NaCl	200 POPC, 29,784 SPC/E, 108 Na^+, 108 Cl+	0.5 μs	70 mM
POPC-KCl	200 POPC, 29,784 SPC/E, 108 K^+, 108 Cl+	0.5 μs	90 mM
POPC-RbCl	200 POPC, 29,784 SPC/E, 108 Rb^+, 108 Cl+	0.5 μs	120 mM

Table 3.1: Table of monovalent simulation details. Columns include the name of the system simulated and utilized throughout this chapter, the composition of molecules in the simulation, the simulated duration, and the effective bulk concentration, as determined by measuring the equilibrium ion concentration in the bulk water away from the bilayer.

Molecular Dynamics (MD) simulations of hydrated palmitoyl-oleoyl-phosphatidylcholine (POPC) bilayers were conducted. Five systems were simulated and their details listed in table 3.1. The first system was simulated without salt ions, referred to as POPC (No Salt). This system is used as a control to compare the other ionic simulations. It is comprised of two, 100 POPC lipid leaflets, arranged as a bilayer, and 50 molecules of waters per lipid. The remaining four simulations used the same initial lipid bilayer with a 150:1 water to lipid ratio. The increase in the ratio was necessary since the lipid bilayer adsorbs so many of the ions. Concentrations of ions, in simulations

with a 50:1 ratio, were fully absorbed by the bilayer; consequently, the bulk water region was left with a net negative anion density. Once the water molecules were established, 108 of them were replaced with Chloride (Cl^-), and 108 were replaced with the respective cation Lithium (Li^+), Sodium (Na^+), Potassium (K^+), and Rubidium (Rb^+), to achieve an initial ion concentration of 200 mM. Once in equilibrium, the effective bulk concentration was computed from the number of remaining ions in bulk water (table 3.1 column 4).

MD simulations were performed using version 4.5 of the GROMACS package [60–63]. Force fields published by Chiu *et al.* [24] were used for lipid molecules, while ions force fields were taken from Joung *et al.* [58]. Lipid and ionic cross term parameters were set explicitly from calculations using Lorentz-Berthelot rules [58]. Nosé-Hoover temperature coupling scheme was used to fix the simulated temperature at 300 K. Parrinello-Rahman semi-isotropic pressure coupling [21] was utilized to maintain a constant pressure of 1 atm. All bonds were constrained with the LINCS algorithm [40]. This restriction allowed for integration time steps of 4 fs. All dimensions of the simulation were set to periodic boundary conditions. Long range, above 10.0 Å, electrostatics were computed using SPME algorithm [41], and Van der Waals forces above 16 Å were cutoff.

All simulations were constructed by first generating two outwardly facing lipid leaflets, each with 100 lipids placed on a ten by ten grid. Then, the amount of SPC/E waters described in table 3.1 was added atop the bilayer. In the case of the ionic simulations, 108 water molecules were replaced by Cl^- anions and 108 water molecules were replaced by the appropriate cations. The systems were then energy-minimized to relax over stretched bonds and overlapping hard sphere surfaces. Proper thermalization of hydrocarbon chains was then achieved by annealing the system. Annealing steps included a 290 K run for 200 ps to allow the bilayer to relax. This was followed by a series of NVT simulations, which allowed for the system to further relax without exploding the box. These NVT ensembles were 50 ps at 500 to 420 K in 20 K steps, and 400 to 300 K in 10 K steps. This was followed with 50 ps NPT simulations from 400 to 300 K in 10 K steps. 500 ns of continuous MD simulations were carried out on each of the systems described in table 3.1 once fully annealed.

3.3 Analysis

3.3.1 Lipid Properties

Number Density

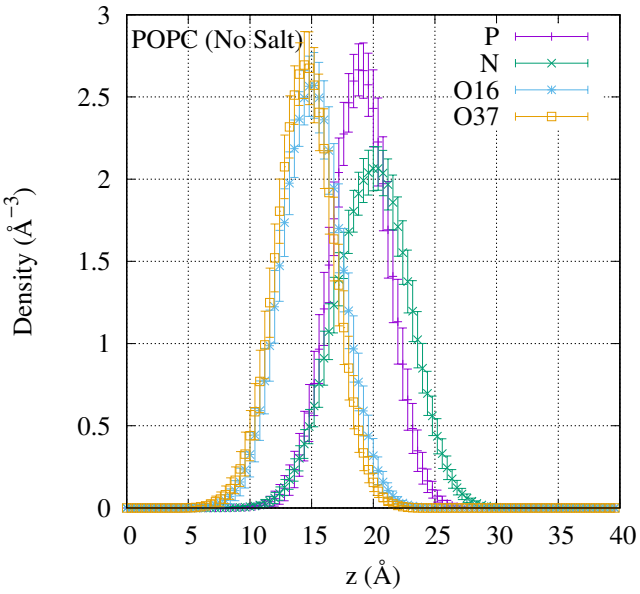

Figure 3.1: The number density of Phosphorus, P (purple), Nitrogen, N (green), Sn–2 side carbonyl oxygen, O16 (blue), and Sn–1 side carbonyl oxygen, O37 (orange), as a function of the distance to the center of the bilayer (z).

Ions, attracted to its partial charges, concentrate in the head group region of the bilayer. Figure 3.1 plots the number densities of pivotal head group atoms from the POPC (No Salt) simulation. We note in this figure, positively charged carbon atoms around the nitrogen (N) are in the outer most region of the head group, followed by the negatively charged regions surrounding the Phosphate (P) and carbonyl oxygen (O16 and O37). These densities are plotted for the four salt simulations in figure 3.2, with the addition of the cation and anion number densities. From this figure we see, as expected, the positive cations penetrate deep into the head group, between negatively charged phosphate and carbonyl groups, while the negative anions concentrate on the outer side of the positive nitrate region. We note that in particular, Li^+ has a left side protrusion, signifying a notable concentration of Li^+ in the carbonyl region. The number of cations in the head

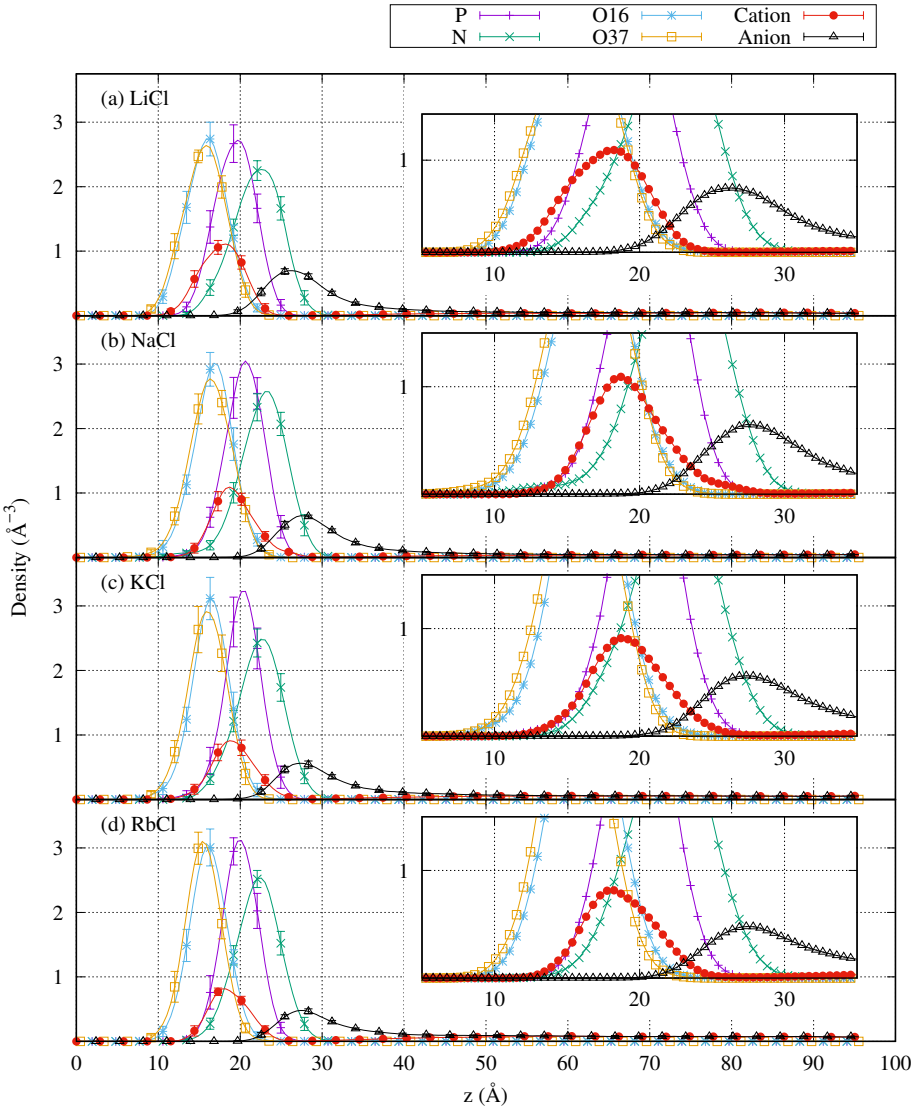

Figure 3.2: Number density plots for the four salt simulations, (a) POPC-LiCL, (b) POPC-NaCl, (b) POPC-KCl, and (c) POPC-RbCl. The six lines plot the densities of six important atoms in the simulation: Phosphorus, P (purple), Nitrogen, N (green), Sn–2 side carbonyl oxygen, O16 (blue), the cation used in the salt simulation (red), and the anion of Cl^- used in the salt simulation (black).

group region of the bilayer can be determined by integrating the number density times the area of the box. The number of cations, thus computed, are listed in the table 3.2 in the row labeled "No. of ions."

Volumes of the POPC bilayers in the five simulations were calculated from number densities according to section 1.4.1. V_c, V_{HG}, and V_l values, thus computed, are listed in table 3.2. These values for volume change very little with the introduction of ions which is expected since the addition of ions would not significantly affect the molecular volume of a lipid. The thickness of the bilayer, both $2D_c$ and D_b, were computed as described in section 1.4.1, and are listed in table 3.2. These values demonstrate thickening of the bilayer with the introduction of ions. Area per lipid (A_l) was then calculated from V_c and $2D_c$, and is printed in table 3.2. We note, the area per lipid decreases roughly as the concentration of ions in the head group region increases. The decreased A_l has been established with other simulations [45, 51, 55, 64]. In those simulations, force fields for K^+ would not allow it to disassociate with Cl^- in any significant amount, and so it would not enter the bilayer and thereby have little effect on the bilayer properties.

Properties	POPC (No Salt)	POPC-LiCl	POPC-NaCl	POPC-KCl	POPC-RbCl
No. of ions	–	78.63	78.25	68.53	58.21
V_c (Å^3)	902.9	895.0	895.1	895.1	897.0
V_{HG} (Å^3)	313.5	312.0	310.7	316.4	315.3
V_l (Å^3)	1216.4	1202.0	1200.1	1207.2	1211.1
$2D_c$ (Å)	27.4	29.9	30.1	30.3	29.9
D_b (Å)	35.80	39.75	40.96	40.16	39.07
A_l (Å^2)	65.9	59.9	57.7	59.0	60.0
D_{HH} (Å)	37.01	38.07	40.32	40.19	38.94
P-N angle (°)	14.45	36.33	31.36	29.46	29.63

Table 3.2: Table of bilayer properties for the POPC (No Salt) and four monovalent simulations.Row "No. of ions" is the number of cations in the head group region as determined from integrating the number density. V_c, V_{HG}, and V_l are the volumes of the carbon chains, head group region, and total lipid respectively. $2D_c$ and D_b are the thicknesses of the both leaflets of carbon chains and of the total bilayer. A_l is the area per lipid. D_{HH} is the peak to peak difference in electron density. "P-N angle" is the average angle of the P-N vector with respect to the bilayer normal.

Chain Order Parameters

As ions enter the head group, the area per lipid decreases. This decrease in the area requires hydrocarbon chains to order, thus thickening the bilayer as measured above. If the bilayer is

thickening, the order parameter of the carbon chains must also increase [55]. Carbon chain order parameters were calculated as explained in section 1.4.1 and plotted in figure 3.3 1 for Sn–1 side carbons and figure 3.3 2 for Sn–2 side carbons.

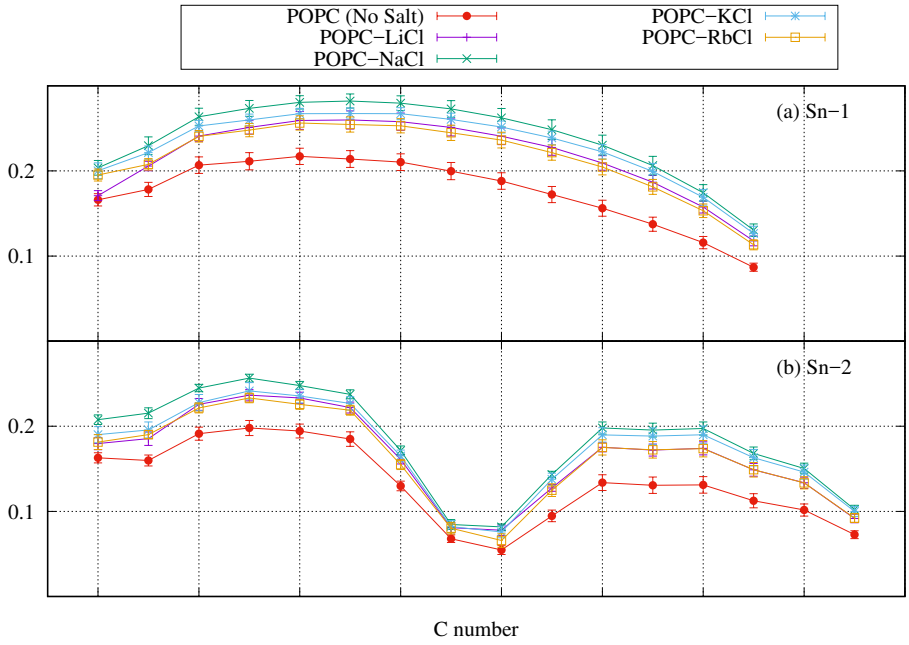

Figure 3.3: Carbon chain order parameters. (a) Sn–1 side order parameters. (b) Sn–2 side order parameter. Order parameters of each simulation are presented in a different color, POPC (No Salt) in red, POPC-LiCl in purple, POPC-NaCl in green, POPC-KCl in blue, POPC-RbCl in orange.

We can see in figure 3.3 carbon chain order increases for all carbons, other than the first carbon, of the Sn–1 side, of the POPC-LiCl simulation. Further, this increase appears proportional to the decrease in thickness.

P-N Angle

Head group orientation is believed to act as a charge sensor for the bilayer surface [46, 47] ergo, the angle of the head group dipole is particularly interesting in ionic simulations. The angle of the head group, as measured by the angle between the vector connecting the P and N atoms and the vector normal to the bilayer was calculated according to section 1.4.1. The average P-N angle, calculated thusly, is listed in table 3.2. We note, indeed the P-N able does increase with the presence of ions. However, it also appears that the species of ions might affect the angle more than

the concentration since lower concentrations of Rb^+ and K^+ produce angles within two degrees of Na^+ while Li^+ is more than five degrees strait than Na^+.

3.3.2 Solvent Properties

Cations, being positively charged, associate with negatively charged atoms, which in these simulations are oxygen. These oxygen atoms are available in water oxygen and lipid oxygen such as phosphate and carbonyl. The association of these atoms can best be seen in radial distribution function (RDF), the pairwise correlation function, between cations and each oxygen atom. The first peak in the RDF represents the increased probability at finding oxygen inside some shell about the ion. This high probability density zone and the oxygen atoms inside of it are referred to the solvation shell. For the following measurements, we take the location of the first trough after the first peak in the RDF as the solvation shell cutoff. Any oxygen atoms inside this cutoff will be considered "bound" to the cation.

Reaction Rate

In our simulations, ions did not start with an excess concentration in the head group but are randomly distributed throughout the solvent. Ions, diffuse through the solvent and can bind to the bilayer. For cations, we consider them bound to the bilayer when it haves at lease one lipid oxygen in the solvation shell. Once the system has reached equilibrium, the reaction must be steady state, that is the rate at which the ions bind to the bilayer must be the same as the rate at which they unbind. To ensure a steady state was reached, the number of cations bound to the bilayer (n) is plotted vs. time t in figure 3.4. Assuming the reaction is first order, the on-rate (K_{on}) and off-rate (K_{off}) constants are determined by fitting the equation

$$n(t) = \frac{NK_{on}}{K_{on} + K_{off}}(1 - e^{-(K_{on}+K_{off})t}) + n_0 e^{-(K_{on}+K_{off})t}, \tag{3.1}$$

where N is the 108 total cations and n_0 is the initial number of cations at the epoch point where $t = 0$. The values determined by a Gnuplot fit, for each salt simulation, are printed, along with the equation, on figure 3.4. We note, in the figures, the apparent leveling off of the data denotes the simulations have reached sufficient steady state.

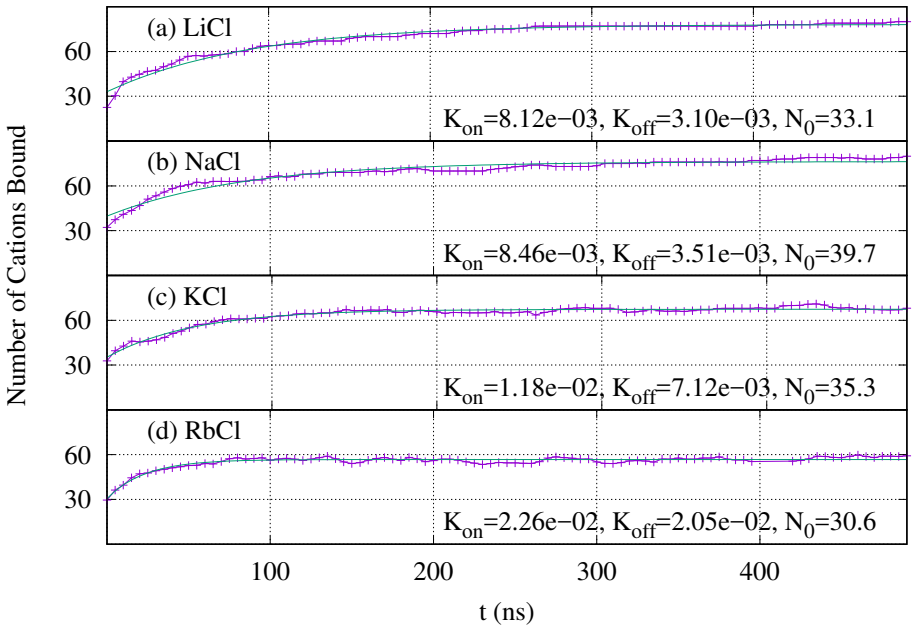

Figure 3.4: Plots of the number of cations bound to the lipid as a function of time for (a) POPC-LiCl, (b) POPC-NaCl, (c) POPC-KCl, and (d) POPC-RbCl simulations. An exponential function is fit to each plot to extrapolate the printed reaction parameters.

Coordination Number

Since we can track the number of ions of each type, surrounding each cation, it is of interest to determine the coordination number. The coordination is the number of oxygen atoms inside the solvation shell, and the population of each species of oxygen inside the solvation shell. Coordination is used to understand how the ions fill their shell differently inside the lipid head group as opposed to in bulk water. Figure 3.5 plots, for each cation, the average number of each oxygen species in the solvation shell, and the total number of oxygen atoms, of the cation simulated as a function of its distance from the center of the bilayer. Cations in bulk water fill their shell with water oxygen. The coordination numbers of Li^+, Na^+, K^+, and Rb^+ in bulk water are ~ 4, ~ 6, ~ 7, and ~ 8 respectively. These values are consistent with other simulations and experiments [45, 65]. We note that the total coordination drops as cations approach the center of the bilayer and that Na^+ and Rb^+, in particular, lose almost an entire bond oxygen. This loss is possibly due to cations not able to find energetically favorable configurations within the rigged lipids.

In addition to a small drop in total coordination number as cations approach the center of the

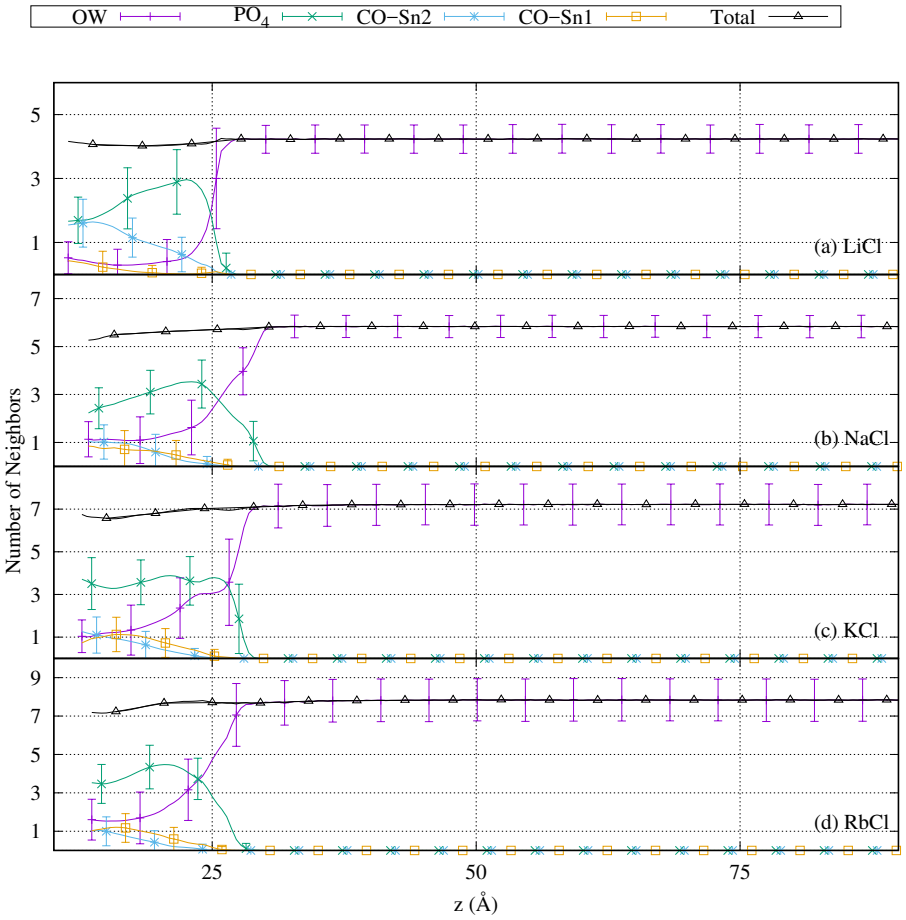

Figure 3.5: The number of each type of oxygen atom, and the total number of oxygen atoms, in the solvation shell of the simulated cation in each of the salt simulations: (a) POPC-LiCl, (b) POPC-NaCl, (c) POPC-KCl, (d) POPC-RbCl. Oxygen types include water oxygen, OW (purple), phosphate oxygen (green), Sn–2 side carbonyl, CO-Sn2 (blue), Sn–1 side carbonyl, CO–Sn1 (orange), and the total number of oxygen (black).

bilayer, there is a loss in the number of water oxygen completing the solvation shell. In particular, Li^+ looses almost all water, having less than one water oxygen in the shell on average. We note, for all cations, except Li^+, coordination numbers of carbonyl oxygen increase consistently for both the Sn–2 side (depicted in blue), and the Sn–1 side (depicted in orange). In the case of Li^+, it heavily favors the Sn–2 side carbonyl as a binding site.

Water Order

The perturbation of water is an essential measurement in connection to the stability and structure of the bilayer. In ^{2}H-NMR water experiments, the quadrupole splitting of water is measured to infer perturbation of water at that bilayer surface. These experiments are not available for ionic solvents due to difficulty controlling the ion concentration with such small amounts of water. However, with simulations, we are able to directly measure the perturbation of water in each slice of the bilayer and understand changes to the ordering of water in the presence of each cation. The average first and second rank water orders were calculated as explained in section 1.4.2. The results of these calculations are plotted in figure 3.6 a for rank 1, and figure 3.6 b for rank 2, as a function of distance from the center of the bilayer. We note that water concentration decreases as a hyperbolic function as we approach the center of the bilayer and consequently, the total water order is less in that region. We note the critical difference in the first rank order of salt simulations, seen in figure 3.6 a, is that in addition to the negative order, there is a positive first rank order region, extending past the negative one, corresponding to the $O \rightarrow H$ pointing away from the bilayer. In figure 3.6 b, we note that salt simulations have an additional negative region outside the inner negative and positive regions corresponding to the $O \rightarrow H$ becoming more parallel.

Inside the head group, cations are chaotropic agents. In figure 3.6 cations lower the average the order of water, in both ranks. Li^+ appears to be the most chaotropic, lowering the order in each rank, in the $\sim$15Å range by more than the error bars of the next chaotropic cation. The ability of Li^+ to destabilize water is possibly related to the toxicity since the reduction of water order will weaken the bilayer.

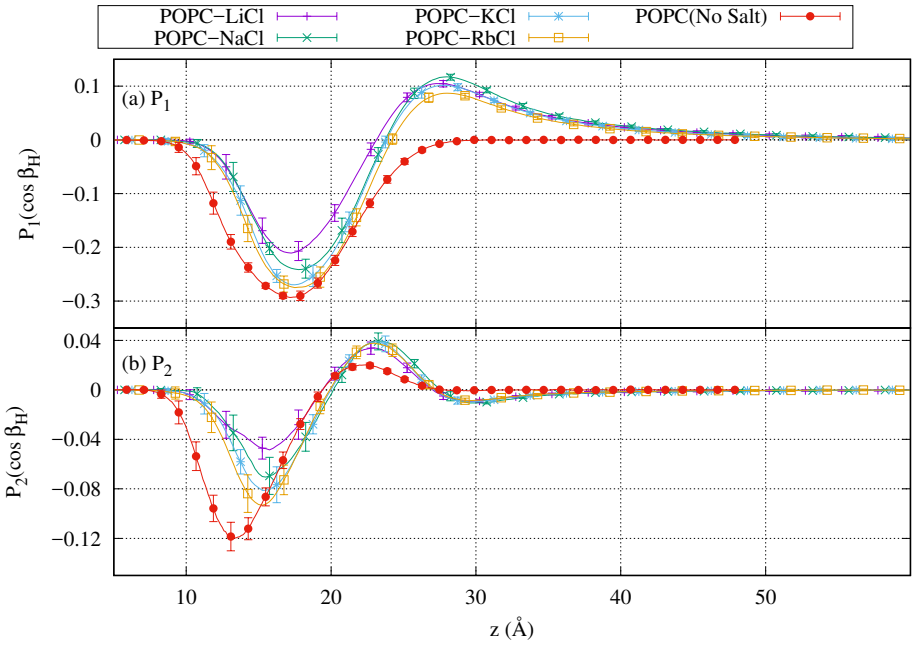

Figure 3.6: (a) First rank and (b) second rank order parameters for the five simulations as a function of distance from the center of the bilayer (z). Plots are colored by simulation, POPC (No Salt) in red, POPC-LiCl in purple, POPC-NaCl in green, POPC-KCl in blue, POPC-RbCl in orange.

3.3.3 Interface Properties

Electric Potential

Large concentrations of ions settling on two separate surfaces, cations between phosphate and carbonyl groups and anions around the nitrate groups, creates a large dipole, which one would expect to increase the dipole potential of the bilayer significantly. Figure 3.7 is a plot of the electric potential computed, as described in section 1.4.3, as a function of the distance from the center of the bilayer. The electric potential of bulk water was taken to be zero. We see in these figures that the dipole potential of bilayers simulated with ions has increased, but not to the extent expected from the large charges concentrated in the head group. The reason for this is explained in work by Cordomi *et al.* [45], which showed that the changes to the dipole potential, due to the straightening of the head group and its dipole, reduces the increase in potential due to the presence of salt [45]. This increase is therefore consistent with dipoles in other simulations [45].

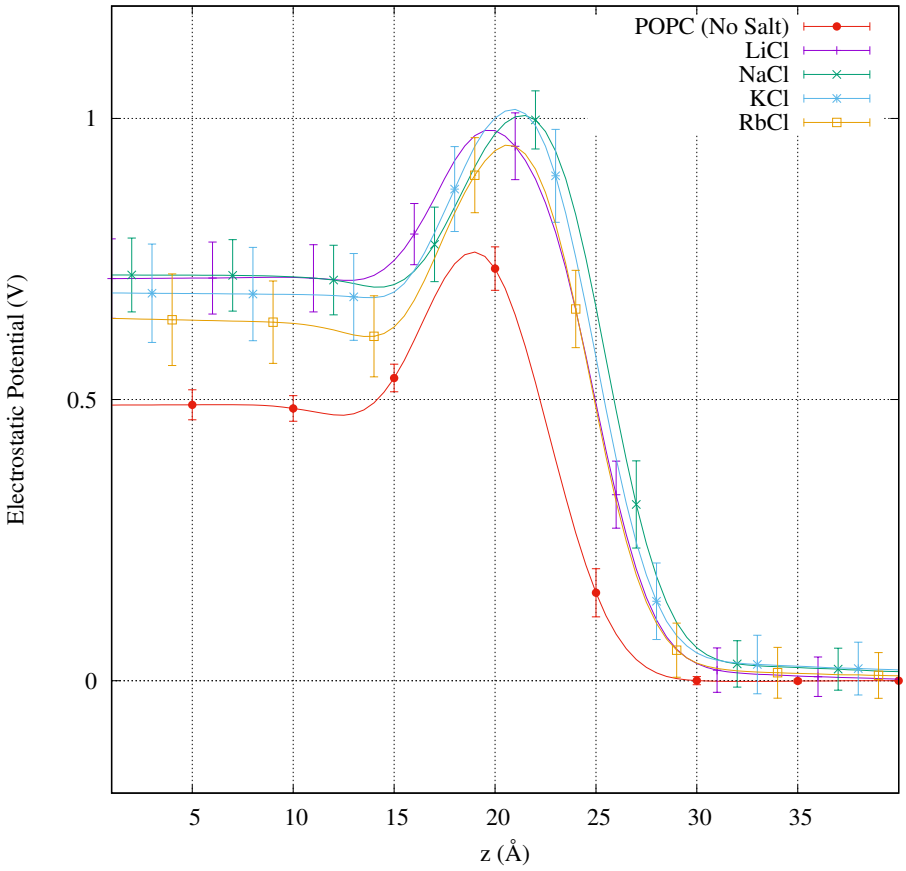

Figure 3.7: Electrostatic potential as a function of distance from the center of the bilayer. The potential of bulk water was taken to be zero. Each simulation is plotted in a different color, POPC (No Salt) in red, POPC-LiCl in purple, POPC-NaCl in green, POPC-KCl in blue, POPC-RbCl in orange.

Pressure Profile

Lipid bilayers, absent of osmotic pressure, free to contract and undulate, have no surface tension [66]. NPT simulations with semi-isotropic pressure coupling adjust their dimensions until they have no net surface tension. However, the surface tension on a particular slice of the simulation can be non-zero, and give insights into the mechanical stresses acting on different regions of the bilayer [27, 29, 30, 67]. In order to explore the changes to the stress of a bilayer in the presence of different cations, we computed the pressure profiles as described in section 1.4.3. Simulation boxes were divided into 150 slices. Local pressure tensors in each slice were computed every 0.5 ps and averaged over 250 ps runs. The set of tensors for each interaction was then summed to find the total pressure tensor of the run. This process was repeated for 40, 250 ps runs, each 5 ns apart for the last 200 ns of each of the 5 simulations.

Figure 3.8 is a plot of the normal pressure component minus the average of the lateral components of the pressure profile. These differences are the surface tension contributions, the integration of which are the surface tensions of the simulated systems. Since the pressure components normal to the slices, in a semi-isotropic NPT simulation, should all equal to the set pressure in the normal dimension, changes in the surface tension contributions can be said to come from opposite changes in lateral pressure. In general, all the plots of surface tension contribution in figure 3.8 start with an initial excess lateral pressure in the hydrocarbon chain region (0 to 12 Å). This positive lateral pressure is slightly relieved around the region of the double bonded carbon ($\sim$ 8 Å) in the oleoyl chain. In the head group region of the bilayer, for all simulations, there is a negative lateral pressure, and a positive region, with a peak of $\sim$ 600 bars. By $\sim$ 20 Å from the center of the bilayer, around the region of the positive rank two water order described in section 3.3.2, the lateral pressure again becomes negative.

At $\sim$ 27 Å from away from the center of the bilayer, there is a significant difference in the form of the lateral pressure of POPC (No Salt) and the other Salt simulations. In this region, the lateral pressure of POPC (No Salt) decays exponentially until it reaches the normal pressure (indicated by $P_N - P_L$ going to zero). The lateral pressure of the salt simulations reverses, giving an additional negative lateral pressure. This negative lateral pressure is in the same region, and is a similar shape, as the outer negative second rank water order. This final region decays exponentially from

the opposite sign as POPC (No Salt).

We note that in the first region of positive lateral pressure, the portion between the double bonded carbon and the negative peak ($\sim$ 8 to 12 Å) increases in lateral pressure in simulations with salt. In particular, the lateral pressure in POPC-LiCl is $\sim$ 50 bars greater than the next closest simulation, that of POPC-NaCl. Cantor *et al.* [67] has been shown that changes in lateral pressure can be a mechanism for regulating protein functions [67] and therefore, the mechanism of the pharmacological effects of Li^+.

We note that the lateral pressure in bulk water is equal to the normal pressure, since water, away from the influence of the bilayer, is isotropic. We, therefore, define a new barrier between the bulk solvent and non-bulk solvent, where the solvent is under stress from the bilayer. We refer to this boundary as the "*hydrostatic boundary*" and define it using $P_N - P_L$ with the following procedure. First, we truncate the portion of the final curve which demonstrates monotonic decay to zero. Next, we use the Marquardt-Levenberg algorithm to fit the data to the exponential function,

$$f(x) = -ae^{-b(x-c)}, \tag{3.2}$$

where a, b, and c are fitting parameters, whose initial values are $a = 400$, $b = 0.2$, and $c = 25$ for POPC (No Salt), and $a = -200$, $b = 0.2$, and $c = 25$ for the four salt simulations. Once the fitting parameters are determined, the length scale of the exponent, $\frac{1}{b} + c$, is taken to be the "*hydrostatic boundary*." The values, thus computed, are printed in red in figure 3.8 next to each plot.

Surface Charge

ζ-potential is a critical measurement in electrophoretic mobility experiments [68, 69] and is related to the surface charge densities ($\sigma(z)$) as mentioned in section 1.2.4. $\sigma(z)$ can be calculated from the equation

$$\sigma(z) = \int_0^z \rho(z')dz', \tag{3.3}$$

where z' is the distance from the center of the bilayer which is integrated over, $\rho(z')$ is the charge density at z', and z is the distance of the "slip surface" from the center of the bilayer. We assert the

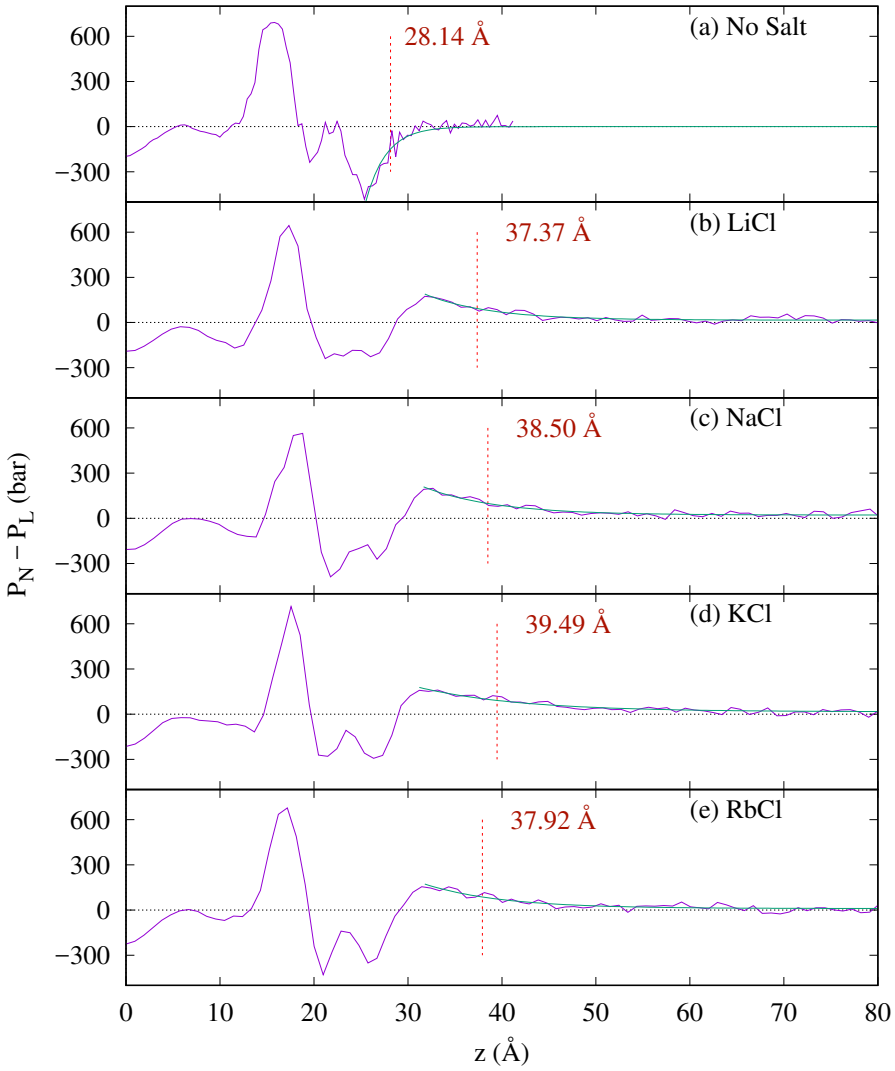

Figure 3.8: Plots of the difference between the normal component and average of the lateral components as a function of the distance from the center bilayer (purple). The integration of this function is the total surface tension of the simulation. An exponent is fit to the final decay (blue) of the plot, and the pivot of the exponent is denoted in red.

previously mentioned *"hydrostatic boundary"* is equivalent to the "slip surface" in Electrophoretic Mobility experiments. For all POPC simulations, $\sigma(z)$ integrated to this boundary was zero. This suggests that the presence of ions does not significantly alter the surface potential of the zwitterionic lipid. This result is consistent with electrophoretic mobility experiments by McLaughlin *et al.* [70].

3.4 Conclusions

Five POPC lipid bilayers were simulated, one control bilayer without the addition of salt ions, four each with a monovalent cation (Li^+, Na^+, K^+, or Rb^+) and the anion Cl^-. Two crucial techniques were established when simulating bilayers with ions. First, a sufficiently large solvation layer is needed such that cations absorbed by the lipid bilayer do not leave the bulk region unbalanced by anions. Second, sufficient time must be allowed for ions to reach a steady state with the surface of the bilayer.

Force fields by Joung *et al.* [58] are shown to yield better results than previous ionic simulations. In particular, larger ions, such as K^+, were now able to penetrate the bilayer, believed to be a defect of previous ion force fields [56].

Cations appear to have unique binding affinities inside the bilayer. Li^+, in particular, has a strong affinity to the Sn–2 side carbonyl, possibly due to the small ionic radius.

The Structure of the bilayer is altered by the binding of ions in the head group. Roughly proportional to the number of ions bond to the bilayer, the order of the hydrocarbon chain increased, the area per lipid A_l decreased, and the thickness $2D_c$ and D_b increased. Another physical change is the straightening of the head group as seen in the increase of the $P \rightarrow N$ angle with respect to the bilayer plane.

Ions have a chaotropic effect on the water order in the head group region, lowering the overall order of water. Li^+, in particular, has the greatest chaotropic effect in the deepest region of the head group. Plots of water order outside the head group of the lipid, have an additional ordered region far outside of POPC (No Salt).

The dipole potential increases with the presence of all ions. This increase is small compared to the amount of additional charge inside the bilayer. The reduction is believed to be due to an increase in the oppositely directed $P \rightarrow N$ dipole.

Pressure profiles for the five simulations show similar shapes for lateral pressure across the membrane. Some differences include an increase in lateral pressure in the hydrocarbon tail region above the double bonded carbon. This increase in lateral pressure could be a mechanism for regulating protein functions around ions. Another change in the pressure profile has an additional negative lateral pressure region outside the bilayer in the same region as the additional rank two positive water order seen in ionic simulations. The length scale of the exponent is taken as the *"hydrostatic boundary"* used to compute the surface charge of the simulations, which is effectively zero.

Chapter 4

Lipid Bilayers in the Presence of Divalent Ions

4.1 Introduction

In addition to monovalent ions, divalent ions also play essential roles in human biology. Mg^{2+} and Ca^{2+} are both critical elements in bone and muscle development [71]. In recent works, it is theorized that the pharmaceutical effects of Li^{+} may arise from its ability to replace Mg^{2+} in critical physiological processes [72]. In particular, Li^{+} is thought to be an inhibitor for Mg^{2+} in Glycogen Synthase Kinase 3-beta (GSK-3β) [73]. Of the two binding locations of Mg^{2+} on GSK-3β, Li^{+} has been shown to replace Mg^{2+} at one of these sights. Recent work by Srinivasan *et al.* [74] has shown strong competition between Li^{+} and Mg^{2+} in the interior membrane of red blood cells. This competition is unexpected since the solvation shell, a significant contributor to ion competition, of Li^{+} is measured several atoms small in coordination number then Mg^{2+}.

In chapter 3, we used the new force fields optimized against hydration free energy, lattice energy, and lattice constants by Joung *et al.* [58] to simulate bilayers with ions using these new parameters. Improved force field parameters for divalent ions are more difficult as less experimental data exists to compare to; however, we found two recent papers published improved parameters for divalent ion parameters using similar optimizations to Joung *et al.* [58]. The first such paper is by Li *et al.* [75], where experimental hydration free energies and ion-oxygen distances were used to tune parameters for Mg^{2+} and Ca^{2+}. Additional Mg^{2+} force fields were published by Aqvist *et al.* [76] using the exchange rate of the first shell water molecules [76]. Despite the force fields from these two works being similar, work by Bergonzo *et al.* [77] showed different inner shell water molecule loss to form chelated interaction with the RNA [77]. Hence, in this chapter, we used two simulate both Mg^{2+} force fields and where appropriate, compare results from the two sources.

If Li^{+} is a suitable replacement for Mg^{2+}, we expect the solvation shell of Li^{+} is in some way similar to that of Mg^{2+}. Solvation shells are the nearest neighbors attracted to the ions arranged

in a lower energy arrangement. To compare the solvation shells of cations, we introduce a novel method of classifying solvation arrangements, by mapping them to a completely connected graph whose edges are weighted by the length between the atoms that make up the vertices. With this mapping, comparisons can be made by looking at the percent of sub-graph isomorphism between the species.

4.2 Simulations

Three 500 ns MD simulations were performed on three new systems. Each of the three systems were simulated with POPC lipid bilayers, just as in chapter 3. In addition to the lipids, the simulation had 150:1 SPC/E waters per lipid. In two of the simulations, 108 random water molecules were replaced by Mg^{2+} while in the last simulation they were replaced with Ca^{2+}. In all three simulations, 216 water molecules were replaced with Cl^{-}. The systems were constructed in the same faction as chapter 3, were two leaflets of lipids are constructed with 100 lipids each and a water layer is built on top, and then finally the number of water molecules mentioned above were replaced with the appropriate number of cations and anions to achieve the 200 mM initial concentration.

Version 4.5 of the GROMACS software package [60] was used to evolve the system. One atm pressure was maintained using the Parrinello-Rahman semi-isotropic pressure coupling [21], and the temperature was held at 300 K using the Nosé-Hoover temperature coupling scheme [20]. Pairwise bonds were constrained using the LINCS algorithm [40]. With this constraint, an integration time step of 4 fs is possible and was used for all of the simulations unless otherwise noted. Long-range electrostatics with beyond the real-space cutoff of 10.0 Å were calculated using the SPME algorithm [41], and Lennard-Jones potentials were truncated after 16 Å.

Force fields parameters for lipids were taken from Chiu *et al.* [24], while force fields from divalent ions were taken from Li *et al.* [75] or Allner *et al.* [76]. In the case of simulations where force fields of Li *et al.*are used, a superscript with the Roman numeral I will be added to the name, and for simulations where force fields of Allner *et al.*are used, a superscript of the roman numeral II will be added. The cross terms between the new force fields and the lipid force fields were calculated using Lorentz-Berthelot [58].

4.3 Analysis

4.3.1 Lipid Properties

Number Density

Number densities of the three simulations were calculated and are presented in figure 4.1. We note in these results that concentrations of divalent cations are much smaller than ion concentration in figure 3.2. The number of cations in the first peak in density seen in figure 4.1 is calculated by integrating the cation number density from the center of the bilayer to the minimum following the first peak. The number of cations, thus computed are listed in the row "No. of ions" of the table 4.1. Since divalent cations have a net charge of +2, a better metric, when comparing the effects of lipid properties due to ion concentration, is the charge concentration in the head group from cations; therefore, the number of ions is multiplied by 2 and listed in table 4.1 as the row Charge. These values for Mg^{2+} are smaller than the charge present in the monovalent simulations, but the additional charge from Ca^{2+} is in the range of Na^{+} and Li^{+} from the last chapter.

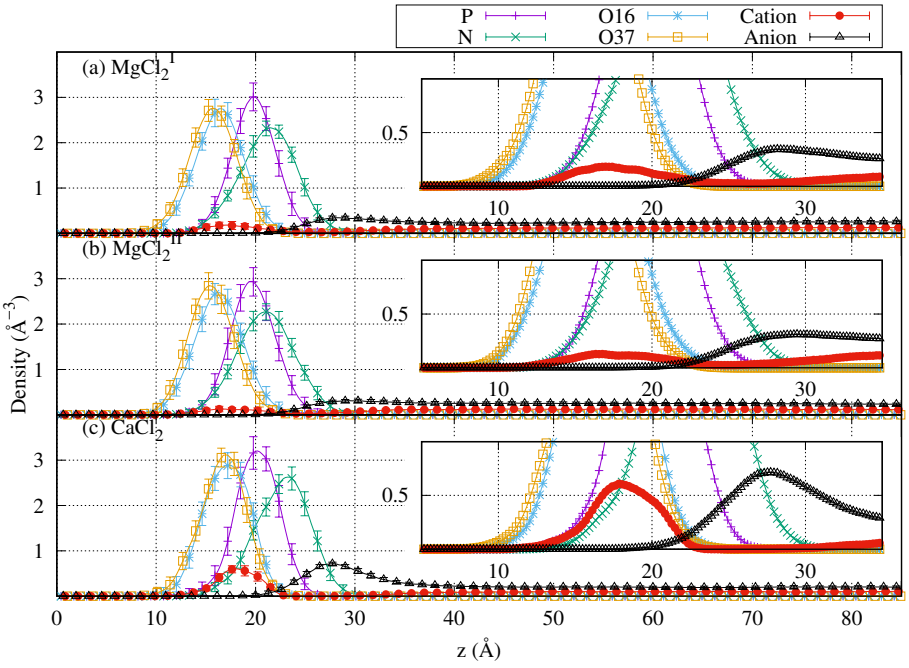

Figure 4.1: Number density plots for the three divalent salt simulations (a) $MgCl_2^I$ (b) $MgCl_2^{II}$, and (c) $CaCl_2$. The six lines plot the densities of six important atoms in the simulation: Phosphorus, P (purple), Nitrogen, N (green), Sn–2 side carbonyl oxygen, O16 (blue), the cation used in the salt simulation (red), and the anion of Cl^{-} used in the salt simulation (black).

Volumes of the three simulations were computed according to section 1.4.1. V_c, V_{HG}, and V_l values, thus computed, are listed in table 4.1. Again, these values change very little in the divalent ion simulations since molecular volume does not change significantly based on simulation parameters. Bilayer thickness, $2D_c$ and D_b, was computed from number density according to the process described in section 1.4.1. The values, thus computed, are listed in table 4.1. The thickness of the hydrocarbon chains ($2D_c$) and volume of the chains (V_c) are used to compute the area per lipid $A_l = 2V_c/2D_c$. Changes to A_l due to the presence of ions, as reported in tables 4.1 and 3.2, appear to decrease in A_l from that of POPC (No Salt) proportional to the charge from the cation, in the head group of the bilayer. To confirm this hypothesis, we plot the A_l vs. the additional charge in the head group region from the addition of cations in figure 4.2. We also fit a linear function to the points in the figure. The slope of this line is -19.55 $\AA$ per e, meaning we expect in the range of concentrations we are studying, the area per lipid of the bilayer decreases 19.55 $\AA$ for every additional elementary charge per lipid, in the head group of the bilayer.

Electron Density

Electron density for the three simulations was calculated and plotted in figure 4.3. The peak to peak electron density distance, D_{HH}, was calculated for these plots and placed in table 4.1. Form factors were derived from these electron densities by taking the cosine transform as described in section 1.4.1. These transforms are plotted in figure 4.4. We have not at this time, identified x-ray scattering experimental data for divalent ions to compare these form factors too, but the data is available for this comparison.

P-N Angle

The orientation of the head group region of the lipid head group was computed as described in section 1.4.1 using the angle between the vector connecting the phosphorus and nitrogen atoms, and the vector normal to the bilayer. The average angle was taken as the mean angle for the last 100 ns of the simulations. The resulting angles are listed in table 4.1. We note that the increase in P-N angle for Ca^{2+} is consistent with the other monovalent ions, but the decrease in angle for $MgCl_2^I$ and $MgCl_2^{II}$ is unique. This decrease in angle suggests that the charge signaling the head group is responsible for [46, 47] might be dependent on the species of cation present.

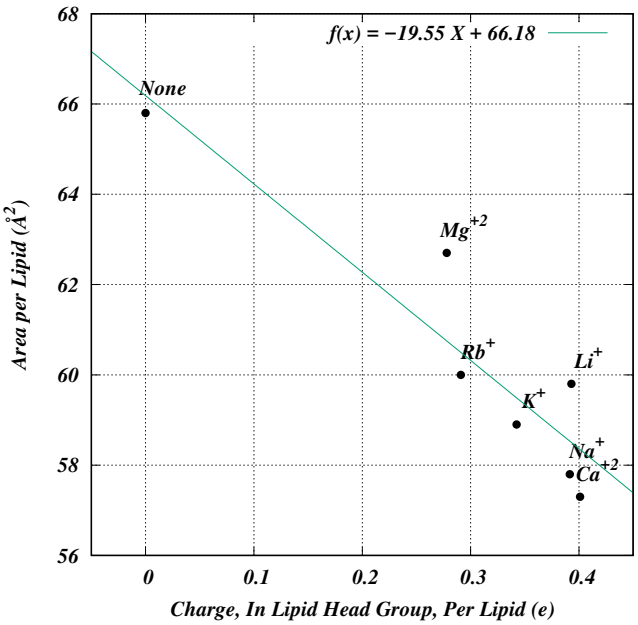

Figure 4.2: A plot of the A_l vs. additional charge in the lipid head group from the presence of cations. Data points are taken from the Mg^{2+} and Ca^{2+} simulations in this chapter, and the five other POPC simulations from the previous chapter. A linear function is fit to the data points with a slope of -19.55 $\mathring{A}$ per e. $MgCl_2^{II}$ is omitted since is it not significantly different from $MgCl_2^{I}$.

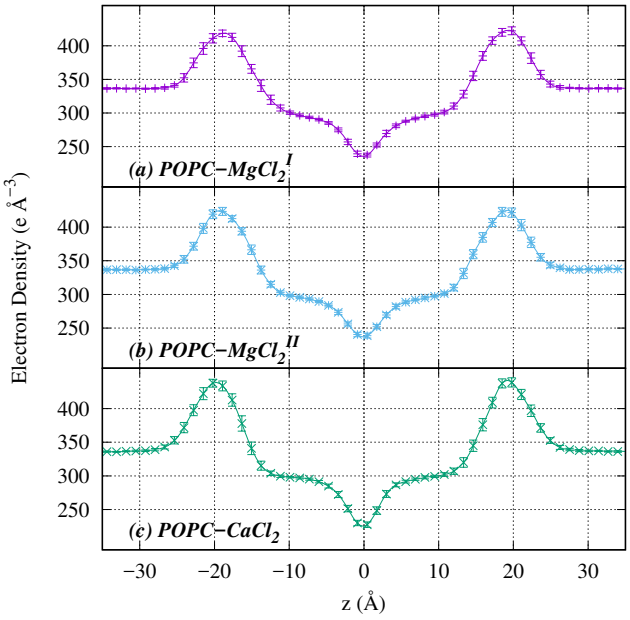

Figure 4.3: The electron density of divalent ion simulations as a function of the distance from the center of the bilayer (z). (a) POPC-$MgCl_2^I$, (b) POPC-$MgCl_2^{II}$, (c) POPC-$CaCl_2$.

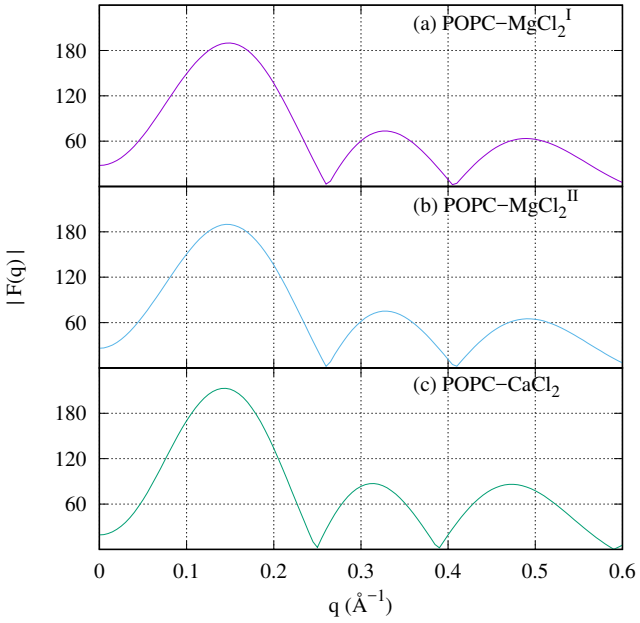

Figure 4.4: Form factor plots of divalent simulations. (a) POPC-$MgCl_2^I$, (b) POPC-$MgCl_2^{II}$, (c) POPC-$CaCl_2$.

Properties	POPC (No Salt)	POPC-$MgCl_2^I$	POPC-$CaCl_2$	POPC-$MgCl_2^{II}$
No. of ions	–	15.6	35.0	16.6
Charge	–	31.2	70.0	33.2
V_c (Å^3)	902.9	899.6	891.8	899.5
V_{HG} (Å^3)	313.5	314	312	313.4
V_l (Å^3)	1216.4	1214.5	1204.0	1212.9
$2D_c$ (Å)	27.4	28.7	31.1	29.5
D_b (Å)	35.80	37.8	41.6	37.6
A_l (Å^2)	65.9	62.6	57.4	62.9
D_{HH} (Å)	37.01	38.2	39.0	38.1
P-N angle (°)	14.45	9.60	21.93	12.1

Table 4.1: Table of bilayer properties for the POPC (No Salt) and three divalent simulations.Row "No. of ions" is the number of cations in the head group region as determined from integrating the number density. Charge is the number of cations in the head group region times the charge of those ions. V_c, V_{HG}, and V_l are the volumes of the carbon chains, head group region, and total lipid respectively. $2D_c$ and D_b are the thicknesses of both leaflets of carbon chains and of the total bilayer. A_l is the area per lipid. D_{HH} is the peak to peak difference in electron density. "P-N angle" is the average angle of the P-N vector with respect to the bilayer normal.

Chain Order Parameters

Changes to the order of the hydrocarbon chains were calculated according to section 1.4.1 and were plotted in figure 4.5. We note, as seen with monovalent ions that the addition of ions causes a decrease in area per lipid, which increases the thickness of the bilayer, which corresponds to an increase in hydrocarbon chain order. This set of properties has been stated previously [45, 51, 55, 64], and our work with newer force fields is consistent with this.

4.3.2 Interface Properties

Electrostatic Properties

The electrostatic potential of each of the three divalent salt simulations was calculated following our procedure outlined in section 1.4.3. These potentials, thus computed, are plotted with the electrostatic potential of POPC (No Salt), appear in figure 4.6. Changes to the dipole potential due to divalent ions are consistent with monovalent ions, to the extent that the amount of charge inside the head group is proportional to the shift in potential.

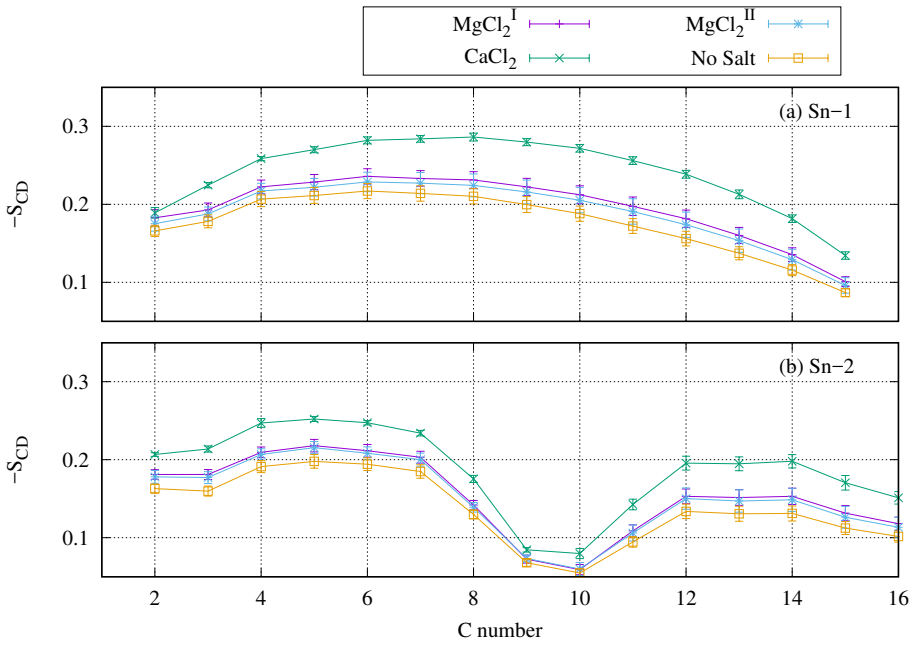

Figure 4.5: Carbon chain order parameters. (a) Sn–1 side order parameters. (b) Sn–2 side order parameter. Order parameters of each simulation are presented in a different color, $MgCl_2^I$ in purple, $MgCl_2^{II}$ in blue, $CaCl_2$ in green, and POPC (No Salt), taken from chapter 3 in orange.

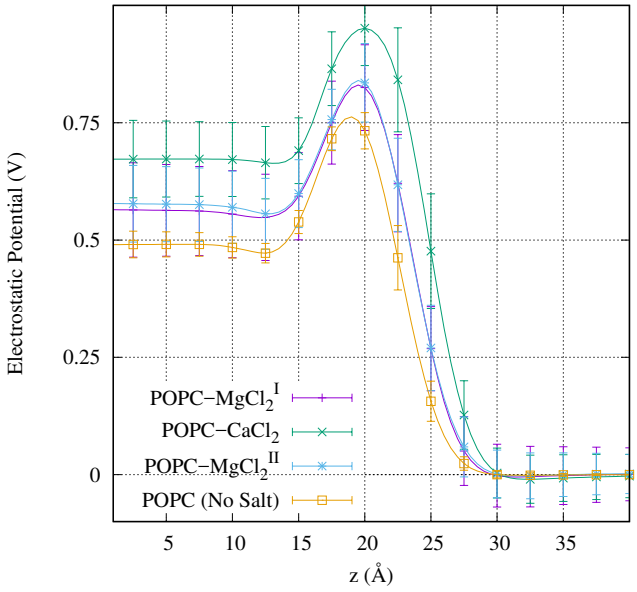

Figure 4.6: Electrostatic potential of the simulation as a function of the distance from the center of the bilayer. Potentials of each simulation are presented in a different color: $MgCl_2^I$ in purple, $MgCl_2^{II}$ in blue, $CaCl_2$ in green, and POPC (No Salt), taken from chapter 3 in orange.

4.3.3 Solvent Properties

Water Order

Structure and stability of the bilayer are tied to the structure of water surrounding it. Water inside the head group is studied with NMR experiments which measure the order of the water molecules by measuring changes to the quadrupole splitting of the bilayer. In simulations, we have full access to the orientation of water throughout the bilayer. With this in mind, we measured the rank one and rank two according to the procedure described in section 1.4.2, and plotted the results in figure 4.7a for rank one order, and in figure 4.7b for second rank order. We can see in these figures that Ca^{2+} has a stronger chaotropic property towards the center of the bilayer but has much higher order in the regions just outside the head group. Both Mg^{2+} and Ca^{2+} have the additional positive rank one and negative rank two regions outside the head group region as seen in monovalent solvent simulations from the last chapter.

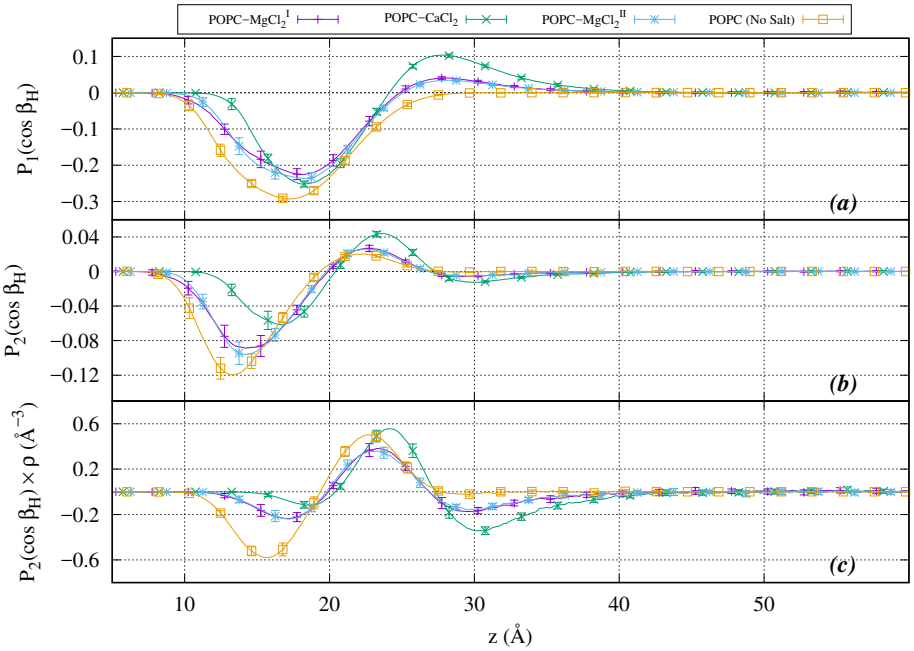

Figure 4.7: (a) First rank and (b) second rank order parameters as a function of distance from the center of the bilayer (z). (c) The product of the second rank order parameter and the density of water oxygen used for the estimation of $\Delta\nu$. Each figure includes plots for POPC (No Salt) in orange, POPC-$MgCl_2^I$ in purple, POPC-$CaCl_2$ in green, and POPC-$MgCl_2^{II}$ in blue.

It has been shown that experimental values of $\Delta\nu$ from Nuclear Magnetic Resonance (NMR)

Spectroscopy can be reproduced using the product of the second rank water order ($S(B_z)$) and water density (P_z) [26, 78], the result of which can be seen in figure 4.7c. This plot is proportional to the quadrupole splitting which arises from the water ordering in each slice. To compute the expected $\Delta\nu$ from this plot, we used the equation

$$\Delta\nu = \frac{3}{4}\chi\frac{1}{P_t}\sum_{z=0}^{z_0} P_z S(B_z), \tag{4.1}$$

where $z = 0$ is the center of the bilayer, z_0 is the slice considered the end of the simulation, and P_t is the total number of water molecules in the considered slices $\sum_{z=0}^{z_0} P_z$. This simulated $\Delta\nu$ is expected to match experimental values computed for the same number of waters per lipid as is simulated. Since ion simulations need upwards of 150 waters per lipid to achieve necessary bulk properties [78], their water to lipid ratio is too high to match with experimental values. Therefore, we assume that we may stop the integration early (z_0 less than the simulated box length) to compute the $\Delta\nu$ for the number of waters per lipid in the region between $\pm z_0$. This approximation has been shown to reproduce experimental values [78] but is considered inaccurate for small numbers of water, where the ordering location and behavior may be altered by the absence of neighboring waters. For ion simulations this error is more significant since ions create additional regions for water to order, which regions water will fill first is unknown from current simulations, Another issue with these approximations is that computing ion concentration in experiments with only a few dozen waters per lipid is extremely difficult.

With these limitations in mind, we have computed the expected $\Delta\nu$ for various limits z_0, and therefore, different waters per lipid for POPC (No Salt), POPC-$MgCl_2^I$, POPC-$CaCl_2$, POPC-LiCl, and POPC-NaCl and plotted them in figure 4.8. $MgCl_2^{II}$ was omitted since it was not significantly different from $MgCl_2^I$. POPC-LiCl and POPC-NaCl data were gathered from simulations in chapter 3. In figure 4.8 we see, in the absence of ions, that POPC (No Salt) has the strongest $\Delta\nu$ with the fewest number of water molecules which are settled in the first region. The quadrupole splitting then reduces, first from water in the oppositely oriented second region, then ultimately by the dilution of oriented waters for bulk. This shape has been shown in experiments with the similar dipalmitoylphosphatidylcholine (DPPC) lipid in work by Gawrisch *et al.* [17]. Ion simulation, such as POPC-$CaCl_2$, POPC-LiCl, and POPC-NaCl have less water in the first region, and a more

ordered second region; therefore, most of its quadrupole splitting is dominated by the water in the positive second region. In the ionic simulations, water from the third region reduces the quadrupole splitting until it surpasses the second region and becomes the dominant source. $MgCl_2^{II}$ has a more significant amount of water in the first region than any other ion creating an additional initial competition and thus $\Delta\nu$ drops faster than any other ion.

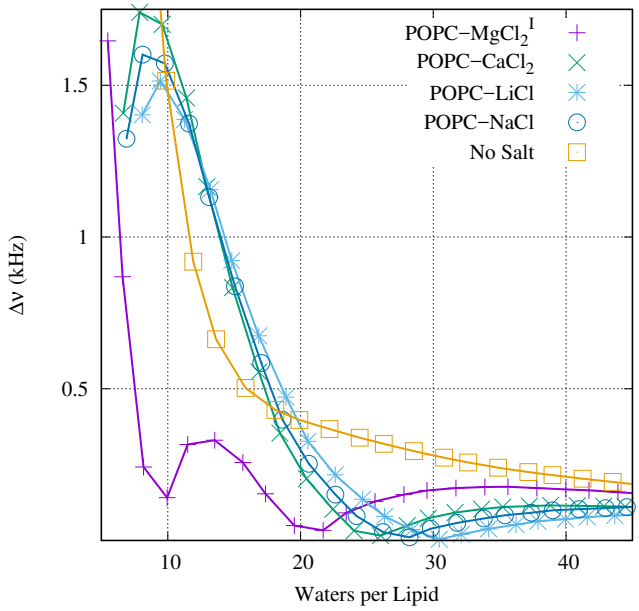

Figure 4.8: A plot of estimated values of $\Delta\nu$ calculated from second rank water order as a function of the number of water molecules per lipid considered. These plots have been calculated for POPC (No Salt) in orange, POPC-$MgCl_2^I$ in purple, POPC-$CaCl_2$ in green, POPC-LiCl in blue, and POPC-NaCl in dark blue.

Coordination Number

Solvation shells of ions are an important distinguishing feature. Coordination numbers are thought to be used as selection criteria for ions in bilayers [79] and proteins. In section 3.3.2 we examined the coordination number, of various solvation oxygens, of monovalent cations as a function of distance from the center of the bilayer. We repeat this process for the divalent cations simulated in this chapter and plot them in figure 4.9. We note in this figure, Mg^{2+} in POPC-$MgCl_2^I$ and POPC-$MgCl_2^{II}$ simulations retained a solvation shell nearly filled by water oxygen. This is in contrast to Ca^{2+} and all previous monovalent cations in figure 3.5, in which other lipid oxygen

atoms replace most water oxygens as they entered the head group of the bilayer. The reason for Mg^{2+} retaining its water comes from the higher potential differences calculated from the force field parameters. We also note that Mg^{2+} has a coordination number of ~ 6, similar to Na^{+}, and Ca^{2+} has a coordination number of ~ 8 in bulk water but loses ~ 1 oxygen as it enters the head group region.

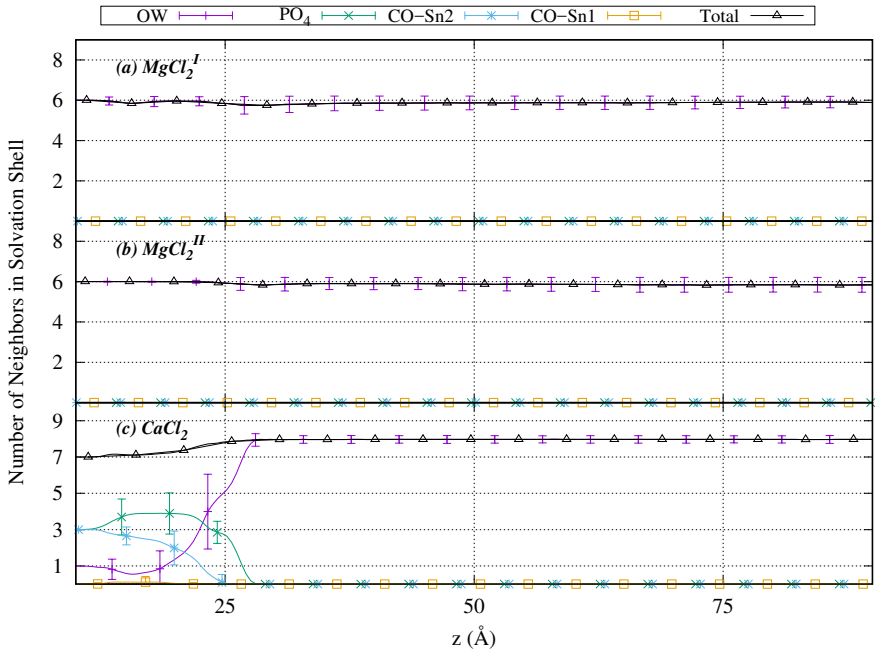

Figure 4.9: The number of each type of oxygen atom, and the total number of oxygen atoms, in the solvation shell of the simulated cation in each of the salt simulations: (a) $MgCl_2^I$, (b) $MgCl_2^{II}$, (c) $CaCl_2$. Oxygen types include water oxygen, OW (purple), phosphate oxygen (green), Sn–2 side carbonyl, CO-Sn2 (blue), Sn–1 side carbonyl, CO–Sn1 (orange), and the total number of oxygen (black).

Categorizing Solvation Shell

Since we know Mg^{2+} and Li^{+} competition is an important mechanism of Li^{+} action [72], we are interested in what are the shapes of biological binding points accepted by each ion. We, therefore, propose the following method to classify solvation shells. The software was developed which maps a cluster of atoms to a completely connected, colored, weighted graph. The software then hashes each graph to a unique bin for each isomorphism of the graph. This software was used on clusters of oxygen atoms in the solvation shell of cations and the cations themselves.

An example of this process, in two dimensions, is outlined in detail in figure 4.10. The detailed steps of the algorithm are as follows. In each step of the simulation, for each cation, all neighboring oxygen in the cutoff distance (R) is included in the cluster (see figure 4.10a). The cutoff distance is determined in advance from the location of the trough after the first peak in the cation–oxygen RDF as described in section 3.3.2. Each atom in the cluster is indexed according to the distance from the cation, starting with the cation itself as index 0. The closest oxygen is then indexed as 1, etc. Figure 4.10b shows how this indexing may look. Each index atom is then made vertices in the graph. The edges of this graph are therefore E_{ij}, for each pair of atoms with index i and j where $i < j$ (see figure 4.10c). Since every pair of vertices makes an edge, the graph is completely connected. The first N edges, N being the number of oxygens atoms in the graph, are therefore all the edges which include the target cation. These edges are denoted as dark blue in figure 4.10c while all other edges are light blue. The edges are then weighted (or colored) using the function,

$$W_{ij} = \left\lfloor \frac{R_{ij}}{W_B} \right\rfloor, \tag{4.2}$$

where R_{ij} is the distance between the real position of the atoms which map to the vertices and W_B is a tunable weight parameter. The $\lfloor\rfloor$ symbol denotes the floor function which takes a real number and returns the largest integer lower than the inputted real number. Examples of weights, thus computed, are shown in figure 4.10d for a two-dimensional example. The graph can then be represented as the list of weights (W_{ij}) in order of the vertices which compose them. This list for the example in figure 4.10d would be $\{4, 4, 4, 5, 4, 6, 5, 6, 5\}$. Graphs are then inserted into a hash table which tracks the population of each class of graph.

After all clusters have been processed and inserted into the graph, the software prints a list of the registered graphs and the total occurrences of that graph (N_i). Choice of W_B is not arbitrary. Large values of W_B result in the reduction of the diversity of weights and therefore the diversity of graphs. In the case of $W_B > 2R$, since no distance is greater than the twice the cutoff all weights would be 0, and all graphs with the same number of vertices would be equal. When a small value for W_B is chosen, the diversity of edges is increased, and consequently, the increase in the diversity of graphs. In the limit of W_B going to zero, each graph is unique, and therefore not a useful way of classifying. We have found that $W_B = 0.3\mathring{A}$ is a good weight which allows for a balance of variety

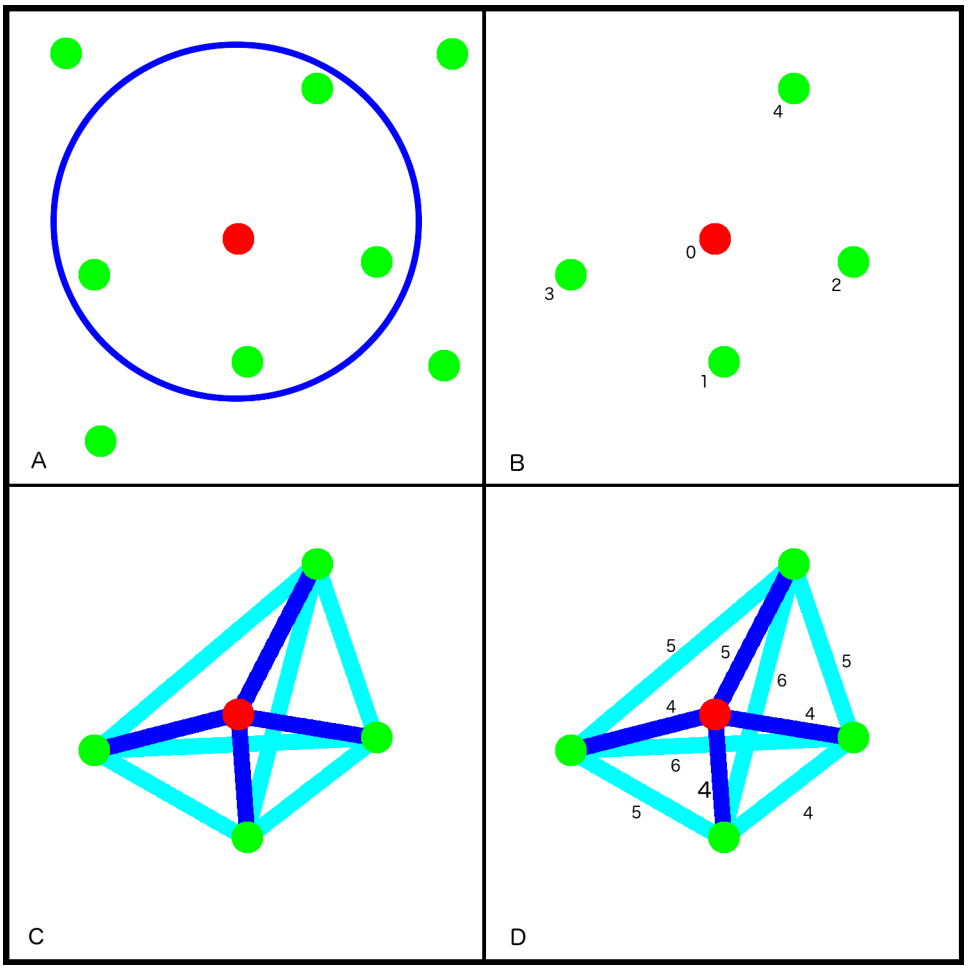

Figure 4.10: Drawing of a two-dimensional example of the process of mapping of three-dimensional clusters of atoms to complete, weighted, graph in order to categorize hydration shell configuration. The four figures demonstrate four steps of the process: (a) For each target, noted with a red dot, all hydration shell atoms in the cutoff distance identified. (b) All atoms in the cluster are mapped to nodes in the cluster, the number of the node is the atoms distance from the target, with the target being the 0-th node. (c) An edge is defined for each none identical pair of nodes, *i.e.*a complete graph. (d) The weight, or color, of the edge, is determined by the distance between the atoms which make up the vertices of the edge.

and density.

Overlap of Solvation Shells

The result of the process described above is a set of graphs for each cation (S_{Li}, S_{Na}, S_{Mg}, S_{Ca}) and a count of occurrences for each member in the set ($N_{Li,i}$, $N_{Na,i}$, $N_{Mg,i}$, $N_{Ca,i}$). We would like to use these sets to determine similarities in the solvation shells, in particular, we would like

to determine the most probable fraction of the weighted edges which match the weights of another set. To compute this value, we developed the following procedure. First, we select a source (S_s) and target (S_t) set such that we would like to determine the average fraction of each source graph ($S_{s,i}$) with all target graphs ($S_{t,i}$). To accomplish this for each $S_{s,i}$, for each $S_{t,i}$, we first determine the greatest sub-graph isomorphism, *i.e.*, the mapping between graphs which the highest number of edges match. The number of edges that match in the greatest sub-graph isomorphism, divided by the number of edges in the smaller graph (the most number of edges that could match) is taken as the greatest percent overlap of $S_{s,i}$ with $S_{t,i}$. The most probable overlap for $S_{s,i}$ with the set S_t, is then taken to be the weighted sum of all of these greatest percent overlap, weighted by the population of the target graph $N_{t,i}$.

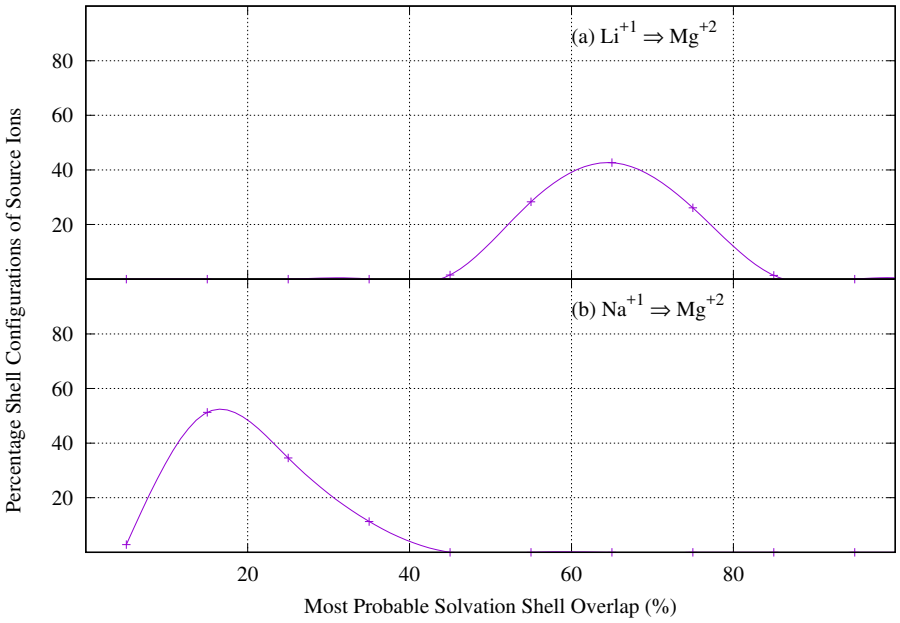

Figure 4.11: Distribution of the most probable solvation shell overlap. Plotted for (a) Li^+ into Mg^{2+} and (b) Na^+ into Mg^{2+}. This figure demonstrates the significantly greater overlap of Li^+ into Mg^{2+} than Na^+.

The result of this process is the set of most probable overlaps of $S_{s,i}$ with the set S_t and a number of the occurrence of $S_{s,i}$, $N_{s,i}$. To best visualize the most probable overlaps of a set, we then bin the most probable overlaps, counting the occurrence of the graphs which obtain the overlap and then divide by the total count to determine the percent of each source graph, *i.e.*the configuration,

which has a probable solvation shell overlap in the said range of the bin. Figure 4.11 is a plot of the percent of shell configurations which have a probable shell overlap in each ten percent range for Li^+ into Mg^{2+} and Na^+ into Mg^{2+}. In this figure, the peak in probable shell overlap between Li^+ and Mg^{2+} is $\sim 65\%$. This is significantly more than the overlap between Na^+ and Mg^{2+} which peaks at $\sim 15\%$. This more significant overlap between Li^+–Mg^{2+} over Na^+–Mg^{2+} is surprising since Na^+ and Mg^{2+} both since similar coordination numbers, and both have solvation shells which are of the general form an octahedron. An overlap of 65% with Mg^{2+} is significant as the percent overlap of Mg^{2+} with itself yielded peaks at $\sim 75\%$.

We conclude from these figures, that any biological molecule(s) which binds with Mg^{2+} by taking up to four of its coordination shell can be replaced by Li^+ given the replacement is energetically favorable. This conclusion is dependent on the reasonable assumption that the geometry of the coordination shells is not dependent on the types of oxygen in its shell.

Solvation Shell Configuration Energy

Since competition between cation for binding sites is not solely based on solvation shell shape, but also the energetic preference of the configuration, we must determine the energy of the solvation shells. The potential energy of each solvation shells was computed by recalculating Lennard Jones and electrostatic potential between the cation and each oxygen atom in the cutoff distance R, as well as the Lennard Jones and electrostatic potential between each of the oxygen atoms. The potential energy of each solvation shells, for each cation simulated in this chapter and chapter 3, both inside the lipid head group region and outside in bulk water region, was computed and is shown in figure 4.12. These energies can be either positive or negative since they focus solely on the cations and oxygens in the solvation shell, and the negative ion–oxygen interaction can be overcome by the positive oxygen–oxygen repulsion. What is of more interest is the difference in energy between ions and states. The difference in energy for either Mg^{2+} between the bilayer and bulk water is minimal, possibly because Mg^{2+} does not dehydrate in the lipid (see figure 4.9). K^+ and Rb^+ show an energetic preference for bulk water, which is in agreement with their fewer number of ions binding to the lipid compared to other ions. Ions such as Ca^{2+}, Li^+, and Na^+ all show an energetic preference for the bilayer, and also have more ions in the head group or the bilayer than K^+ and Rb^+. Li^+, in particular, has a significant preference for the head group region

of the bilayer. These configuration energy calculations are sensitive to force fields, but differences between $MgCl_2^I$ and $MgCl_2^{II}$ are minimal. This large energetic preference Li^+ has for solvation shells in the bilayer compared to that of Mg^{2+}, and a significant percent of solvation shell overlap between Li^+ and Mg^{2+}, explain how Li^+ competes with Mg^{2+} for lipid binding.

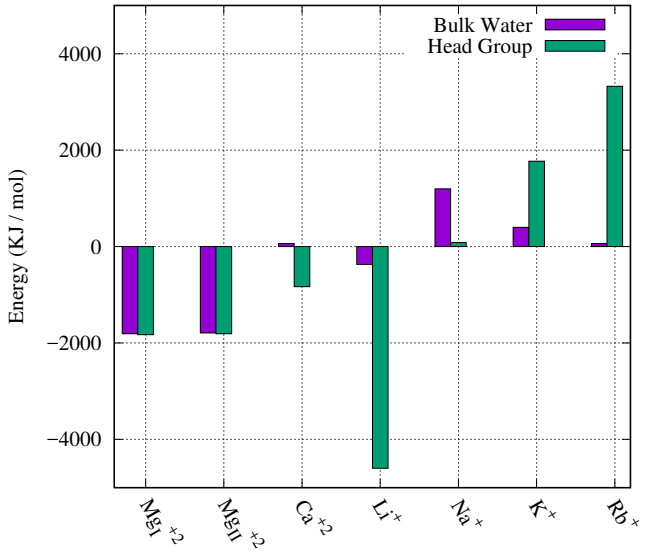

Figure 4.12: Average configuration energy of the solvation shell used to generated overlapping graphs of each ion. The energy of the configurations in bulk water in purple. The energy of configurations inside the head group region of the bilayer is in green.

4.4 Conclusions

POPC lipids were simulated with Mg^{2+} and Ca^{2+} ions using new force fields from Li *et al.* [75] and Allner *et al.* [76]. A single simulation was run with Ca^{2+} from Li *et al.*while two simulations were run with an Mg^{2+} from each group to ensure comparable results. Results calculated from the two simulations with Mg^{2+} force fields yielded very similar results, signifying choice between the two force fields is unimportant in lipid simulations.

Area per lipid of the bilayer A_l was shown to shrink consistently as the amount of charge added from cations located in the head group region of the bilayer. Changes in A_l corresponded with thickening of the bilayer and increase in the order of hydrocarbon chains.

Mg^{2+} was shown to be more chaotropic in the head group region of the bilayer than Ca^{2+}. Plots of coordination of ions determined that Mg^{2+} cations retained full coordination with waters even inside the bilayer. This result was consistent with both Mg^{2+} simulations.

New methods to categorize solvation shells were implemented. This method mapped the shells to a completely connected, weighted graph which was then hashed to count the population of each solvation shell configuration. These graphs were used to compare probable overlap between solvation shells of cations by looking at the sub-graph isomorphisms between graphs. It was determined that large portions of the solvation shell of Li^{+} frequently fit the solvation shells of Mg^{2+}. Therefore, Mg^{2+} may lose its binding to a biological molecule(s) if there is at most a four-fold binding site, for the four oxygen in the solvation shell of Li^{+}.

Average configuration energies of the solvation shells were determined for shells inside and outside the lipid head group for each cation. Li^{+} showed to have a strong, energetic preference for solvation shells inside the bilayer while Mg^{2+} showed no preference either way. This energetic advantage for Li^{+} along with the overlap in probable solvation shell explains the competition between Li^{+} and Mg^{2+} in red blood cell lipid membranes [74].

Chapter 5

Conclusions

Ten simulations were run to further the understanding of lipid bilayer interfaces. Two of these simulations, DPPC and DHPC bilayers, differ only in that the carbon tails of DPPC lipids are ester bonded and therefore contain an additional carbonyl, while DHPC lipids are ether bonded. Eight simulations involved POPC bilayers with different salt ions. Four of these simulations involved monovalent ions, Li^+, Na^+, K^+, and Rb^+, while three of them involved divalent ions of Mg^{2+} and Ca^{2+}. Two of these simulations tested two different force fields for Mg^{2+} with little difference in results.

Simulations with ions revealed several important requirements for lipid/ionic simulations not yet discussed. First, simulations involving ions require more water to reach a bulk solvent region than purely lipid-water simulations. This is due to a bilayers ability to absorb cations more than anions, that will leave the bulk water region acidic if there are not sufficient cations to remain in the bulk region. A ratio of 150:1 water to lipid was used for our simulations of 200 Mm salt concentration. Second, ion simulations take a long amount of time, 200 to 300 ns for ion binding to reach equilibrium. Finally, new force fields for ions improved results including, fixing issues with K^+ ions not hydrating in simulations.

Comparisons between DPPC and DHPC lipids are an excellent choice for a general comparison between ether and ester lipids since the lipids differ only in how the chains are bonded to the backbone. Ether lipids are shown to better perturb water in the interface of the bilayer which makes the water more viscous. This was demonstrated with measurements of water molecules which showed higher water ordering, lower lateral diffusion rates, and longer rotational autocorrelation times.

Despite the lower dipole potential, DHPC is shown to have a higher peak potential, due to the more ordered water in the head group region of the bilayer. This increased peak potential, along with the more frozen region of water, possibly explains the decreased permeability seen in ether

lipids.

Archaea and other microorganisms, which became eukaryotic and prokaryotic life, is one of the earliest known speciation. One of the primary specializations archaea adapted was of its lipid bilayer. This specialization was possible because ether lipids have significant different bulk properties due to the loss of ester carbonyls. Some human tissue, have some portion of lipids with one chain ether bonded. The result of this bond equates to a less permeable surface.

Some changes to lipid bilayers due to the presence of ions are the same regardless of the ion. Ions decrease the area per lipid while increasing thickness, proportional to the number of ions in the head group region times their charge. The total ordering of the carbon chains increases with the addition of ions, proportional to an increase in area. Electrostatic potential increases evenly, proportional to the number of ions times their charge in the head group region. The angle of the head group of the bilayer measured as the P–N angle, straightened as the number and charge of ions that entered the head group region, reduced the increasing dipole potential caused by the cation and anion concentrations in the head group and surface of the bilayer. Water order decreased, proportional to the size of the ion. Pressure profiles of lipid bilayer simulations with ions saw a decrease in the lateral pressure near the surface (D_b) of the bilayer, and an increase in the lateral pressure just outside the bilayer where anions are positioned.

In some ways, ions act distinctly from each other. Li^+ had a very significant preference to include the Sn–2 side carbonyl in its solvation shell when inside the head group region of the bilayer. The energy needed to remove water oxygens from Mg^{2+} is so high that Mg^{2+} would rarely dehydrate. Instead, it would enter the head group region without filling any of its solvation shells with oxygen from the lipid.

Solvation shells of various simulated ions are discretized to graphs and compared by determining the percent of sub-isomorphisms. Li^+ solvation shells have a significant overlap with the solvation shell of Mg^{2+}. Solvation shell energies for ions within or outside the bilayer were compared. Li^+ was found to have a significant difference in energy favoring the solvation shells inside the bilayer. The substantial overlap of solvation Li^+ and Mg^{2+} shells and the greater energetically favorable shells inside the of Li^+ inside the bilayer explains why Li^+ replaces Mg^{2+} in bilayers.

Bibliography

[1] S. J. Singer. "The Fluid Mosaic Model of Membrane Structure". In: *Structure of Biological Membranes*. Ed. by S. Abrahamsson and I. Pascher. Boston, MA: Springer US, 1977, 443–461.

[2] B. Alberts. *Molecular biology of the cell.* New York : Garland Science, c2002., 2002.

[3] J. N. Israelachvili, D. J. Mitchell, and B. W. Ninham. "Theory of self-assembly of lipid bilayers and vesicles". *Biochimica et Biophysica Acta (BBA)-Biomembranes* 470 (1977), 185–201.

[4] E. Fahy, D. Cotter, M. Sud, and S. Subramaniam. "Lipid classification, structures and tools". *Biochimica et Biophysica Acta (BBA)-Molecular and Cell Biology of Lipids* 1811 (2011), 637–647.

[5] N. E. Braverman and A. B. Moser. "Functions of plasmalogen lipids in health and disease". *Biochimica et Biophysica Acta (BBA)-Molecular Basis of Disease* 1822 (2012), 1442–1452.

[6] Y. Koga. "From promiscuity to the lipid divide: on the evolution of distinct membranes in archaea and bacteria". *Journal of molecular evolution* 78 (2014), 234–242.

[7] J. Lombard, P. López-Garca, and D. Moreira. "The early evolution of lipid membranes and the three domains of life". *Nature Reviews Microbiology* 10 (2012), 507–515.

[8] E. J. Dufourc. "Sterols and membrane dynamics". *Journal of chemical biology* 1 (2008), 63–77.

[9] S. A. Pandit, G. Khelashvili, E. Jakobsson, A. Grama, and H. Scott. "Lateral organization in lipid-cholesterol mixed bilayers". *Biophysical journal* 92 (2007), 440–447.

[10] D. L. Valentine. "Adaptations to energy stress dictate the ecology and evolution of the Archaea". *Nat Rev Micro* 5 (2007), 316–323.

[11] H.-J. Hinz and F. P. Schwarz. "Measurement and analysis of results obtained on biological substances with differential scanning calorimetry (IUPAC Technical Report)". *Pure and Applied Chemistry* 73 (2001), 745–759.

[12] M. H. Chiu and E. J. Prenner. "Differential scanning calorimetry: an invaluable tool for a detailed thermodynamic characterization of macromolecules and their interactions". *Journal of Pharmacy and Bioallied Sciences* 3 (2011), 39.

[13] N. Kuerka, J. F. Nagle, J. N. Sachs, S. E. Feller, J. Pencer, A. Jackson, and J. Katsaras. "Lipid bilayer structure determined by the simultaneous analysis of neutron and X-ray scattering data". *Biophysical journal* 95 (2008), 2356–2367.

[14] J. C. Fogarty, M. Arjunwadkar, S. A. Pandit, and J. Pan. "Atomically detailed lipid bilayer models for the interpretation of small angle neutron and X-ray scattering data". *Biochimica et Biophysica Acta (BBA)-Biomembranes* 1848 (2015), 662–672.

[15] J. F. Nagle and S. Tristram-Nagle. "Structure of lipid bilayers". *Biochimica et Biophysica Acta (BBA)-Reviews on Biomembranes* 1469 (2000), 159–195.

[16] A. Leftin, T. R. Molugu, C. Job, K. Beyer, and M. F. Brown. "Area per lipid and cholesterol interactions in membranes from separated local-field 13C NMR spectroscopy". *Biophysical journal* 107 (2014), 2274–2286.

[17] K. Gawrisch, D. Ruston, J. Zimmerberg, V. Parsegian, R. Rand, and N. Fuller. "Membrane dipole potentials, hydration forces, and the ordering of water at membrane surfaces". *Biophysical journal* 61 (1992), 1213–1223.

[18] G. Cevc. *Phospholipids handbook*. CRC press, 1993.

[19] S. A. Pandit, S.-w. Chiu, E. Jakobsson, and H. L. Scott. "Atomistic and mean field simulations of lateral organization in membranes". *Current Topics in Membranes* 60 (2008), 281–312.

[20] S. Nosé and M. Klein. "Constant pressure molecular dynamics for molecular systems". *Molecular Physics* 50 (1983), 1055–1076.

[21] M. Parrinello and A. Rahman. "Polymorphic transitions in single crystals: A new molecular dynamics method". *Journal of Applied physics* 52 (1981), 7182–7190.

[22] T. Darden, D. York, and L. Pedersen. "Particle mesh Ewald: An N log (N) method for Ewald sums in large systems". *The Journal of chemical physics* 98 (1993), 10089–10092.

[23] J. C. Fogarty, S.-W. Chiu, P. Kirby, E. Jakobsson, and S. A. Pandit. "Automated optimization of water–water interaction parameters for a coarse-grained model". *The Journal of Physical Chemistry B* 118 (2014), 1603–1611.

[24] S.-W. Chiu, S. A. Pandit, H. Scott, and E. Jakobsson. "An improved united atom force field for simulation of mixed lipid bilayers". *The Journal of Physical Chemistry B* 113 (2009), 2748–2763.

[25] S. E. Feller and R. W. Pastor. "Constant surface tension simulations of lipid bilayers: the sensitivity of surface areas and compressibilities". *The Journal of chemical physics* 111 (1999), 1281–1287.

[26] K. Åman, E. Lindahl, O. Edholm, P. Håkansson, and P.-O. Westlund. "Structure and dynamics of interfacial water in an L α phase lipid bilayer from molecular dynamics simulations". *Biophysical journal* 84 (2003), 102–115.

[27] R. Goetz and R. Lipowsky. "Computer simulations of bilayer membranes : Self-assembly and interfacial tension". *Journal of Chemical Physics* 108 (1998), 7397–7409.

[28] J. Sonne, F. Y. Hansen, and G. H. Peters. "Methodological problems in pressure profile calculations for lipid bilayers". *The Journal of Chemical Physics* 122 (2005).

[29] J. M. Vanegas, A. Torres-Sánchez, and M. Arroyo. "Importance of force decomposition for local stress calculations in biomembrane molecular simulations". *Journal of chemical theory and computation* 10 (2014), 691–702.

[30] E. Lindahl and O. Edholm. "Spatial and energetic-entropic decomposition of surface tension in lipid bilayers from molecular dynamics simulations". *The Journal of Chemical Physics* 113 (2000), 3882–3893.

[31] L. J. Pike, X. Han, K.-N. Chung, and R. W. Gross. "Lipid rafts are enriched in arachidonic acid and plasmenylethanolamine and their composition is independent of caveolin-1 expression: a quantitative electrospray ionization/mass spectrometric analysis". *Biochemistry* 41 (2002), 2075–2088.

[32] P. J. Sindelar, Z. Guan, G. Dallner, and L. Ernster. "The protective role of plasmalogens in iron-induced lipid peroxidation". *Free Radical Biology and Medicine* 26 (1999), 318–324.

[33] L. Kuerschner, D. Richter, H. K. Hannibal-Bach, A. Gaebler, A. Shevchenko, C. S. Ejsing, and C. Thiele. "Exogenous ether lipids predominantly target mitochondria". *PLoS One* 7 (2012), e31342.

[34] S. D. Guler, D. D. Ghosh, J. Pan, J. C. Mathai, M. L. Zeidel, J. F. Nagle, and S. Tristram-Nagle. "Effects of ether vs. ester linkage on lipid bilayer structure and water permeability". *Chemistry and physics of lipids* 160 (2009), 33–44.

[35] D. Balleza, A. B. Garcia-Arribas, J. Sot, K. Ruiz-Mirazo, and F. M. Goñi. "Ether-versus ester-linked phospholipid bilayers containing either linear or branched apolar chains". *Biophysical journal* 107 (2014), 1364–1374.

[36] J. Pan, X. Cheng, F. A. Heberle, B. Mostofian, N. Kuerka, P. Drazba, and J. Katsaras. "Interactions between ether phospholipids and cholesterol as determined by scattering and molecular dynamics simulations". *The Journal of Physical Chemistry B* 116 (2012), 14829–14838.

[37] J. F. Nagle, J. C. Mathai, M. L. Zeidel, and S. Tristram-Nagle. "Theory of passive permeability through lipid bilayers". *The Journal of general physiology* 131 (2008), 77–85.

[38] K. Shinoda, W. Shinoda, T. Baba, and M. Mikami. "Comparative molecular dynamics study of ether-and ester-linked phospholipid bilayers". *The Journal of chemical physics* 121 (2004), 9648–9654.

[39] M. J. Abraham, T. Murtola, R. Schulz, S. Páll, J. C. Smith, B. Hess, and E. Lindahl. "GROMACS: High performance molecular simulations through multi-level parallelism from laptops to supercomputers". *SoftwareX* 1 (2015), 19–25.

[40] B. Hess, H. Bekker, H. J. C. Berendsen, and J. G. E. M. Fraaije. "LINCS: A linear constraint solver for molecular simulations". *Journal of Computational Chemistry* 18 (1997), 1463–1472.

[41] U. Essmann, L. Perera, M. L. Berkowitz, T. Darden, H. Lee, and L. G. Pedersen. "A smooth particle mesh Ewald method". *The Journal of chemical physics* 103 (1995), 8577–8593.

[42] M. Frisch, G. Trucks, H. Schlegel, G. Scuseria, M. Robb, J. Cheeseman, V. Zakrzewski, J. Montgomery Jr, R. Stratmann, J. Burant, et al. "Gaussian 98, revision A. 7". *Gaussian Inc., Pittsburgh, PA* 49 (1998).

[43] W. Rawicz, K. Olbrich, T. McIntosh, D. Needham, and E. Evans. "Effect of chain length and unsaturation on elasticity of lipid bilayers". *Biophysical journal* 79 (2000), 328–339.

[44] J. C. Fogarty, M. Arjunwadkar, S. A. Pandit, and J. Pan. "Atomically detailed lipid bilayer models for the interpretation of small angle neutron and X-ray scattering data". *Biochimica et Biophysica Acta (BBA)-Biomembranes* 1848 (2015), 662–672.

[45] A. Cordomi, O. Edholm, and J. J. Perez. "Effect of ions on a dipalmitoyl phosphatidylcholine bilayer. A molecular dynamics simulation study". *The Journal of Physical Chemistry B* 112 (2008), 1397–1408.

[46] H. Akutsu and T. Nagamori. "Conformational analysis of the polar head group in phosphatidylcholine bilayers: a structural change induced by cations". *Biochemistry* 30 (1991), 4510–4516.

[47] J. Seelig, P. M. MacDonald, and P. G. Scherer. "Phospholipid head groups as sensors of electric charge in membranes". *Biochemistry* 26 (1987), 7535–7541.

[48] W. Young. "Review of lithium effects on brain and blood." *Cell transplantation* 18 (2008), 951–975.

[49] J. F. Cade. "Lithium salts in the treatment of psychotic excitement." *Medical Journal of Australia* (1949).

[50] G. Pabst, A. Hodzic, J. trancar, S. Danner, M. Rappolt, and P. Laggner. "Rigidification of neutral lipid bilayers in the presence of salts". *Biophysical journal* 93 (2007), 2688–2696.

[51] R. A. Böckmann, A. Hac, T. Heimburg, and H. Grubmüller. "Effect of sodium chloride on a lipid bilayer". *Biophysical Journal* 85 (2003), 1647–1655.

[52] H. Binder and O. Zschörnig. "The effect of metal cations on the phase behavior and hydration characteristics of phospholipid membranes". *Chemistry and physics of lipids* 115 (2002), 39–61.

[53] M. Eisenberg, T. Gresalfi, T. Riccio, and S. McLaughlin. "Adsorption of monovalent cations to bilayer membranes containing negative phospholipids". *Biochemistry* 18 (1979), 5213–5223.

[54] S. A. Simon, T. J. McIntosh, and A. D. Magid. "Magnitude and range of the hydration pressure between lecithin bilayers as a function of headgroup density". *Journal of colloid and interface science* 126 (1988), 74–83.

[55] S. A. Pandit, D. Bostick, and M. L. Berkowitz. "Molecular dynamics simulation of a dipalmitoylphosphatidylcholine bilayer with NaCl". *Biophysical journal* 84 (2003), 3743–3750.

[56] A. Cordomi, O. Edholm, and J. J. Perez. "Effect of force field parameters on sodium and potassium ion binding to dipalmitoyl phosphatidylcholine bilayers". *Journal of chemical theory and computation* 5 (2009), 2125–2134.

[57] A. A. Gurtovenko and I. Vattulainen. "Calculation of the electrostatic potential of lipid bilayers from molecular dynamics simulations: Methodological issues". *The Journal of chemical physics* 130 (2009), 215107.

[58] I. S. Joung and T. E. Cheatham III. "Determination of alkali and halide monovalent ion parameters for use in explicitly solvated biomolecular simulations". *The journal of physical chemistry B* 112 (2008), 9020–9041.

[59] M. L. Berkowitz, D. L. Bostick, and S. Pandit. "Aqueous solutions next to phospholipid membrane surfaces: insights from simulations". *Chemical reviews* 106 (2006), 1527–1539.

[60] B. Hess, C. Kutzner, D. Van Der Spoel, and E. Lindahl. "GROMACS 4: algorithms for highly efficient, load-balanced, and scalable molecular simulation". *Journal of chemical theory and computation* 4 (2008), 435–447.

[61] D. Van Der Spoel, E. Lindahl, B. Hess, G. Groenhof, A. E. Mark, and H. J. Berendsen. "GROMACS: fast, flexible, and free". *Journal of computational chemistry* 26 (2005), 1701–1718.

[62] E. Lindahl, B. Hess, and D. Van Der Spoel. "GROMACS 3.0: a package for molecular simulation and trajectory analysis". *Molecular modeling annual* 7 (2001), 306–317.

[63] H. J. Berendsen, D. van der Spoel, and R. van Drunen. "GROMACS: a message-passing parallel molecular dynamics implementation". *Computer Physics Communications* 91 (1995), 43–56.

[64] A. A. Gurtovenko and I. Vattulainen. “Effect of NaCl and KCl on phosphatidylcholine and phosphatidylethanolamine lipid membranes: insight from atomic-scale simulations for understanding salt-induced effects in the plasma membrane”. *The Journal of Physical Chemistry B* 112 (2008), 1953–1962.

[65] S. Obst and H. Bradaczek. “Molecular dynamics study of the structure and dynamics of the hydration shell of alkaline and alkaline-earth metal cations”. *The Journal of Physical Chemistry* 100 (1996), 15677–15687.

[66] F. Jahnig. “What is the surface tension of a lipid bilayer membrane?” *BIOPHYSICAL JOURNAL* 71 (1996), 1348–1349.

[67] R. S. Cantor. “Lateral pressures in cell membranes: a mechanism for modulation of protein function”. *The Journal of Physical Chemistry B* 101 (1997), 1723–1725.

[68] B. Klasczyk, V. Knecht, R. Lipowsky, and R. Dimova. “Interactions of alkali metal chlorides with phosphatidylcholine vesicles”. *Langmuir* 26 (2010), 18951–18958.

[69] A. McLaughlin, C. Grathwohl, and S. McLaughlin. “The adsorption of divalent cations to phosphatidylcholine bilayer membranes”. *Biochimica et Biophysica Acta (BBA)-Biomembranes* 513 (1978), 338–357.

[70] S. McLaughlin. “The electrostatic properties of membranes”. *Annual review of biophysics and biophysical chemistry* 18 (1989), 113–136.

[71] L. Nanninga and R. Kempen. “Role of magnesium and calcium in the first and second contraction of glycerin-extracted muscle fibers”. *Biochemistry* 10 (1971), 2449–2456.

[72] E. Jakobsson, O. Argüello-Miranda, S.-W. Chiu, Z. Fazal, J. Kruczek, S. Nunez-Corrales, S. Pandit, and L. Pritchet. “Towards a unified understanding of lithium action in basic biology and its significance for applied biology”. *The Journal of membrane biology* 250 (2017), 587–604.

[73] P. S. Klein and D. A. Melton. “A molecular mechanism for the effect of lithium on development”. *Proceedings of the National Academy of Sciences* 93 (1996), 8455–8459.

[74] C. Srinivasan, N. Minadeo, C. F. Geraldes, and D. M. de Freitas. “Competition between Li+ and Mg2+ for red blood cell membrane phospholipids: a 31P, 7Li, and 6Li nuclear magnetic resonance study”. *Lipids* 34 (1999), 1211–1221.

[75] P. Li, B. P. Roberts, D. K. Chakravorty, and K. M. Merz Jr. “Rational design of particle mesh Ewald compatible Lennard-Jones parameters for+ 2 metal cations in explicit solvent”. *Journal of chemical theory and computation* 9 (2013), 2733–2748.

[76] O. Allnér, L. Nilsson, and A. Villa. “Magnesium ion–water coordination and exchange in biomolecular simulations”. *Journal of Chemical Theory and Computation* 8 (2012), 1493–1502.

[77] C. Bergonzo, K. B. Hall, and T. E. Cheatham. “Divalent Ion Dependent Conformational Changes in an RNA Stem-Loop Observed by Molecular Dynamics”. *Journal of Chemical Theory and Computation* 12 (2016). PMID: 27294370, 3382–3389.

[78] J. Kruczek, S.-W. Chiu, E. Jakobsson, and S. A. Pandit. “Effects of Lithium and Other Monovalent Ions on Palmitoyl Oleoyl Phosphatidylcholine Bilayer”. *Langmuir* 33 (2017). PMID: 28076953, 1105–1115.

[79] N. Vlachy, B. Jagoda-Cwiklik, R. Vácha, D. Touraud, P. Jungwirth, and W. Kunz. “Hofmeister series and specific interactions of charged headgroups with aqueous ions”. *Advances in colloid and interface science* 146 (2009), 42–47.

[80] C. B. Raub, A. J. Putnam, B. J. Tromberg, and S. C. George. "Predicting bulk mechanical properties of cellularized collagen gels using multiphoton microscopy". *Acta Biomaterialia* 6 (2010), 4657–4665.

[81] P. J. Flory, N. Rabjohn, and M. C. Shaffer. "Dependence of elastic properties of vulcanized rubber on the degree of cross linking". *Journal of Polymer Science* 4 (1949), 225–245.

[82] G. Lewis. "Properties of crosslinked ultra-high-molecular-weight polyethylene". *Biomaterials* 22 (2001), 371–401.

[83] C. C. Reed and R. V. Iozzo. "The role of decorin in collagen fibrillogenesis and skin homeostasis". *Glycoconjugate Journal* 19 (4 2002). 10.1023/A:1025383913444, 249–255.

[84] E. J. G. Peterman and J. M. Scholey. "Mitotic microtubule crosslinkers: insights from mechanistic studies". *Current Biology* 19 (2009), R1089–R1094.

[85] I. Jager and P. Fratzl. "Mineralized collagen fibrils: a mechanical model with a staggered arrangement of mineral particles". *Biophysical Journal* 79 (2000), 1737–1746.

[86] C. Storm, J. J. Pastore, F. C. MacKintosh, T. C. Lubensky, and P. A. Janmey. "Nonlinear elasticity in biological gels". *Nature* 435 (2005), 191–194.

[87] M. L. Gardel, J. H. Shin, F. C. MacKintosh, L. Mahadevan, P. Matsudaira, and D. A. Weitz. "Elastic behavior of cross-linked and bundled actin networks". *Science* 304 (2004), 1301–1305.

[88] D. A. Head, A. J. Levine, and F. C. MacKintosh. "Deformation of cross-linked semiflexible polymer networks". *Physical Review Letters* 91 (2003), 108102.

[89] E. Conti and F. C. MacKintosh. "Cross-linked networks of stiff filaments exhibit negative normal stress". *Physical Review Letters* 102 (2009), 088102.

[90] C. Heussinger, F. Schüller, and E. Frey. "Statics and dynamics of the wormlike bundle model". *Physical Review E* 81 (2010), 021904.

[91] C. P. Broedersz, M. Depken, N. Y. Yao, M. R. Pollak, D. A. Weitz, and F. C. MacKintosh. "Cross-Link-Governed Dynamics of Biopolymer Networks". *Physical Review Letters* 105 (2010), 238101.

[92] Z. Qin and M. J. Buehler. "Mechanical properties of crosslinks controls failure mechanism of hierarchical intermediate filament networks". *Theoretical and Applied Mechanics Letters* 2 (2012), 014005.

[93] J. P. R. O. Orgel, J. D. San Antonio, and O. Antipova. "Molecular and structural mapping of collagen fibril interactions". *Connective Tissue Research* 52 (2011), 2–17.

[94] X. Liu, M.-L. Yeh, J. L. Lewis, and Z.-P. Luo. "Direct measurement of the rupture force of single pair of decorin interactions". *Biochemical and Biophysical Research Communications* 338 (2005), 1342–1345.

[95] N. Metropolis, A. W. Rosenbluth, M. N. Rosenbluth, A. H. Teller, and E. Teller. "Equation of state calculations by fast computing machines". *Journal of Chemical Physics* 21 (1953), 1087–1092.

[96] J. Lapujoulade. "The roughening of metal surfaces". *Surface Science Reports* 20 (1994), 195–249.

[97] A. G. Constantine and P. Hall. "Characterizing surface smoothness via estimation of effective fractal dimension". *Journal of the Statistical Society B* 56 (1994), 97–113.

[98] T. Gneiting and M. Schlather. “Stochastic models that separate fractal dimension and the Hurst effect”. *SIAM Review* 46 (2004), 269–282.

[99] T. Koob, M. Koob-Emunds, and J. Trotter. “Cell-derived stiffening and plasticizing factors in sea cucumber (Cucumaria frondosa) dermis”. *Journal of Experimental Biology* 202 (1999), 2291–2301.

[100] J. Kruczek, M. Saunders, M. Khosla, Y. Tu, and S. A. Pandit. “Molecular dynamics simulations of ether-and ester-linked phospholipids”. *Biochimica et Biophysica Acta (BBA)-Biomembranes* 1859 (2017), 2297–2307.

[101] C. B. Bennett, J. Kruczek, D. Rabson, W. G. Matthews, and S. A. Pandit. “The effect of cross-link distributions in axially-ordered, cross-linked networks”. *Journal of Physics: Condensed Matter* 25 (2013), 285101.

[102] J. Kruczek, S.-W. Chiu, S. Varma, E. Jakobsson, and S. A. Pandit. “Interactions of Mono- and Di- valent cations at Palmitoyl Oleoyl Phosphatidylcholine Interface”. In preparation. 2019.

Appendix A

Previous Work on Collagen Fibers

A.1 Introduction

Cross-linked polymeric materials are critical in biomimetic applications due to their complex and versatile mechanical properties. Collagen fibers, with proteoglycan cross-links, create a variety of tissue [80]. This diversity in the physical properties of tissue, such as collagen, cannot be solely due to structural differences in constituent polymer chains, but rather these properties are connected to variations in cross-linking structures [80–82]. A significant illustration is the result of disrupted cross-links on collagen fibrillogenesis [83]. Microtubule bundling and actin networks have been used to show the effects on the physical properties of tissue due to the cross-linkers. Their cross-links determine polarity patterns of these microtubule bundles.

Polarity patterns of these microtubule bundles are determined by their cross-links[84]. Slight changes to the cross-link concentration of actin networks alter the mechanical stiffness of the bundles by a significant factor.

Many compelling models for cross-link polymer materials have been proposed. These models include the study of well-aligned, stiff fibrils work by Jager *et al.* [85], work on the elasticity of cross-linked random networks [86–89], and models by Heussinger *et al.* [90] studied the bulk properties of cross-linked worm-like chains. Still more work by Broedersz *et al.* [91] modeled the long-time dynamics of transient cross-linked networks, and more recently, models by Qin *et al.* [92] examined the failure of intermediate filament networks caused by the strength of cross-links. We propose in this work a simple model in order to isolate how changes to density and strength of cross-links alter the thermodynamic and mechanical properties of the bulk material. This model matches well with the rod-like, well-aligned, cross-linked collagen fibers found in a tendon.

A.2 Model

Our model is that of a simple three-dimensional lattice of rod-like fibers, with fix density of potential cross-link sites along the rods of the lattice (see figure A.1 a). By simple three-dimensional lattice, we mean a collection of "binding sites" at regular intervals in three dimensions, x, y, and z from some origin position at ($x = 0$,$y = 0$,$z = 0$) to some opposite corner at ($x = N_x$,$y = N_y$,$z = N_z$).

By rod-like fibers, we mean to say that the sites along the z dimension, are considered to be on the same fiber, and therefore, shifts in sites can only occur in the $\pm$ z-direction and that all sites within the same fiber (having the same x and y) must shift by the same amount. These fibers can be thought of as lying on a two-dimensional lattice, x and y. These fibers are modeled as stiff chains, unable to bend. We also apply two restrictions on the fibers. Fibers themselves do not interact directly but interact only through "cross-linking" as described below, and only the four "neighboring" fibers can have cross-links. Two fibers must be one lattice space away ($\pm$ 1 x or $\pm$ 1 y) to be considered "neighbors". The definition of fiber in the context of this model means the number of "binding sites" on a fiber N is therefore fixed $N = N_z$.

When we say the model has, fix density of potential cross-link sites along the rods, we imply that some fraction of the sites in the lattice, ρ, can "cross-link" to another similar site on a neighboring fiber. These sites which can be "cross-linked", we will refer to as "active binding sites" (ABS). Whenever two ABS, of two neighboring fibers, share the same z position, we consider the sites to be "cross-linked". The number of ABS on each fiber n is constrained by the equation $\rho = n/N$ (see figure A.1 b). These ABS are fixed to their site on the fiber, and therefore when the fiber shifts, all ABS shift the same amount along the $\pm z$. Unless otherwise noted, we restrict the placement of ABS to random locations along the fiber.

In our model, we also add periodic conditions to the lattice in the dimension perpendicular to the fibers. This addition allows fibers on the edges of the two-dimensional lattice of fibers, which would thereby be missing a neighbor, to consider the fiber on the opposite side of the lattice to be its neighbor. Therefore all fibers have four neighbors, and the model approximates an infinitely thick bundle of fibers.

These restriction allows the model to approximate collagen fibrils in the tendon, where well-

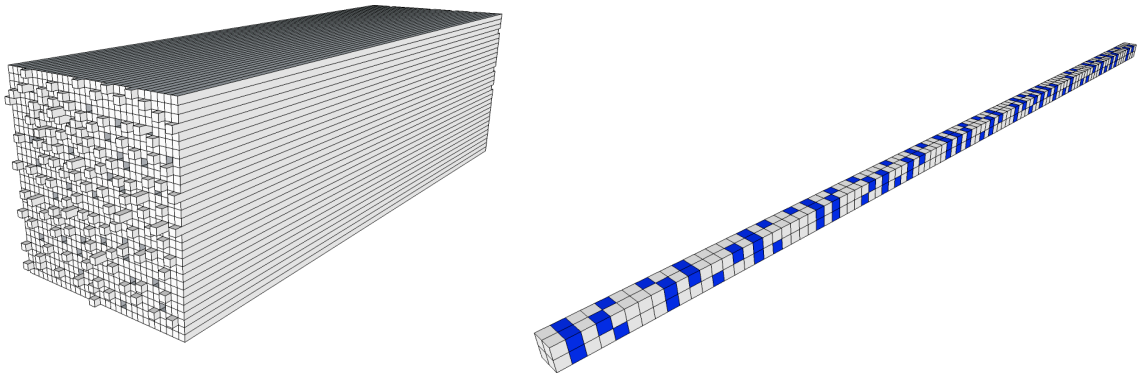

(a) (b)

Figure A.1: (a) An illustration of the lattice with some portion of fibers shifted and (b) isolation of four fibers from within the lattice. A grid is projected on the four fibers denoting "binding sites with "Active binding sites" (ABS) colored in blue. Whenever two blue ABS align, a cross-link is formed.

aligned fibrils have d-band locations at a fixed periodic interval which can contain the cross-linking molecule proteoglycan [93]. Therefore d-band sites map to binding sites on the lattice while d-band sites which contain a proteoglycan map to an ABS which can form a cross-link.

For cross-links to be stable, they must be energetically stable and therefore have a reduction of energy in the system when a cross-link is formed. We, therefore, define the Hamiltonian of the system as

$$\mathcal{H} = -\frac{1}{2} J \sum_{\langle i,j \rangle} \mathbf{S}_i \cdot \mathbf{S}_j \tag{A.1}$$

Where i and j are indices of neighboring fibers, and the summation is over all neighboring pairs of fibers, J is the cross link energy, $\mathbf{S}_i$ is a vector representing a fiber, $\mathbf{S}_i = \{s_{i0}, s_{i1}, ..., s_{ik}, ..., s_{i,N-1}\}$, where s_{ik} is some positive value when k is the location of an ABS and zero otherwise, and $\mathbf{S}_i \cdot \mathbf{S}_j$ is, therefore, the dot product of the two vectors. The controlled parameters of the model, therefore, characterize systems These parameters are the average cross-link energy in units of thermal energy ($J = \chi k_B T$), The density of ABS (ρ), the cross-sectional ($x \times y$) size of the lattice (M^2), and the shared length of the fibers (N).

Ideally, the value of s_{ik} for ABS would be one, to model a system where the creation of a cross-link reduces the energy by a fixed amount. Unfortunately, this restriction gave rise to a system with highly degenerate ground states, leading to slow convergence. We, therefore, set the value of

"individual binding strength", s_{ik} to a random value chosen from a Gaussian distribution around 1.0 and a standard deviation of 0.2. Although this deviation from a simple model is not ideal, as it adds more parameters to the model, it is not inconsistent with examples of cross-linked systems which can have a range of interaction strengths [94].

A.3 Methods

Metropolis Monte Carlo [95] (MC) is used to generate an ensemble of probable states. For our model, the algorithm follows the steps:

1. A random fiber $\mathbf{S}_i$ is chosen.
2. A random direction, $\pm$ 1 z, is chosen for the proposed MC move of the previously chosen fiber, the move would, therefore, shift the values of the vector describing the fiber ($s_{ik} \rightarrow s_{i,k\pm1}$).
3. The change in energy, ΔE, between the new state and the old is calculated using equation A.1.
4. The new state is always accepted if the energy is lower ($\Delta E \leq 0$) in the new state and is accepted with the probability equal to the Boltzmann weight ($e^{-\Delta E/k_B T}$).

We define an MC step as a set of M (number of fibers) proposed MC moves.

A randomly generated system will have significantly fewer cross-links then that of an equilibrated one. Therefore thermalization of the system is required and is accomplished with the following steps. First, the system is made periodic in the direction parallel to the fibers, z, so that the lengths of the fibers, which is intended to be an idealization of real fibers, would no limit the ability of fibers to "align" themselves, optimizing the number of cross-links between them. This periodicity is removed after thermalization so that displacement can be measured. The system is run for a minimum of 100 million MC steps, and the energy of the system at each accepted step t is then fitted to the exponential

$$E(t) = (E_0 - E_\infty)e^{-t/\tau} + E_\infty, \tag{A.2}$$

where E_∞ is the average energy after thermalization, E_0 is the initial energy of the system, and τ is the step scale of the exponential. Figure A.2 is a plot of the Energy of a system undergoing

thermalization with an exponential fit to it using equation A.2. The system is then considered thermalized if one of the following conditions are met:

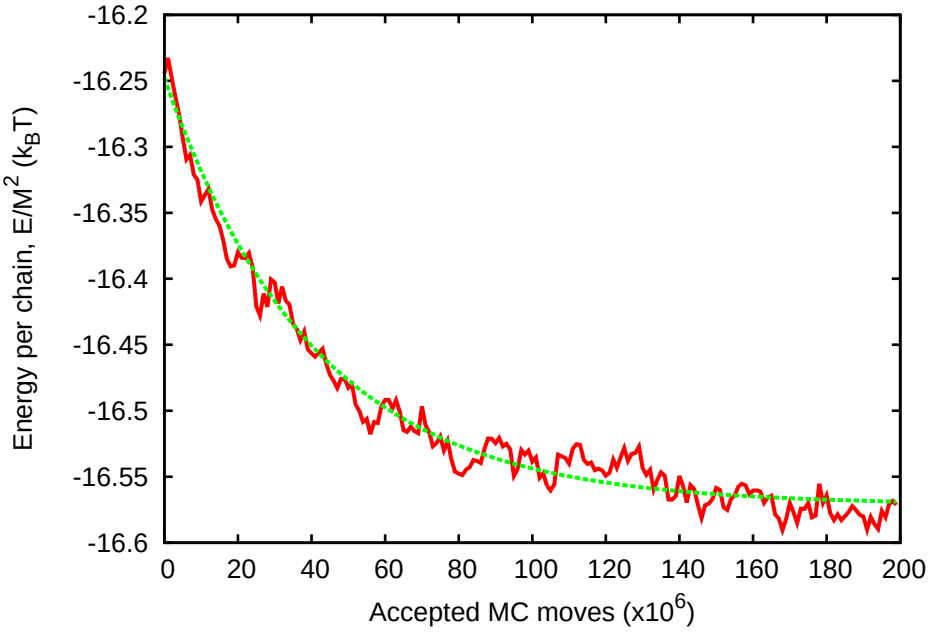

Figure A.2: Exponential fit to the Energy vs. Number of Accepted moves data in the thermalization phase of a simulated lattice

After 100 million MC steps, a system is considered thermalized if it meets one of the following criteria:

1. $|E_\infty - E_0| \leq k_B T$—i.e., the energy of the system is not changing significantly.
2. The uncertainty in τ from the fit of the exponential is on the order of 1%, and the number of accepted steps is greater than 5τ.
3. For any uncertainty in τ, in the case of noisy but consistent data, the number of accepted steps is greater than 20τ

As stated previously, the system retains periodicity parallel to fibers only during thermalization phase, and therefore chain displacements are calculated from the starting positions of the fibers at the end of thermalization. Ensembles are then generated, and thermodynamic properties of those ensembles are calculated, using the MC algorithm on multiple systems for each ρ, T, M, and N.

A.4 Results

A.4.1 Order Parameter

The order parameter of a phase change characterizes the phase properties of the system. The order parameter is dependent on reduced temperature and will be near zero in high temperatures. An order parameter will often be a measure of some symmetry breaking order in the system. Since our system lacks an obvious symmetry, the identity of an order parameter is nontrivial. Since the principal movement of the system is by fibers, we start by defining the displacement of the i–th fiber from its initial position to be d_i. The average displacement of all fibers in the system is therefore $\bar{d}$ and the number of fibers whose displacement is less than one lattice spacing from the average $|d_i - \bar{d}| < 1$ as n_f. We expect when the system has a low temperature, the probability of moving away from low energy is small, and, therefore, the fibers are mostly frozen, and will therefore have a large number of "frozen" fibers. In simulations when the temperature is high, almost any step is taken, and therefore many fibers have shifted away from the initial "surface" of the lattice. Therefore we define the order parameter f as the "frozen fraction," *i.e.*, the fraction of fibers which are within one lattice spacing of the mean $f = n_f/M^2$.

Figure A.3 plots f vs. T for systems with varying ABS densities (ρ). Each of these plots has a fitted sigmoid function of the form

$$f(T) = 1 - \frac{1}{1 + e^{-\alpha(T - T_C)}}, \tag{A.3}$$

where α is the exponential constant which describes the sharpness of the transition and T_C describe crossover temperature above which the order parameter is near zero.

We note that the chosen order parameter has the stipulated behavior which we described above. It is near zero above T_C and is much higher than zero below T_C. Additionally below T_C , we see a high degree of translational symmetry, as few fibers have displaced more than one space away from the average.

Additionally, we note that both the crossover temperature T_C and exponential constant α are dependent on ρ. Small values for ρ produced systems with lower T_C and larger exponential constants α. These larger α are indicative of a sharper "transition" from the ordered state, to

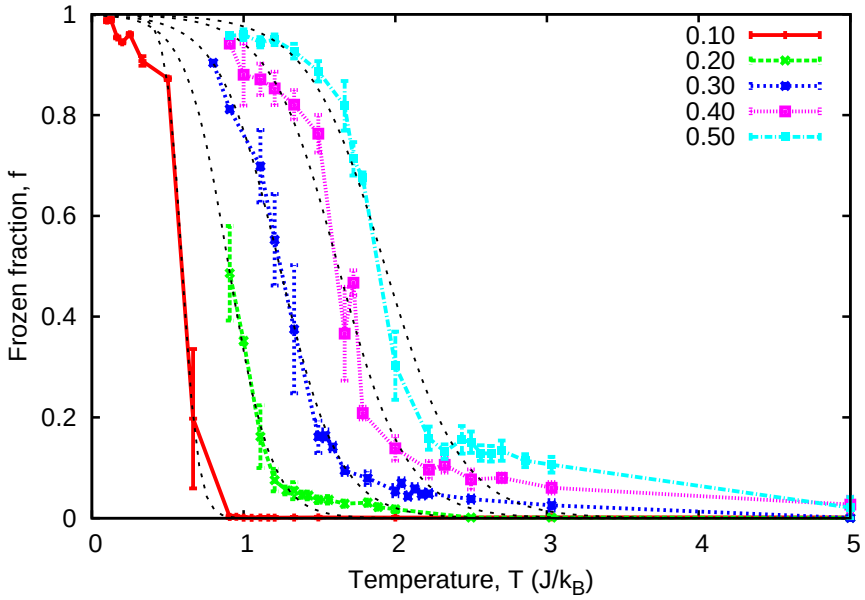

Figure A.3: Order parameter, f vs. temperature, T. Sigmoid functions, $1 - \left(1 + e^{-\alpha(T-T_C)}\right)^{-1}$, where then fit determining the crossover temperature, T_C, and exponential constant, α, which described the sharpness of the sigmoid.

the less ordered state. Large values for α represent a sudden, step function like, "transition" from ordered to disordered with little increase in temperature while small values signify a smooth and continuous "transition" between states.

Unfortunately, the order parameter we have chosen, f, is one that may only be accessible computationally and therefore we must introduce the inverse root-mean-squared displacements $1/\langle \vec{d} \rangle$ as a experimentally available analog to f. The root-mean-squared displacements $\langle \vec{d} \rangle$ in our MC simulation, is defined by the average of

$$\langle \vec{d} \rangle = \sqrt{\frac{1}{M^2} \sum_{i=0}^{M^2-1} (d_i - \bar{d})^2}. \tag{A.4}$$

In studies of surface roughening during surface growth, root-mean-squared displacements has been found to be an analogous measurement [96]. Though these measurements are interfacial properties rather than describing material properties as we wish to describe.

Plots of this analog parameter $1/\langle \vec{d} \rangle$ vs. temperature are presented in figure A.4. We note a similar sigmoidal shape where our new parameter goes to near zero above some temperature and that the temperature of that "transition" increases with ρ. The transition temperatures taken from sigmoids fitted to figure A.3 are denoted in the figure with a dotted line and the value of the location of the line above the graph. These transition temperatures match well the plots of $1/\langle \vec{d} \rangle$ vs. temperature.

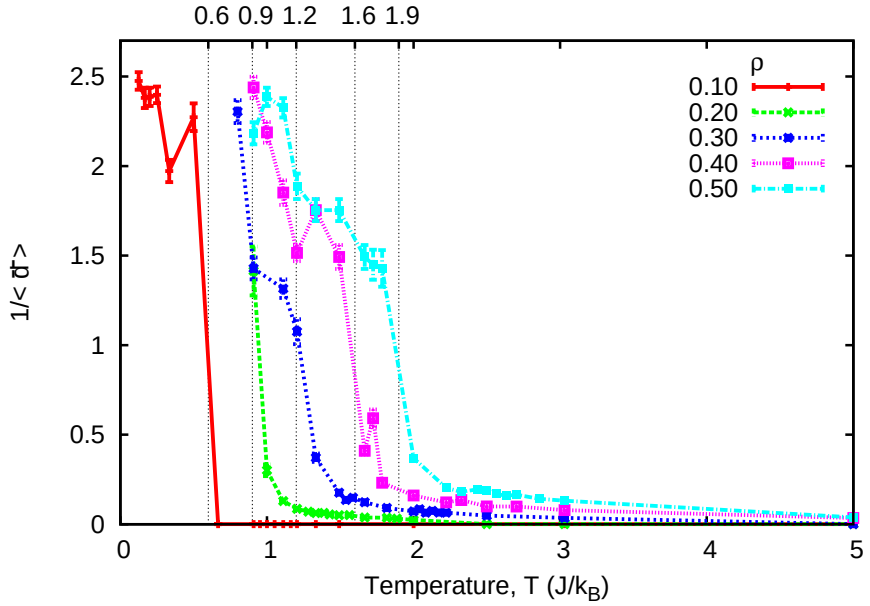

Figure A.4: $1/\langle \vec{d} \rangle$ vs. T. These plots have a similar sigmoidal shape as f vs. T plots from figure A.3. Transition temperatures predicted from sigmoids fitted to figure A.3 are denoted with dotted lines and values above the graph.

Therefore, f and $1/\langle \vec{d} \rangle$ demonstrate a "transition" from a high ordered frozen system to a disordered fluid one about a transition temperature T_C. Small amounts of noise coming from a few displaced chains which are more destructive to $1/\langle \vec{d} \rangle$ calculations where outliers have a greater effect on the resulting Gaussian fit to the normalized distribution.

A.4.2 Fractional Dimension

The sigmoidal shape of the order parameter f vs. the temperature T signify an order-disorder transition which breaks the symmetry of the surface. However, whether that symmetry is broken by many small fibers or a few large groups of fibers shifting from the mean displacement, needs to be determined. Therefore, in addition to defining displacement, d_i, we wish to define a height of the surface of a fiber h_i for which we can compute the "fractional dimension" (D_f) and characterize the smoothness of surfaces [97]. We, therefore, sample 100 configurations evenly spaced between the runs and compute $\bar{d}$ and the standard deviation of the displacement σ_d. We then discard any fiber for whom the magnitude of displacement is greater then both σ_d and the shared length of the fibers N. These fibers are no longer part of the bulk and are therefore free fibers. The average displacement of the remaining fibers $\bar{d\prime}$ is then used to determine the height of the remaining fibers at step i using

$$h_i = d_i - \bar{d\prime}. \tag{A.5}$$

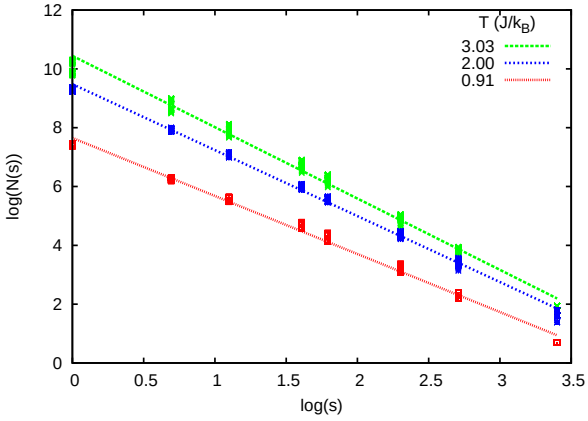

Figure A.5: $\log(N(s))$ vs $\log(s)$ for a system with $\rho = 0.30$ at three temperatures. A linear fit is plotted with the points the slope of which is the opposite the fractional dimension.

We then compute the fractional dimension, $2 \leq D_f \leq 3$ of the surface, where values near 2 represent a smooth surface while values near 3 are rough and space filling [98]. We determine D_f using the box-counting method to find the minimum number of square boxes N_{boxes} of linear size

s which are needed to cover the surface. The area of the boxes of lengths s are chosen as a factor of M. For example if the lattice is 50×50 fibers, the box sizes used are the factors of 50–*i.e.*, $1, 2, 5, 10, 25,$ and 50. Since the number of boxes needed N_{boxes} is related to the size of the boxes according to the equation $N_{boxes}(s) \propto s^{-D_f}$, the opposite of the slope of the linear fit of $log(s)$ vs. $log(N_{boxes})$ will determine D_f. Figure A.5 is such a plot of $log(s)$ vs. $log(N_{boxes})$ for simulations for $\rho = 0.3$ at three temperatures. We note the agreeable linear fit to the points whose slope is the opposite of D_f.

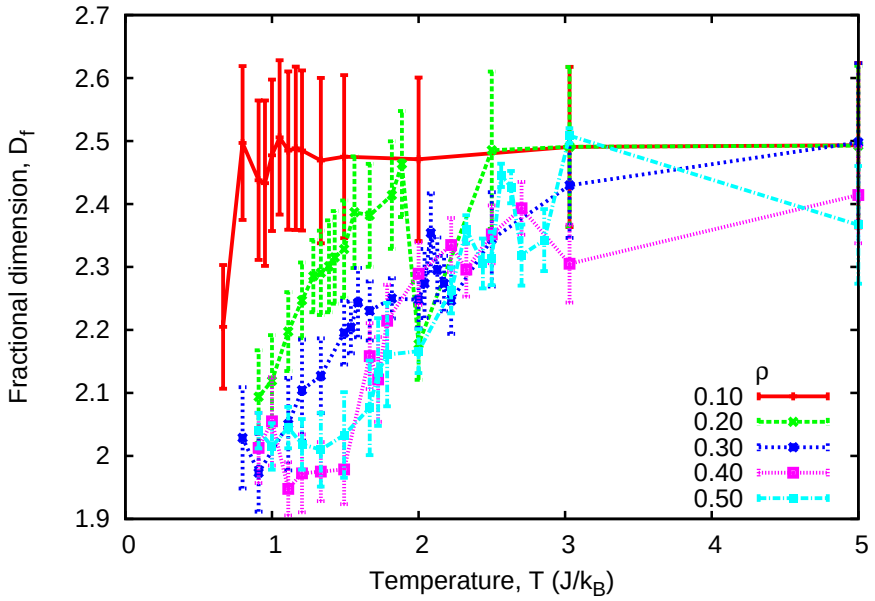

Figure A.6: Fractional dimension D_f vs. T. Smooth surfaces are apparent for low temperatures. A transition to a completely rough surface is apparent. The saturation value of 2.5 represents a surface for which the heights are completely uncorrelated. Error bars represent the uncertainty of the slope of the best-fit lines.

The fractional dimension of the lattice at each density ρ, for each temperature T, was computed and is plotted in figure A.6. The plots of D_f display smoother surfaces for systems at lower temperatures and rougher surfaces for higher temperatures. These transitions are somewhat reminiscent of the plots of f and $1/\langle \vec{d} \rangle$ in figures A.3 and A.4 respectively, in that they have different transition temperatures and different rates of transition, which depend on the density of the ABS

ρ. The maximum value of D_i is about 2.5 which is due to Brownian ("$1/f^2$") noise [98]. The model, therefore, predicts that under higher temperatures the fibers all move independently and do not form clusters of fibers.

A.4.3 Heat Capacity

In addition to the order parameters and fractional dimension size, the heat capacity, C_V, of the system was calculated for various ρ and T values. Heat capacity is determined from variance in energy δE from the equation $C_V = \left\langle (\delta E)^2 \right\rangle / (k_B T^2)$ by the fluctuation-dissipation theorem. We computed the Heat capacity per ABS, $C_V/left(M^2 \times Nright)$. For each ρ and T (see figure A.7). We note several important features of the plots. First, high and low-temperature simulations had a minimal heat capacity while the heat capacity around some peak temperature T_p was very high. Second, peaks at lower ρ where sharper than peaks at higher ρ. Third, the Location of T_p shifts up to higher temperatures as ρ increased but T_p appears to approach a maximum value below 3 J/k_b.

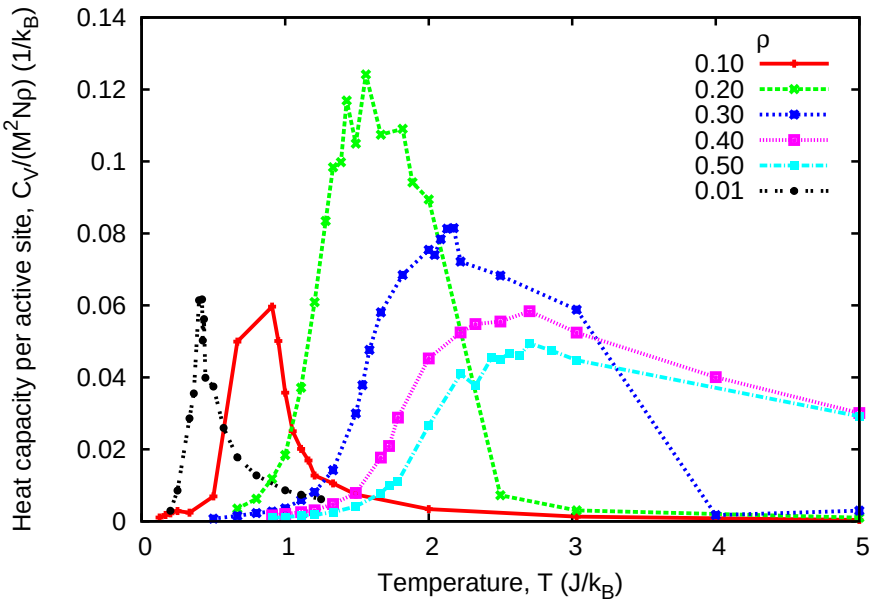

Figure A.7: The heat capacity per ABS, C_V/n, vs. Temperature T. The number of ABS is equal to $n = M \times N$. The plots show a peak in heat capacity whose temperature and sharpness depends on the ABS density ρ.

A.4.4 Frustration

We have shown the model predicts "transitions" at ρ-dependent temperatures. These "transitions" are not always sharp, but rather large values of ρ had gradual changes in order parameters with T. Larger values of ρ increase the number of ways the ABS can be arranged on the fiber. This increase in non-degenerate arrangements means more fibers are unable to match perfectly with neighboring fibers. This inability to satisfy all ABS with cross links, no matter what the binding energy and temperature of the system creates a "frustration" in the system. This frustration is lower for lower values of ρ, which also have a sharper transition. The "frustration" in the system can also be removed by making all fibers in the lattice identical. This is the only case where a ground state is well defined. To prove systems without frustration will result in sharp phase transitions, we simulated three systems with identical $\rho = 0.30$ values. The first system was generated as stated in section A.3, with random ABS locations A.8 b. The other two systems were given identical, but not random, ABS distributions. The first consisted of all ABS clustered together A.8 a, while the last system had ABS at regular intervals along the length of the fibers A.8 c. The heat capacity per ABS, as described in section A.4.3 was computed for these three systems at various temperatures, and is shown in figure A.8.

Figure A.8(d) plots the heat capacity vs. temperature of the three systems. We note that the transition for the randomly distributed system is between 1 and 4 units of temperature, while the systems with identical fibers have much sharper transitions.

The critical temperature for a clustered system A.8 a ($T_{crit} \approx 1.1\ J/k_B$) is less than the peak temperature of the random system A.8 b, as shown above ($T_p \approx 2.1\ J/k_B$). The critical temperature for the separated system A.8 c is exceptionally much higher than the other systems ($T_{crit} \approx 17.7\ J/k_B$). This figure suggests that the $\rho = 0.30$ random system is more like a clustered system than an evenly distributed system.

The large value of T_C for the evenly distributed system is a result of the extreme stability of the ground state. To move a single fiber away from the ground state costs about $4\rho NJ$ energy (4 because of the 4 neighboring fibers.) For the clustered system to move a single fiber from the ground state costs only $4J$. For a random system, the number of unsatisfied cross-links loss by moving from the minimum energy state is $8n_b$, where n_b is the number of "boundaries" between

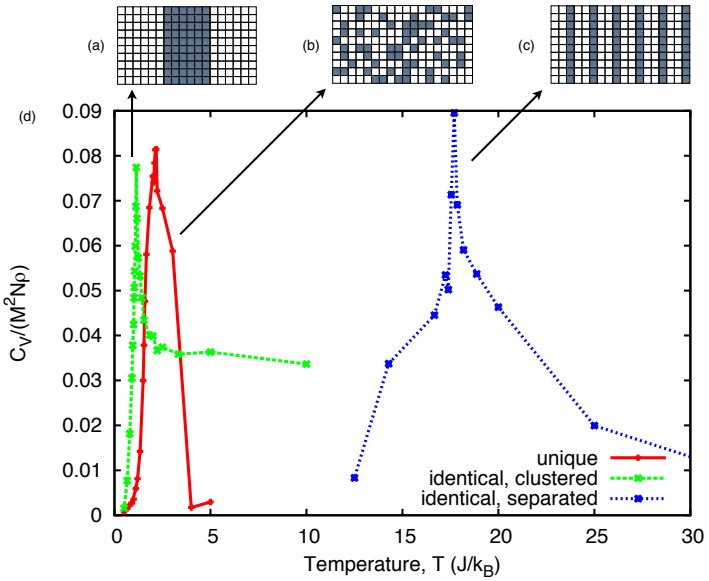

Figure A.8: The heat capacity of three systems with identical ABS density (ρ) but different distributions. The distributions include: (a) A system with identical fibers with clustered ABS locations, (b) A system with non-identical, random distributions of ABS, (c) A system with identical fibers with evenly distributed ABS locations. (d) Heat capacity vs. temperature plots for the three previously mentioned systems.

ABS clusters and clusters of empty binding sites.

The number of these boundaries (n_b) decreases with clustering of ABS. Since lower densities are randomly distributed along a much larger space of available sites, the distributions allow for fewer n_b. However, since there is less possible variance in n_b, we expect a more uniform fiber to yield a sharper transition, which we see in figures A.3 A.3 and A.7. Increase in ρ not only allows for an increase in n_b, leading to a transition at higher temperatures to overcome energy differences, but also larger variances in n_b, and therefore wider transition ranges.

To demonstrate the relation between increasing ρ and the variation of domain boundaries, n_b, we plot the standard deviation of the possible number of domain boundaries σ_n vs. ρ for $N = 100$ in figure A.9. We note σ_n increases monotonically up to $\rho = 0.50$. Thus systems with high ρ exhibit a greater degree of frustration and therefore have wider transition temperatures.

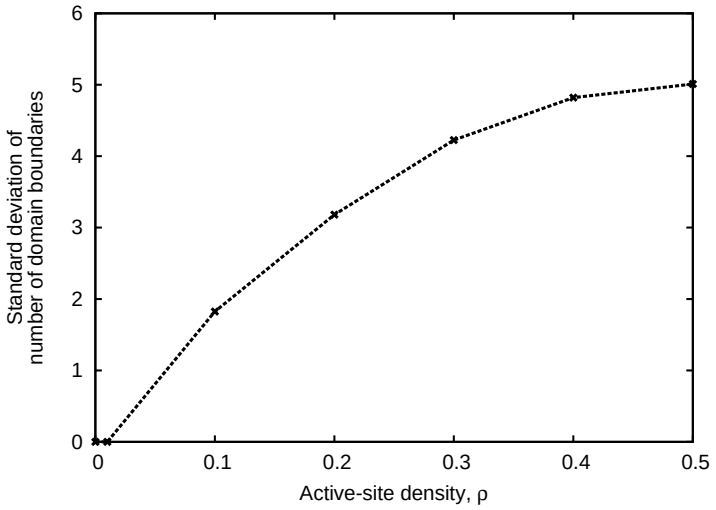

Figure A.9: The standard deviation of the number of domain boundaries per chain vs. ABS density The number of domains in low ρ systems is expected to be similar to the number of ABSs, with little variance. These systems are similar to the separated systems. The number of domains increases with ρ; however, the probability of ABS clustering also increases, therefore the variance in the number of domains increases.

A.5 Discussion

The density of Available Binding Sites (ABS), as well as the interaction strength, are important factors in the physical properties in randomly distributed available site cross-linked system. The smoothness of the surface and diffusion rate of the fibers depended on the temperature vs. cross-link interaction strength and also was affected by the density of ABS. Systems with low temperature vs. interaction strength remain mostly frozen while systems with high temperature vs. interaction strength were more diffuse and did not retain a solid surface. Lower ABS densities resulted in transition between these states to be more sudden and happen at lower temperature vs. interaction strength ratios. Higher ABS densities resulted in a more gradual transition at higher temperature vs. interaction strength ratios. The gradual transition was found to be the result of greater frustration (or an inability to satisfy all ABS with cross links). Systems with less random distributions of ABS had sharper transitions.

Cross-link materials are shown even in this simple model, to have great flexibility in physi-

cal properties. Transition temperature can be controlled with interaction energy or ABS density or through the control of the number of ABS domains. The sharpness of the transition can be controlled by ABS density or the variation of distribution between fibers of ABS domains. One example of the leveraging of these traits in nature is Echinoderms, which are known to stiffen their exterior dermis when threatened [99]. This response is obtained chemically by a Ca^{2+}-mediated increase in cross-link interaction strength of proteoglycan cross-links.

We have proposed a three-dimensional lattice model that exhibits a variety of behaviors from a small set of tunable parameters. This rich phase behavior is possibly the reason cross-linked matrix are abundant in nature. Also, it is a signal to the usefulness in industry.

Appendix B

Publications

E. Jakobsson, O. Argüello-Miranda, S.-W. Chiu, Z. Fazal, J. Kruczek, S. Nunez-Corrales, S. Pandit, and L. Pritchet. "Towards a unified understanding of lithium action in basic biology and its significance for applied biology". *The Journal of membrane biology* 250 (2017), 587–604.

J. Kruczek, S.-W. Chiu, E. Jakobsson, and S. A. Pandit. "Effects of Lithium and Other Monovalent Ions on Palmitoyl Oleoyl Phosphatidylcholine Bilayer". *Langmuir* 33 (2017). PMID: 28076953, 1105–1115.

J. Kruczek, M. Saunders, M. Khosla, Y. Tu, and S. A. Pandit. "Molecular dynamics simulations of ether-and ester-linked phospholipids". *Biochimica et Biophysica Acta (BBA)-Biomembranes* 1859 (2017), 2297–2307.

C. B. Bennett, J. Kruczek, D. Rabson, W. G. Matthews, and S. A. Pandit. "The effect of cross-link distributions in axially-ordered, cross-linked networks". *Journal of Physics: Condensed Matter* 25 (2013), 285101.

J. Kruczek, S.-W. Chiu, S. Varma, E. Jakobsson, and S. A. Pandit. "Interactions of Mono- and Divalent cations at Palmitoyl Oleoyl Phosphatidylcholine Interface". In preparation. 2019.

Appendix C

Copyright Permissions

Title:	Molecular dynamics simulations of ether- and ester-linked phospholipids
Author:	James Kruczek,Matthew Saunders,Meghna Khosla,Yicheng Tu,Sagar A. Pandit
Publication:	Biochimica et Biophysica Acta (BBA) - Biomembranes
Publisher:	Elsevier
Date:	December 2017

Title: Effects of Lithium and Other Monovalent Ions on Palmitoyl Oleoyl Phosphatidylcholine Bilayer

Author: James Kruczek, See-Wing Chiu, Eric Jakobsson, et al

Publication: Langmuir

Publisher: American Chemical Society

Date: Jan 1, 2017

PERMISSION/LICENSE IS GRANTED FOR YOUR ORDER AT NO CHARGE

This type of permission/license, instead of the standard Terms & Conditions, is sent to you because no fee is being charged for your order. Please note the following:

- Permission is granted for your request in both print and electronic formats, and translations.
- If figures and/or tables were requested, they may be adapted or used in part.
- Please print this page for your records and send a copy of it to your publisher/graduate school.
- Appropriate credit for the requested material should be given as follows: "Reprinted (adapted) with permission from (COMPLETE REFERENCE CITATION). Copyright (YEAR) American Chemical Society." Insert appropriate information in place of the capitalized words.
- One-time permission is granted only for the use specified in your request. No additional uses are granted (such as derivative works or other editions). For any other uses, please submit a new request.

BACK CLOSE WINDOW

Copyright Clearance Center

Note: Copyright.com supplies permissions but not the copyrighted content itself.

1 PAYMENT 2 REVIEW 3 CONFIRMATION

Step 3: Order Confirmation

Thank you for your order! A confirmation for your order will be sent to your account email address. If you have questions about your order, you can call us 24 hrs/day, M-F at +1.855.239.3415 Toll Free, or write to us at info@copyright.com. This is not an invoice.

Confirmation Number: 11794300
Order Date: 02/27/2019

If you paid by credit card, your order will be finalized and your card will be charged within 24 hours. If you choose to be invoiced, you can change or cancel your order until the invoice is generated.

Payment Information

James Kruczek
jkruczek@mail.usf.edu
+1 (813) 974-2871
Payment Method: n/a

Order Details

Journal of Physics : Condensed Matter

Order detail ID:	71827117
Order License Id:	4537050761314
ISSN:	0953-8984
Publication Type:	Journal
Volume:	
Issue:	
Start page:	
Publisher:	IOP Publishing
Author/Editor:	American Institute of Physics ; Institute of Physics (Great Britain)

Permission Status: Granted
Permission type: Republish or display content
Type of use: Thesis/Dissertation

Requestor type	Author of requested content
Format	Print, Electronic
Portion	chart/graph/table/figure
Number of charts/graphs/tables/figures	9
The requesting person/organization	James Kruczek
Title or numeric reference of the portion(s)	figures 1-9
Title of the article or chapter the portion is from	The effect of cross-link distributions in axially-ordered, cross-linked networks